Imperial College London
Department of Physics

Ionisation Cooling Lattices for the Neutrino Factory

Androula Alekou

March 19, 2012

Submitted in part fulfilment of the requirements for the degree of
Doctor of Philosophy in Physics of Imperial College London
and the Diploma of Imperial College London

Declaration

I herewith certify that all material in this dissertation which is not my own work has been properly acknowledged.

Androula Alekou

Abstract

The future accelerator complex of the Neutrino Factory will have an excellent precision and outstanding discovery reach, and is therefore a facility of choice for precise neutrino oscillation measurements. In the Neutrino Factory, muons are accumulated into storage rings and decay to neutrinos. However, due to the fact that the muon beam is produced occupying a large transverse phase-space, it is essential that its emittance is decreased using ionisation cooling.

The reference ionisation cooling lattice of the Neutrino Factory has a large magnetic field at the position of the RF cavities, and there is a strong concern this can lead to RF breakdown. Therefore, there lies a great necessity for alternative cooling lattices to be found.

This thesis presents several cooling lattices that were designed aiming to mitigate the problem of the RF breakdown in the presence of a magnetic field, that the reference lattice suffers from. In particular, amongst these lattices, a promising new configuration which makes use of a pair of opposite polarity and homocentric coils, named "Bucked Coils", is presented. The Bucked Coils lattice not only manages to successfully achieve a virtually zero longitudinal magnetic field at the position of the RF cavities, but also obtains a better transmission than the reference lattice. A detailed comparison between the reference and the new lattices is presented with respect to the magnetic field, transmission and cooling efficiency. A possible extension of the work is also discussed.

A six-dimensional cooling could be used at a Neutrino Factory but is essential for a Muon Collider. Another novel configuration, which aims to achieve 6D ionisation cooling, is presented in this thesis. This new lattice creates dispersion with the use of dipoles, and a correlation between energy loss and position with the use of wedge absorbers. A detailed description of this lattice configuration and analysis is given, together with preliminary results.

To my parents.

Acknowledgements

There are many people I feel indebted to.

First of all, I would like to thank my supervisor, Jaroslaw Pasternak, for accepting me as his student. His motivation, enthusiasm and creativity helped me and taught me a lot. I thank him for encouraging me and challenging me through my PhD, for the frequent meetings we had, and for correcting my papers, and especially this thesis, in detail. For never accepting anything but my best effort. Thank you.

I would also like to express my sincere gratitude to my co-supervisor, Ken Long, for giving me the great opportunity to be a PhD student at Imperial College.

To my three examiners: Dr. Morgan Wascko, Dr. Bruno Muratori, and Prof. Zulfikar Najmudin for their detailed corrections. Their constructive comments have undoubtedly improved the quality of this work.

To Chris Rogers, for patiently guiding my first steps in G4MICE and for his availability throughout these years.

To Juergen Pozimski, for the valuable discussions we had, and for all the support he gave me.

To my former supervisor, Fotios Ptochos, for helping me pursue my studies at Imperial College. I do not think I would be here without his valuable guidance.

To Raymond Beuselinck and Simon Fayer for always being so helpful whenever there was a code related question.

To my office-mates and friends Simon, Ajit, Adam, Edward, and Morteza for their valuable advices. I feel I am especially indebted to Adam for his enormous kindness, for always listening, understanding, and for generously offering his valuable proof-reading skills. To Edward for always being there for me, and for the amazing time we were having whenever on a break or relaxing.

My friends made this journey a lot easier. I offer my sincerest gratitude to: Marilia Giannakopoulou: for the excellent time we were having whenever going out for a glass of Sauvignon Blanc, or just for coffee on level 8. For reminding me that all PhD students face very similar issues. Christos Gavriel: for the very valuable advices, and in particular the one that says “when you face a problem sleep on it before taking any action”. John Demetriou (Tarzan): for the amazing time we were having whenever meeting up for Tavli, Taboo or just catching up. David Forrest: for making every collaboration meeting much more fun and for the great help he so generously offered me through the post-doc application process; I do not think I can thank him enough. Laura, Loukia (Bubu): my two best friends, for listening, understanding, being there for me whenever I needed them the most. Thank you.

I would like to express my heartfelt gratitude to my parents, Maria and Christos, for believing in me, supporting me, and giving me their advices. I feel I owe them everything.

Finally I want to thank Patrick for his support, for helping me stand up on my two feet whenever feeling down, for always giving me his honest opinion, and for supporting my decisions.

I would like to thank Ken, Chris, Patrick and Adam for proof-reading parts of this thesis. Also special thanks to Jaroslaw and Ken for giving me the amazing opportunity to travel the world in order to attend so many meetings and conferences.

Contents

List of Figures

List of Tables

Chapter 1

Introduction

1.1. The Neutrino

The neutrino, denoted by the Greek letter ν (nu), is the lightest known elementary fermion. In the Standard Model of elementary physics its mass is assumed to be zero, however it is now known that this particle has mass. Due to the fact that neutrinos interact only weakly[1] with matter, it can pass through the Earth and hardly be affected, and we do not feel ten trillions of them passing through our bodies every second. Neutrinos are the most numerous matter particles in the universe; for every single atom there are about a billion neutrinos. This particle belongs to the the lepton family and has three flavours: electron (ν_e), muon (ν_μ), and tau (ν_τ). Neutrinos come from a variety of sources like radioactivity, the Sun, interstellar space and from the Big Bang itself. They are of great importance: they may have played a significant role in shaping the galaxies, stars and planets; in addition stars would not burn without them. Neutrinos may be the reason why the universe exists at all, as they are thought to be a vital piece in the longstanding puzzle of matter-antimatter asymmetry of our Universe [1].

In β-decay, a radioactive nucleus A is transformed into a lighter nucleus B, with the emission of an electron[2]:

$$A \rightarrow B + e^-. \tag{1.1.1}$$

Because of charge conservation, nucleus B must have one more unit of positive charge than A. Also, in a two-body decay ($A \rightarrow B + C$) the outgoing energies are kinematically determined in the centre-of-mass frame. If A is at rest, then B and e^- come out back-to-back and therefore, from energy conservation, the

---

[1] Although neutrinos interact only via the weak force with matter, here the word “weak” has the meaning of small interaction cross-section of a neutrino with matter.

[2] There are also β^+ decays, which emit a positron, e^+.

electron energy is:

$$E = \left(\frac{m_A^2 - m_B^2 + m_e^2}{2m_A} \right) c^2, \tag{1.1.2}$$

i.e. fixed once the three masses are specified. However, from experimental measurement of β-decay, it is known that the electron energy has a continuous spectrum (see fig. 1.1) [2].

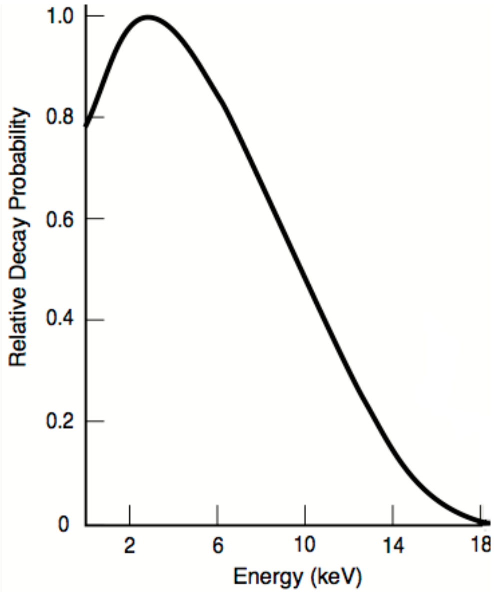

Figure 1.1.: Continuous energy spectrum of electron emerging from a β-decay. This continuity suggests that another particle, apart from electron, is produced.

The existence of the neutrino was first proposed from W. Pauli in December 1930 in order to explain the continuous spectrum of β-decay[3] [3]. He concluded that another particle is emitted together with the electron. This particle needed to be neutral in order to conserve electric charge (and to also explain why it left no track). Pauli called it the "neutron" and assumed that it has mass. Although this idea was greeted with scepticism, in 1933-34 E. Fermi presented a theory of beta decay that incorporated Pauli's particle. This theory turned out to be so successful that Pauli's suggestion had to be taken seriously. The new particle had to be extremely light since the observed electron energy spectrum extends up to the maximum value of eq. 1.1.2. Fermi therefore proposed to call it neutrino, which in Italian means neutral and small. Fig. 1.2 illustrates β-decay in the form of Feynman diagrams.

---

[3] Also to solve the spin problem of ${}^7N_{14}$ and other nuclei, see [3].

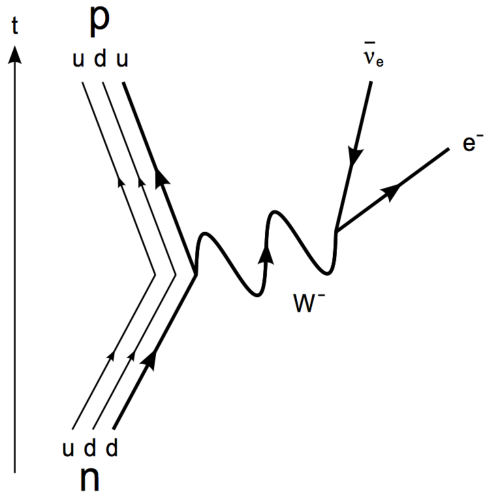

Figure 1.2.: In β-decay, a neutron in a nucleus transforms into a proton, emitting an electron and an electron-antineutrino: $n \to p + e^- + \bar{\nu}_e$ (in β^+ decays a neutron transforms into an antiproton, emitting a positron and an electron-neutrino: $n \to p^- + e^+ + \nu_e$).

A method of measuring the neutrino mass was proposed by Fermi and F. Perrin [4]. This method was based on the high-accuracy measurement of the end-point part of the electron spectrum in which neutrino energy is comparable with neutrino mass. The idea was realised in experiments performed by G. Hanna and B. Pontecorvo [5] and S. Curran [6] et al. in 1949. The upper bound of the neutrino mass was found to be much smaller than the electron mass: $m_\nu \leq 500$ eV $\cong 10^{-3} m_e$.

1.2. C, P and CP Violation in Weak Interactions

Prior to 1956, it was taken for granted that the mirror image, or "parity operator"[4], of any physical process also represents a perfectly possible physical process. A disturbing paradox arose in the early fifties, known as the "tau-theta" puzzle, in which two strange mesons, called at the time τ and θ, appeared to be identical in all aspects (mass, zero spin, charge etc). However, one of them decayed into two pions and the other into three pions, which are states of opposite parity.

After the discovery of the neutrino in 1956 (described in sec. 1.3), Lee and Yang [7] suggested that τ and θ are the same particle, now known as the K^+, and that parity is simply not conserved in one of the two decays. This idea prompted their search for evidence of parity invariance in the weak interactions. Searching the literature they only found evidence for parity invariance under

---

[4] The phrase "mirror image" is misleading, as it only implies a left-to-right transformation. The parity operator corresponds to a simultaneous left-to-right and upside-down transformation: $P(f(\vec{x})) = f(-\vec{x})$.

electromagnetic and strong, but not under weak interactions. Wu [8] recorded the direction of the emitted electrons using Cobalt 60, which undergoes beta decay (${}^{60}Co \to {}^{60}Ni + e + \bar{\nu}_e$), and found that most of the electrons came out in an opposite direction to the nuclear spin. This physical process is not invariant under the parity transformation; if it were, the electrons would have to come out in equal numbers, opposite and in line with the nuclear spin. The cleanest evidence of parity violation is the fact that in pion decay ($\pi^+ \to \mu^+ + \nu_\mu$) the emitted μ^+ always comes out left-handed. A more detailed description of parity invariance can be found in [2].

In elementary particle physics, the charge conjugation operator, C, converts each particle into its antiparticle: $C|p\rangle = |\bar{p}\rangle$. This operator also changes the sign of all "internal" quantum numbers (charge, baryon number, lepton number, strangeness, charm, beauty, truth), but leaves mass, energy, momentum and spin untouched [2]. As with parity, charge conjugation is conserved in electromagnetic and strong, but not under weak interactions. For instance, when applied to the above pion decay, C gives a left-handed muon, whereas in fact the muon always comes out right-handed.

Although the weak interactions are not invariant under P and C, a combination of the parity and charge operators, CP, turns the left-handed antimuon into a right-handed muon which is exactly what we observe in nature. CP was therefore thought to be invariant, until J. Cronin and V. Fitch provided clear evidence in 1964 that it can be violated (Nobel Prize in 1980) [2].

It should be noted that in 1957, the discovery that the parity P and charge conjugation C are violated in weak processes, led to a drastic change of the idea of neutrino. The theory of *the two-component neutrino* was proposed by Landau [9], Lee and Yang [10] and Salam [11], in order to explain the parity violation in the β-decay and other weak decays. This theory played an extremely important role in the development of the theory of weak interaction, but on the other hand misled physicists to believe for many years that neutrinos were massless.

1.3. Neutrino Discovery

1.3.1. First Savannah River Experiment

A new detection technology, a liquid scintillation counter, was exploited by C. Cowan and F. Reines in order to detect the products of the inverse beta-decay reaction [12]:

$$\bar{\nu} + p^+ \to n + e^+. \tag{1.3.1}$$

A preliminary result was published in 1953 [13] using neutrinos from a reactor at the Hanford Site. However, the background turned out to be larger

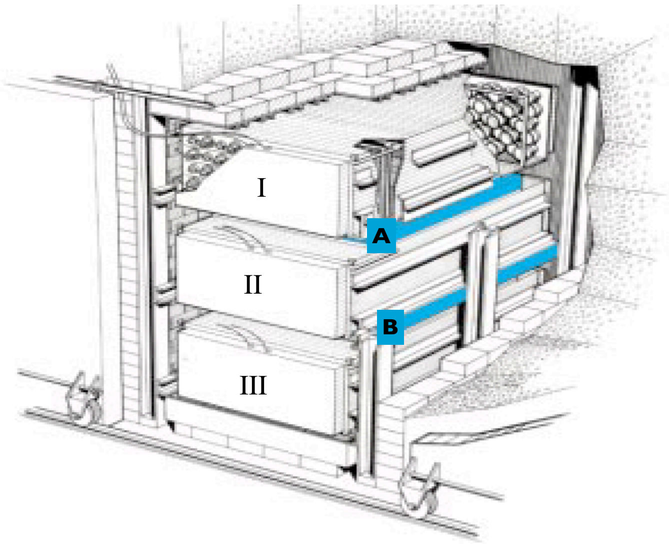

Figure 1.3.: Layout of the first Savannah river experiment. The two target tanks (A and B) were sandwiched between the three scintillation detectors (I, II, and III). A and B were filled with water, in which cadmium was dissolved. Figure taken and edited from [14].

than expected, mostly due to cosmic rays that mimicked neutrino events, and therefore the results were said to be inconclusive.

In 1956 Cowan and Reines moved to the Savannah River Plant in South Carolina where their inverse beta-decay experiment was redesigned. Their detector was entirely reconfigured to differentiate better between events induced by cosmic rays and those initiated in the detector by reactor neutrinos. By mid-April the detection system had been tested and a reactor-power-dependent signal had been observed. The experimental layout is shown in fig. 1.3: two large tanks (called the "target tanks", labeled A and B) were filled with water. The protons in the water were the target for inverse beta decay. The cadmium chloride, which was dissolved in the water, provided the nuclei that would capture the neutrons. The target tanks were sandwiched between three liquid scintillation detectors (I, II and III) of 4,200 litres total capacity and 110 photomultiplier tubes each. A neutrino-induced event in, e.g., tank A would create two pairs of proton-induced prompt coincidence pulses from detectors I and II (the first pair from positron annihilation and the second from neutron capture). The two pairs would be separated by 3-10 μs, and thus the spatial origin of the event could be deduced with certainty, since the signals would be distinguished from false delayed-coincidence signals induced by stray particles from cosmic-ray showers [14, 12]. Reines and Cowan sent a telegram to Pauli in Zurich on June 14, 1956:

"We are happy to inform you that we have definitely detected neutrinos from fission fragments by observing inverse beta decay of protons. Observed cross section agrees well with expected six times ten to minus forty-four square centimeters."

On their monthly report of June 20 of the same year they stated that:

"...the experiment to detect the free neutrino has been completed with a positive result and has been reported on at the American Physical Society meeting at Yale."

The tests undertaken to prove that the detected events were indeed characteristic of inverse beta decay are described in *Science* [15] and *Nature* [16]. Together with the telegram to Pauli, these articles announced a close match between experimental and theoretical cross sections as evidence of the existence of the neutrino. Although in Reines and Cowan's 1953 experiment at Hanford a comparison of the theoretical and measured cross sections played an important role, such a comparison did not take place in their first 1956 experiment at Savannah River. As indicated in an examination of their 1956 laboratory notebooks, the focus of their attention was the demonstration of the unique event signature [12].

1.3.2. Second Savannah River Experiment

Another measurement of the inverse beta-decay cross section was undertaken by Reines and Cowan and their co-workers in late September 1956, where a different arrangement of the Savannah River detector was used (see [14, 12] for details on the experimental layout). The results of this experiment were reported in 1959. The measured prediction for the inverse beta-decay process was $11 \pm 2.6 \times 10^{-44}$ cm^2, consistent with the 1959 theoretical cross section. Their results provided unambiguous confirmation of the neutrino's existence [14, 12].

1.4. Neutrino Oscillations

Neutrino oscillations, predicted by Pontecorvo[5] [18] and Maki, Nakagawa and Sakata [19], describe a process where neutrinos change flavour as they propagate between a source and a detector. This phenomenon is of great experi-

---

[5] B. Pontecorvo was the first physicist who mentioned a possibility of neutrino oscillations. He also predicted [17] that the number of events $\bar{\nu} + p \to e^+ + n$ with reactor antineutrino would be smaller than the expected number, something that was confirmed in the KamLAND reactor experiment. In 1967 B. Pontecorvo also envisaged the solar neutrino puzzle [3].

mental and theoretical interest since its observation implies non-zero neutrino mass, something that cannot be explained by the Standard Model.

The Super-Kamiokande experiment [20] obtained the first model independent evidence for neutrino oscillations in 1998, when a significant up-down asymmetry of the atmospheric high-energy ν_μ events was discovered. Atmospheric neutrinos with energy greater than a few GeV, can be traced back to primary cosmic rays. These high energy cosmic rays arrive at the Earth almost isotropically which results in the prediction that the flux of atmospheric neutrinos should be equal for equal solid angles. However, the up/down asymmetry ($A = \frac{Up-Down}{Up+Down}$) for high energy ν_μ events was found to be $A = 0.296 \pm 0.048$ (stat.) $\pm\, 0.01$ (syst.).

The first experimental solar neutrino measurements were reported in 1968, by Ray Davis *et al.* The experiment used a tank of chlorine in the Homestake mine in South Dakota. Chlorine can absorb a neutrino and convert into argon [2]:

$$\nu_e + {}^{37}Cl \to {}^{37}Ar + e^-. \tag{1.4.1}$$

Several argon atoms were collected within several months. However, the total accumulation was about a third of what John N. Bahcall predicted[6], giving rise to the "solar neutrino problem". The Sudbury Neutrino Observatory (SNO) [21] proved in 2001 that the long-standing solar neutrino puzzle was a result of neutrino oscillations. Although, in the case where no oscillation occurs, all neutrinos coming from the sun should be ν_e, SNO had shown that the ratio of the flux of the solar ν_e to the total flux of ν_e, ν_μ and ν_τ is $\sim 1/3$.

The first confirmed observation of neutrino oscillations from terrestrial neutrino sources was obtained by KamLAND [22] from the measurement of the energy spectrum of neutrinos produced in nuclear reactors. A significant distortion of the reactor antineutrino spectrum was found in this experiment.

There are three known types (flavours) of neutrinos: electron, muon and tau. Although neutrinos are created or detected with a well defined flavour, flavour transitions are possible while propagating in vacuum or matter. The transitions occur because the neutrino mass eigenstates i (i=1, 2, 3) are superpositions of the flavour eigenstates α (α=e, μ, τ). Therefore, a neutrino that was produced as a neutrino of flavour α at a given location has a calculable probability to be detected as a neutrino of flavour β after travelling to another location.

The relation between flavour and mass eigenstates is [23]:

$$\mid \nu_\alpha\rangle = \sum_i U_{\alpha i} \mid \nu_i\rangle, \tag{1.4.2}$$

where $U_{\alpha i}$ is the Pontecorvo-Maki-Nakagawa-Sakata (PMNS) mixing matrix.

---

[6] Bahcall was responsible for most of the calculations of solar neutrino abundances.

Eq. 1.4.3 presents the mixing matrix expressed in terms of the rotation, or mixing angles θ_{12}, θ_{23}, θ_{13} and the CP-violation phases δ, α_1 and α_2:

$$U_{\alpha i} = \begin{pmatrix} 1 & 0 & 0 \\ 0 & c_{23} & s_{23} \\ 0 & -s_{23} & c_{23} \end{pmatrix} \times \begin{pmatrix} c_{13} & 0 & s_{13}e^{-i\delta} \\ 0 & 1 & 0 \\ -s_{13}e^{i\delta} & 0 & c_{13} \end{pmatrix} \times \begin{pmatrix} c_{12} & s_{12} & 0 \\ -s_{12} & c_{12} & 0 \\ 0 & 0 & 1 \end{pmatrix} \times \begin{pmatrix} e^{i\alpha_1/2} & 0 & 0 \\ 0 & e^{i\alpha_2/2} & 0 \\ 0 & 0 & 1 \end{pmatrix}, \qquad (1.4.3)$$

where α_1 and α_2 are the two Majorana phases[7], and δ the Dirac phase. The PMNS matrix can also be written as:

$$U_{\alpha i} = \begin{pmatrix} c_{12}c_{13} & s_{12}c_{13} & s_{13}e^{-i\delta} \\ -s_{12}c_{23} - c_{12}s_{23}s_{13}e^{i\delta} & c_{12}c_{13} - s_{12}s_{23}s_{13}e^{i\delta} & s_{23}c_{13} \\ s_{12}s_{23} - c_{12}c_{23}s_{13}e^{i\delta} & -c_{12}s_{23} - s_{12}c_{23}s_{13}e^{i\delta} & c_{23}c_{13} \end{pmatrix} \times \begin{pmatrix} e^{i\alpha_1/2} & 0 & 0 \\ 0 & e^{i\alpha_2/2} & 0 \\ 0 & 0 & 1 \end{pmatrix}, \qquad (1.4.4)$$

where s_{ij}=sin θ_{ij} and $c_{ij} = \cos\theta_{ij}$.

The first term in the factorized representation of the mixing matrix (eq. 1.4.3), is called the "atmospheric term" and is determined by atmospheric and long-baseline accelerator neutrino experiments. The third term, which is the "solar term", is determined by solar and long-baseline reactor experiments. The second term is the "mixed term" and is determined by long-baseline accelerator and short-baseline reactor experiments [24].

In eq. 1.4.2, $\mid \nu_i\rangle$ is the state vector of neutrino with energy E, mass eigenstate ν_i, mass m_i and momentum p_i given by:

$$p_i = \sqrt{E^2 - m_i^2} \simeq E - \frac{m_i^2}{2E},\ (m_i^2 \ll E^2). \qquad (1.4.5)$$

If the initial time is $t = 0$, then the state of neutrino ν_α at time $t \neq 0$ will be (for $\hbar = 1$ and $c = 1$) [23]:

$$\mid \nu_a\rangle_t = \sum_i U_{\alpha i} e^{-iEt} \mid \nu_i\rangle, \qquad (1.4.6)$$

and the time-dependent transition amplitude for a flavour conversion $\nu_\alpha \to \nu_\beta$

---

[7] If neutrinos are identical to their antiparticles they are called "Majorana", otherwise, they are called "Dirac" (see [3] for more details). The Majorana phases only have physical consequences if neutrinos are Majorana particles, otherwise $\alpha_1 = \alpha_2 = 0$.

is then [23]:

$$A(\nu_\alpha \to \nu_\beta)(t) = \langle \nu_\beta | \nu_\alpha(x,t) \rangle = \sum_i U^*_{\beta i} U_{\alpha i} e^{ip_i x} e^{-iEt}. \tag{1.4.7}$$

Using equation 1.4.5, equation 1.4.7 can be written as:

$$A(\nu_\alpha \to \nu_\beta)(t) = \langle \nu_\beta | \nu_\alpha(x,t) \rangle = \sum_i U^*_{\beta i} U_{\alpha i} e^{-im_i^2 \frac{L}{2E}} = A(\nu_\alpha \to \nu_\beta)(L), \tag{1.4.8}$$

with $L = x = ct$ being the distance between source and detector. The probability for a neutrino created with a flavour α to be detected with flavour β is [25]:

$$\begin{aligned} P(\nu_\alpha \to \nu_\beta) &= \left|A(\nu_\alpha \to \nu_\beta)\right|^2 = \left|\sum_i U^*_{\beta i} U_{\alpha i} e^{-im_i^2 \frac{L}{2E}}\right|^2 \\ &= \delta_{\alpha\beta} - 4\sum_{i>j} \Re(U^*_{\beta i} U_{\alpha i} U_{\beta j} U^*_{\alpha j}) \sin^2\left(\frac{\Delta m^2_{ij} L}{4E}\right) \\ &+ 2\sum_{i>j} \Im(U^*_{\beta i} U_{\alpha i} U_{\beta j} U^*_{\alpha j}) \sin\left(\frac{\Delta m^2_{ij} L}{2E}\right), \end{aligned} \tag{1.4.9}$$

where $\Delta m^2_{ij} = m_i^2 - m_j^2$ is the mass (squared) difference, L the lab-frame distance between the neutrino source and the detector, and E the lab-frame neutrino energy. Including the previously omitted factors of c and $\hbar$:

$$\frac{\Delta m^2_{ij}(\text{eV}^2) L(\text{km})}{4E(\text{GeV})} \approx 1.27 \Delta m^2_{ij} L/E. \tag{1.4.10}$$

From 1.4.9 it can be seen that, if at least one mass state is non-zero (and provided that all mass states are different from one another), then oscillations occur. It should be highlighted that L and E are defined by the experiment, and are common to all ν_i components of the beam[8].

The oscillation probability $P(\nu_\alpha \to \nu_\beta)$ of equation 1.4.9 is that of a neutrino rather than antineutrino. Using the fact that $\bar{\nu}_{R,\alpha} \to \bar{\nu}_{R,\beta}$ is the CPT[9]-mirror image of $\nu_{L,\beta} \to \nu_{L,\alpha}$, where the indices L and R correspond to left and right felicities, then the probability $P(\bar{\nu}_\alpha \to \bar{\nu}_\beta)$ for the corresponding antineutrino oscillation can be found from $P(\nu_\beta \to \nu_\alpha)$. Assuming that CPT invariance

---

[8] In [26] it is shown that the different mass eigenstate components of a beam that contribute coherently to the oscillation signal must have the same energy E. However, in the literature it is frequently assumed that these different mass eigenstates have a common momentum rather than energy. This assumption is technically incorrect; nevertheless, it is a harmless error, since it leads to the same oscillation probabilities described in this section.

[9] T is the time reversal operator, which turns t into $-t$; if $\alpha + \beta \to \delta + \gamma$, then a T transformation would result into $\delta + \gamma \to \alpha + \beta$. CPT symmetry involves the simultaneous inversion of charge, parity and time.

holds (which is believed to be the case for neutrino oscillations in vacuum):

$$P(\bar{\nu}_\alpha \to \bar{\nu}_\beta) = P(\nu_\beta \to \nu_\alpha), \tag{1.4.11}$$

and:

$$\begin{aligned} P(\bar{\nu}_\alpha \to \bar{\nu}_\beta) = \delta_{\alpha\beta} \quad &- \quad 4\sum_{i>j} \Re(U^*_{\beta i} U_{\alpha i} U_{\beta j} U^*_{\alpha j}) \sin^2\left(\frac{\Delta m^2_{ij} L}{4E}\right) \\ &- \quad 2\sum_{i>j} \Im(U^*_{\beta i} U_{\alpha i} U_{\beta j} U^*_{\alpha j}) \sin\left(\frac{\Delta m^2_{ij} L}{2E}\right). \end{aligned} \tag{1.4.12}$$

Since $\bar{\nu}_\alpha \to \bar{\nu}_\beta$ is the CP-mirror image of $\nu_\alpha \to \nu_\beta$, then $P(\nu_\alpha \to \nu_\beta) \neq P(\bar{\nu}_\alpha \to \bar{\nu}_\beta)$ would imply CP violation. T violation can be tested if the probabilities of $\nu_\alpha \to \nu_\beta$ are different from the T conjugate process $\nu_\beta \to \nu_\alpha$. If CPT conservation holds then violation of T is equivalent to that of CP. Using U (eq. 1.4.3) it can be shown that CP violation in vacuum means that $\Delta P^{CP}_{\alpha\beta} = \Delta P^{T}_{\alpha\beta}$, where $\Delta P^{CP}_{\alpha\beta}$ and $\Delta P^{T}_{\alpha\beta}$ are [23]:

$$\begin{aligned} \Delta P^{CP}_{\alpha\beta} &= P(\nu_\alpha \to \nu_\beta) - P(\bar{\nu}_\alpha \to \bar{\nu}_\beta) \neq 0, \ (\alpha \neq \beta) \\ \Delta P^{T}_{\alpha\beta} &= P(\nu_\alpha \to \nu_\beta) - P(\nu_\beta \to \nu_\alpha) \neq 0, \ (\alpha \neq \beta), \end{aligned} \tag{1.4.13}$$

and that:

$$\Delta P^{CP}_{\alpha\beta} = \Delta P^{T}_{\alpha\beta} = -16 J_{\alpha\beta} \sin\left(\frac{\Delta m^2_{12} L}{4E}\right) \sin\left(\frac{\Delta m^2_{23} L}{4E}\right) \sin\left(\frac{\Delta m^2_{13} L}{4E}\right), \tag{1.4.14}$$

where:

$$J_{\alpha\beta} \equiv \Im(U_{\alpha 1} U^*_{\alpha 2} U^*_{\beta 1} U_{\beta 2}) = \pm c_{12} s_{12} c_{23} s_{23} c^2_{13} s_{13} \sin\delta, \tag{1.4.15}$$

with +(-) denoting cyclic (anticyclic) permutation of $(\alpha, \beta) = (e, \mu), (\mu, \tau), (\tau, e)$. It should be emphasised that from 1.4.15, for CP (or T) violation effects to be present, all the angles must be non-zero, and therefore a three-flavour mixing is essential. Hence, provided θ_{13} is nonzero[10] then $\delta \neq 0$, or $\delta \neq \pi$, allows the possibility of CP violation in the leptonic sector [23].

From equations 1.4.9 and 1.4.12 it can be seen that the observation that neutrinos can change from one flavour to another implies neutrino mass *and* mixing. In addition, it can be seen that the probability of flavour change in vacuum oscillates with L/E, and this behaviour led neutrino flavour change to be called "neutrino oscillation". Finally from equations 1.4.9, 1.4.12 and the unitarity of the U matrix it follows that the probability that a neutrino

---

[10] The Daya Bay θ_{13} measurement [27] was published after the conclusion of this thesis. Nonetheless, the result is mentioned in section 1.4 and table 1.1.

changes its flavour, plus the probability that it does not do so, is equal to one. Therefore the flavour change of neutrinos does not involve any change in the total flux[11] [26].

It has been shown that the mass of the second neutrino-mass eigenstate is larger than the mass of the first mass eigenstate. However, it is still not known whether the third mass eigenstate is heavier or lighter than the first two. If $m_{\nu_3} > m_{\nu_2} > m_{\nu_1}$ then the mass hierarchy is called "normal"[12], and if $m_{\nu_2} > m_{\nu_1} > m_{\nu_3}$ then the mass hierarchy is called "inverted" (illustrated in fig. 1.4).

The $\Delta m^2_{\odot} = \Delta m^2_{12}{>}0$ is responsible for the solar-neutrino oscillations, whereas $|\Delta m^2_A| = |\Delta m^2_{31}| \cong \Delta m^2_{32} \gg \Delta m^2_{21}$ is the neutrino mass-squared difference driving the dominant atmospheric-neutrino oscillations. $\theta_{12} = \theta_{\odot}$ and $\theta_{23} = \theta_A$ are the solar and atmospheric neutrino mixing angles respectively. θ_{13} is the so-called "mixed mixing angle"; it is constrained by the CHOOZ and Palo Verde data [3].

It should be noted that the recent results from T2K [28] and MINOS [29] suggest that $\theta_{13} \neq 0$ (for more information on the T2K results see section 1.5). Finally, the Daya Bay reactor neutrino experiment has measured a nonzero value for θ_{13}, with a significance of 5.2 standard deviations [27]. The best fit value is:

$$\sin^2 2\theta_{13} = 0.092 \pm 0.016(\text{stat.}) \pm 0.005(\text{syst.}). \tag{1.4.16}$$

This very important result opens the possibility of measuring CP violation in the lepton sector. Table 1.1 presents the current experimental status of the neutrino oscillation parameters.

---

[11] This statement does not take into account the possibility of neutrino flux becoming sterile neutrinos (hypothetical type of neutrino that only interacts via gravity). If some of the original neutrino flux transforms into sterile then an experiment which measures the total active neutrino flux (sum of ν_e, ν_μ, ν_τ fluxes), will find it to be less than the original flux.

[12] Note that $m_i \equiv m_{\nu_i}$.

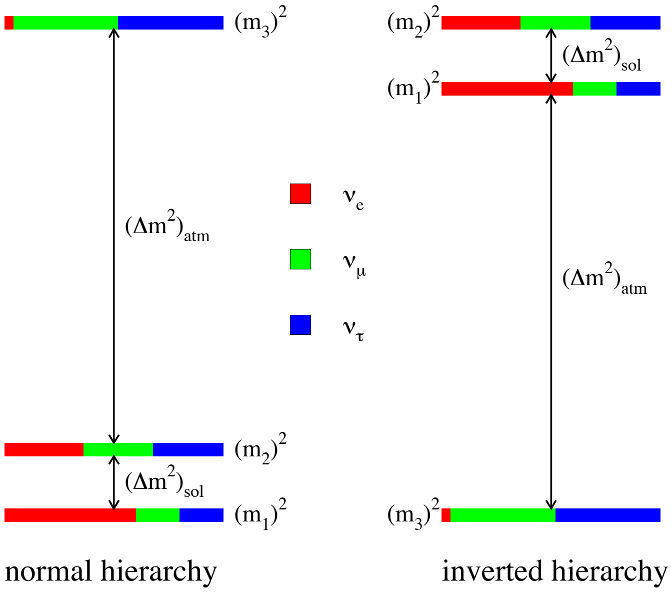

Figure 1.4.: Although it is shown that $m_{\nu_2} > m_{\nu_1}$, it is still not known if m_{ν_3} is heavier or lighter than the first two mass eigenstates. If m_{ν_3} is heavier then we get the normal (left diagram) and if it is lighter the inverse (right diagram) mass hierarchy. Red, green and blue represent the portion of ν_e, ν_μ and ν_τ each mass eigenstate consists of respectively.

Table 1.1.: Neutrino mixing parameters [30]. Values of Δm^2_{32} and $\sin^2(2\theta_{23})$ are from [29], and $\sin^2(2\theta_{13})$ from [27].

Parameter	**Value**
Δm^2_{21} $[10^{-5}]$ eV^2	7.59 ± 0.21
$\lvert\Delta m^2_{32}\rvert$ $[10^{-3}]$ eV^2	$2.32^{+0.12}_{-0.08}$
$\sin^2(2\theta_{12})$	$0.861^{+0.026}_{-0.022}$
$\sin^2(2\theta_{23})$	$> 0.90, 90\%$ C.L.
$\sin^2(2\theta_{13})$	0.092±0.016(stat.)±0.005(syst.)

1.4.1. Neutrino Oscillations in Matter

The propagation of neutrinos when traveling through matter can be significantly affected by their coherent forward-scattering from particles they encounter. Therefore, the probability of neutrinos changing flavour when they pass through matter, can be different than the one in vacuum. The flavour change that takes place in matter is described by the Mikheyev-Smirnov-Wolfenstein (MSW) effect.

The matter effect in the earth is a potential obstacle in measuring CP violation in long-baseline experiments. Therefore, the asymmetry between neutrino and antineutrino oscillations caused by matter effects, has to be separated from the neutrino-antineutrino asymmetry which arises from the genuine CP violation, as it is irrelevant to it. This separation will enable the study of the CP violation phenomenon (for additional theoretical background and equations see [31, 25, 32, 26]).

1.5. Neutrino Experiments Using Accelerator Sources

The full determination and precise measurement of neutrino oscillation parameters is possible only when using a human-made high intensity neutrino beam (>100 kW beam power). This beam can be characterised using beam monitors or a near detector placed close the production point ($\mathcal{O}$(1 km)), and then measured again at a far location which is placed at an adequate distance for the neutrinos to have undergone flavour change ($\mathcal{O}$(100 km))[13]. To date all long-baseline accelerator neutrino experiments have been using neutrinos coming from pion decay. Neutrino flavour change is studied at these long-baseline experiments either by measuring the ν_μ flux disappearance or by looking for appearance of ν_e or ν_τ events [24].

K2K [33] was the first long-baseline experiment, and was designed to verify the Super-Kamiokande observation of neutrino oscillations. K2K was followed by MINOS [34] and OPERA [35]. MINOS aimed at precisely measuring the atmospheric oscillation parameters and OPERA hopes to obtain direct confirmation of $\nu_\mu \rightarrow \nu_\tau$ oscillations.

The next-generation experiments are T2K [36] and NOνA [37]. T2K is designed to observe $\nu_\mu \rightarrow \nu_e$, and their collaboration announced the first θ_{13} result in June 2011: at 90% C.L. (confidence limit) their data are consistent with 0.03 (0.004)$<\sin^2 2\theta_{13} <$0.28 (0.34) for δ_{CP}=0 and normal (inverted) hierarchy (see fig. 1.4) [28]. Due to the fact that NOνA has a longer baseline than T2K, apart from measuring θ_{13}, this experiment may also be able to determine the mass hierarchy[14] [24].

Intense pion beams (super-beams) are utilised in ongoing and approved experiments to generate neutrinos. These experiments are designed to seek and measure θ_{13}, but have reduced sensitivity to matter-antimatter symmetry violation compared to the Neutrino Factory. Several neutrino sources have been conceived to reach high sensitivity, allowing, at the same time, the range of measurements that are necessary to remove the ambiguities in the determination of oscillation parameters. These experiments' sensitivity is beyond that

---

[13] These numbers assume measurement of $\Delta^2 m_{13}$ or $\Delta^2 m_{23}$.

[14] As the distance of the neutrino beam propagation through the earth increases, the mass hierarchy sensitivity increases.

of the presently approved neutrino-oscillation programme.

Studies so far have shown that the Neutrino Factory gives the best performance over all of the parameter space [1]. Fig. 1.5 presents the Neutrino Factory performance in terms of the 3σ discovery reach for CP violation (a), mass hierarchy (b) and $\sin^2 2\theta_{13}$ (c). This figure also presents the performance of a representative subset of alternative proposals. The discovery reach is presented in terms of the fraction of all possible values of δ, which is the "CP fraction", and plotted as a function of $\sin^2 2\theta_{13}$. The performance of the US "Long-baseline Neutrino Experiment" (LBNE) [38] served by the Project-X proton driver is also shown in the figure. In addition, the discovery reach that can be achieved by sending a neutrino beam from CERN is shown, using the superbeam generated by the SPL (Superconducting Proton Linac), or generated by the baseline beta-beam, or a combination of the two, assuming data taken in the MEMPHYS [39] water Cherenkov at Frejus. It is clear that the discovery reach of the Neutrino Factory is significantly better than that of the alternatives [40].

As mentioned above, the mass hierarchy sensitivity increases with the neutrino beam propagation distance through the earth. Additionally, the best CP violation sensitivity is found at large source-detector distances which require high neutrino energy, E_ν. Moreover, the neutrino beam divergence falls linearly and the neutrino-nucleon cross section grows linearly as E_ν grows. All these considerations indicate that the optimum sensitivity will be achieved with a facility that produces intense and high-energy ν and $\bar{\nu}$ beams [40].

The sub-leading $\nu_e \rightarrow \nu_\mu$ could be studied by providing intense ν_e beams. The two proposed techniques in which ν_e and $\bar{\nu}_e$ can be produced are the "beta beam" and the Neutrino Factory. In the beta beam, ions decay producing pure ν_e and $\bar{\nu}_e$ beams. However, as the neutrino carries only a small fraction of the ion's energy, it is necessary for the ion to be accelerated to very high energy in order for the neutrino to be produced with the required energy. Moreover, the ions' small charge-to-mass ratio makes the ion beams' rigidity significantly larger than the rigidity of proton or muon beams of the same energy. This implies that the systems required to accelerate and store the ions are of the scale of the Super Proton Synchrotron (SPS) at CERN or the Tevatron at the Fermi National Laboratory (FNAL) [40].

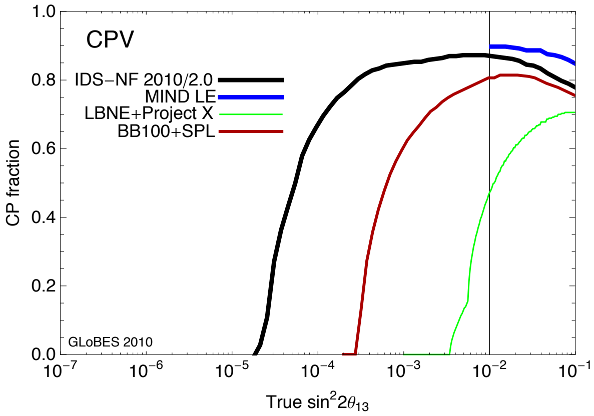

(a) CP violation

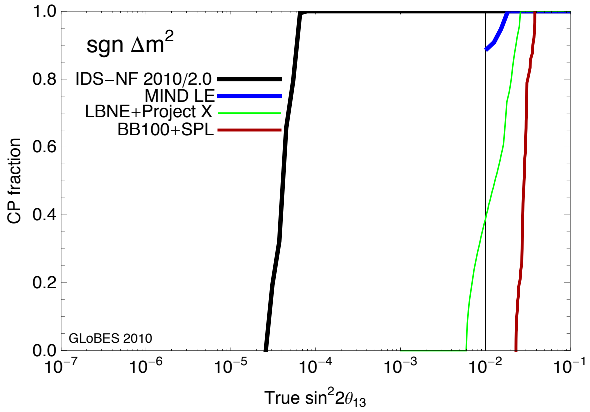

(b) Mass hierarchy

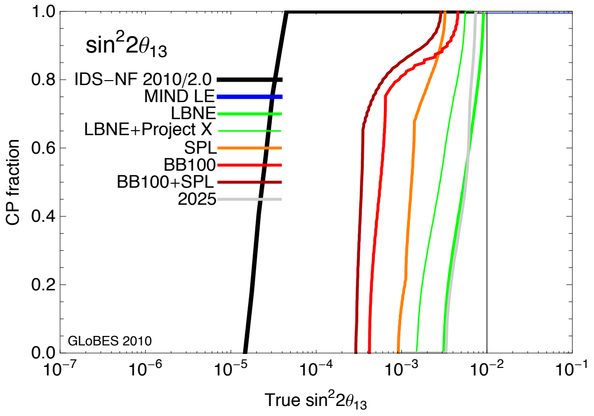

(c) $\sin^2 \theta_{13}$

Figure 1.5.: Physics reach comparison of different future facilities for the discovery of (a) CP violation, (b) the mass hierarchy, and (c) $\sin^2 \theta_{13}$. "True" $\sin^2 2\theta_{13}$ is the value of $\sin^2 2\theta_{13}$ assumed in the Monte Carlo simulations. IDS-NF refers to the baseline Neutrino Factory described in section 2. MIND LE (low energy) refers to a single baseline Neutrino Factory, optimised for large values of $\sin^2 2\theta_{13} > 0.01$. SPL stands for the Superconducting Proton Linac at CERN, BB100 for a beta-beam with $\gamma = 100$, and 2025 refers to the generation of experiments that are currently under construction. Figures taken from [40].

The Neutrino Factory will produce equal fluxes of ν_e and $\bar{\nu}_\mu$ from muons accumulated in the storage ring (equal fluxes of $\bar{\nu}_e$ and ν_μ will also be produced by μ^-). In this scenario, the muon charge-to-mass ratio is large and the neutrinos carry away a substantial energy fraction of the parent muon, hence high energy neutrinos can be easily produced. In the Neutrino Factory, fast acceleration together with time-dilation allow enough time to manipulate the muon beam, producing a pure, almost mono-chromatic, well collimated muon beam.

As shown in fig. 1.5, the Neutrino Factory has an excellent precision and outstanding discovery reach; furthermore it has a great sensitivity to non-standard neutrino interactions[15]. Therefore, the Neutrino Factory is a facility of choice for precise neutrino oscillation measurements.

1.6. Ionisation Cooling

In the International Design Study for the Neutrino Factory [40], the baseline accelerator facility provides 10^{21} muon decays per year. The muon beam, produced from pions decaying in flight, has a very large initial transverse emittance, and therefore in order for the muon beam to be efficiently accelerated in downstream accelerator systems its divergence needs to be decreased, or cooled. Due to the short muon lifetime the only viable technique for transverse emittance reduction is *ionisation cooling*: the beam passes through absorbers and loses momentum in every direction by ionising the absorber's material and the lost energy is restored only longitudinally when the beam passes through RF cavities. By repeating this procedure, the transverse emittance of the beam is reduced. A particle is considered to be within the acceptance of the machine if the transverse emittance is less than 0.03 π·m·rad and the longitudinal amplitude squared is less than 0.15 m. The equations that govern ionisation cooling are given in chapter 3.

---

[15] Non-standard neutrino interactions, NSI's, are new interactions of neutrinos (Standard Model extensions) at the source, detector or with matter. For more information on NSI's see [41, 42].

Chapter 2

Neutrino Factory

2.1. Experimental Layout

The Neutrino Factory accelerator complex, illustrated in fig. 2.1, will produce the most intense and high-purity neutrino beam that has ever been achieved. The neutrino beam will have a very well-known energy spectrum, without being contaminated by unwanted neutrino flavours.

At source, the Neutrino Factory beam will contain equal fluxes of ν_e and $\bar{\nu}_\mu$, from μ^+ circulating in the storage ring[1]. Equal fluxes of $\bar{\nu}_e$ and ν_μ will also be produced with μ^- in the storage ring. The oscillation channels that will be available at a Neutrino Factory are listed in table 2.1. The "golden channel" will produce muons of opposite charge to that of the stored muons. Therefore a magnetised detector is needed to distinguish the golden channel signal from the background, produced by unoscillated ν_μ. Furthermore, the ability of detection of the "silver" and "platinum" channels is what makes the Neutrino Factory the ideal place to look for oscillation phenomena.

Table 2.1.: Oscillation processes in the Neutrino Factory [40].

$\mu^+ \to e^+\nu_e\bar{\nu}_\mu$	$\mu^- \to e^-\bar{\nu}_e\nu_\mu$	Process
$\bar{\nu}_\mu \to \bar{\nu}_\mu$	$\nu_\mu \to \nu_\mu$	disappearance
$\bar{\nu}_\mu \to \bar{\nu}_e$	$\nu_\mu \to \nu_e$	appearance: "platinum" channel
$\bar{\nu}_\mu \to \bar{\nu}_\tau$	$\nu_\mu \to \nu_\tau$	appearance (atmospheric oscillations)
$\nu_e \to \nu_e$	$\bar{\nu}_e \to \bar{\nu}_e$	disappearance
$\nu_e \to \nu_\mu$	$\bar{\nu}_e \to \bar{\nu}_\mu$	appearance: "golden" channel
$\nu_e \to \nu_\tau$	$\bar{\nu}_e \to \bar{\nu}_\tau$	appearance: "silver" channel

---

[1] The storage ring is often referred to as "decay ring".

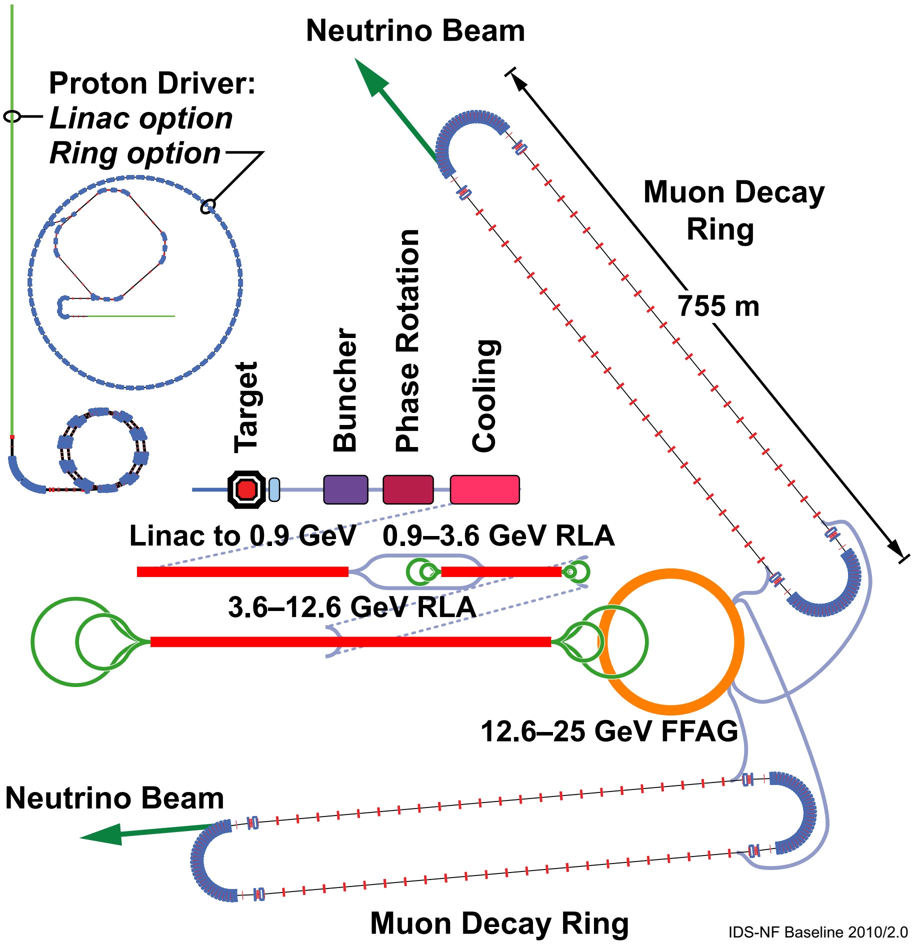

Figure 2.1.: Schematic layout of the IDS-NF baseline for the Neutrino Factory accelerator complex. The various systems have been drawn to scale. Figure taken from [40].

The Neutrino Factory consists of several accelerator subsystems: firstly a high-power proton beam hits a liquid mercury jet target, inside a 20 T solenoid, producing pions. The pions will then decay in flight in a long decay channel producing a muon beam with a large energy spread. An energy-time correlation is built-up by allowing the beam to pass through a dedicated drift space. The "Buncher" follows, which consists of a sequence of RF cavities, turning this distribution into a number of bunches. Further downstream the energy spread between the bunches is reduced with the "Phase Rotator". An ionisation cooling channel follows the bunching and phase-rotation sections which reduces the transverse phase-space of the muon beam, increasing in this way the number of muons that can be transmitted into downstream accelerator systems. The muon beam acceleration occurs in several stages: first a linac accelerates the beam to 0.9 GeV total energy. Then two recirculating linear accelerators (RLAs) increase the beam energy to 3.6 and 12.6 GeV respectively. Finally, the beam is accelerated to 25 GeV by a fixed field alternating gradient (FFAG) accelerator. The muon beam is then injected into two decay rings that point towards the far detectors.

The set-up of the Neutrino Factory baseline was derived by optimising the stored-muon energy and the distance from the source to the two distant detectors. The performance of the facility was optimised for the discovery of leptonic CP violation, the mass hierarchy, and the precise determination of θ_{13}. A detector placed at the "magic baseline" (7,000-8,000 km from the source), capable of detecting the golden channel with high efficiency, has excellent sensitivity to the mass hierarchy, $\sin\theta_{13}$ and θ_{23}. The best sensitivity to CP violation, obtained at a source-detector distance ∼3,000-5,000 km, requires a stored-muon energy in excess of 20 GeV. In addition, the sensitivity to non-standard interactions at the Neutrino Factory also improves as the stored-muon energy increases, with a plateau at ∼25 GeV. Therefore, the adopted stored muon energy is 25 GeV. It should be emphasised there are a number of possible sites for the source and detectors that would allow the IDS-NF[2] baseline Neutrino Factory configuration to be implemented. With the recent Daya Bay θ_{13} measurement, a low energy Neutrino Factory is being considered with a E_{μ}=10 GeV and a single baseline as described in the IDR (International Design Report) [40, 44].

2.2. Proton Driver

At the Neutrino Factory, the Proton Driver is required to deliver a 4 MW proton-beam at a repetition rate of 50 Hz to the pion production target to reach the goal of 10^{21} muons per year. In order to maximise the pion, and therefore the muon yield, the proton-beam energy must be in a multi-GeV range. The specified time structure consists of three short bunches separated by 120 μs, and in order for the muon beam to be efficiently captured, the bunches are required to be 1-3 ns RMS short. Each bunch of the proton driver will become a separate muon bunch train. Table 2.2 presents the proton beam parameters, necessary to produce the desired number of muons in the storage rings of the Neutrino Factory. Several proton-driver schemes have been proposed, consisting of a H^{-}-ion source followed by a radio-frequency quadrupole (RFQ), a chopper and a linac accelerator, which delivers the final energy of the proton-driver.

A linac-based solution was adopted for the CERN Neutrino Factory scenario, based on the proposed 5 GeV, high-power version of the Superconducting Proton Linac (SPL), that can deliver 10^{14} protons at a repetition rate of 50 Hz. Additional accumulator and compressor rings will be needed to provide the

---

[2] IDS-NF: International Design Study for a Neutrino Factory [43].

Table 2.2.: Proton Driver Requirements. Taken from [40].

Proton driver requirements	
Parameter	**Value**
Kinetic energy	5-15 GeV
Average beam power	4 MW
Repetition rate	50 Hz
Bunches per train	3
Total time for bunches	240 μs
Bunch length	1-3 ns
Beam radius	12 mm (RMS)
RMS geometric emittance	$<$5 μm
β^* at target	$\geq$ 30 cm

correct time structure. More details of the CERN proton driver scenario can be found in [40, 45].

A proton driver for a Neutrino Factory situated at Fermilab will be based on a proposed Project X linac. Project X, currently being designed, will be a high-intensity proton source that will deliver beam at 3 and 8 GeV. The Project X linac will only deliver ~10% of the proton-beam power needed for the Neutrino Factory at 8 GeV. Nevertheless, Project X is designed in a way that can be upgraded to deliver the full beam power required for the Neutrino Factory (4 MW at 8 GeV). Similarly with the CERN scheme, additional accumulator and compressor rings will be needed to provide the correct time structure. For more information on this scenario see Appendix A of [40].

A Neutrino Factory sited at the Rutherford Appleton Laboratory (RAL), will be served by a proton driver based on an ISIS pulsed-proton source upgrade. In this scenario, a chain of circular accelerators provides an alternative to the linac-based options which are outlined above. For more details on the Neutrino Factory proton driver option that is based on a RAL facilities upgrade see Appendix B of [40].

2.3. Target

The Neutrino Factory pion-production target should be capable of operating with a 4 MW pulsed proton beam with a repetition rate of 50 Hz. The latest[3] design of the baseline target system, shown in fig. 2.2, is based on a free liquid-mercury jet, the effectiveness of which has been successfully tested at

---

[3] A different layout is shown in [40]. However, energy deposition studies showed that much more shielding was required and therefore a redesign of the target system was needed.

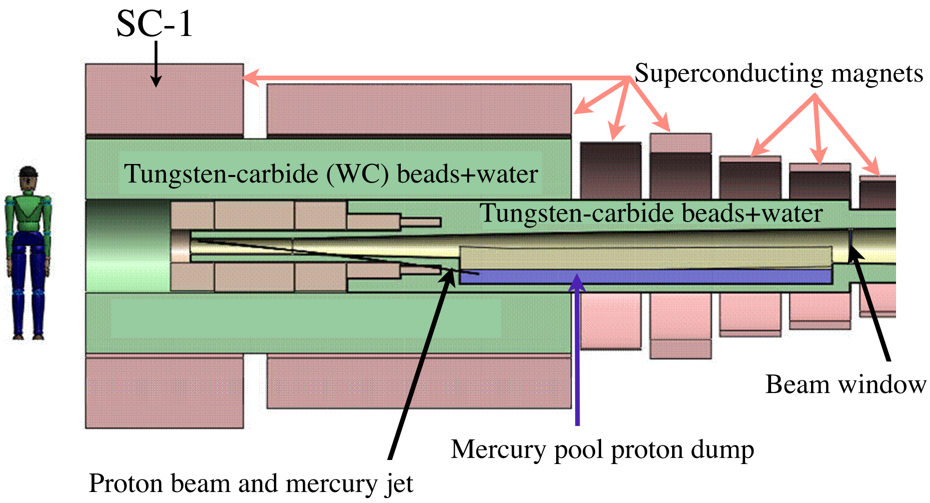

Figure 2.2.: Proposed updated baseline target system. SC-1 is the first superconducting magnet and WC stands for “water cooled”. The Tungsten-carbide beads and water are the shield; the heat exchanger is not shown here. Figure taken and edited from [48].

the MERIT experiment [46]. The parameters of the current target-system, which have been determined by simulations using the MARS code [40], are summarised in table 2.3. For an updated comparison of the target and pion capture systems simulations see [47].

Solenoids, rather than toroidal magnets[4], will be used in order to capture pions of both signs. The target, the proton beam dump and the shield/heat exchanger will be located inside a channel of superconducting solenoidal magnets that capture, confine and transport secondary pions and their decay muons to the muon front-end.

To date, there are four alternatives to the liquid-mercury jet target: a liquid metal jet,using a metal that is solid at room temperature (Lead-Bismuth), helium-cooled metallic low-Z static packed beds [49], a metal powder jet, and a system of solid tungsten bars that are exchanged between beam pulses [40]. There is also a new idea of using a Gallium target, since Gallium is liquid at room temperature. For more details on the updated target design see [50].

2.4. Muon Front-End

The muon front-end consists of a pion decay channel, a buncher, a phase-rotator and a cooling channel. It is responsible for matching the beam produced from the target to the accelerator system.

---

[4] Toroidal magnets are typical in target systems for “conventional” neutrino beams. They primarily capture particles of only one sign [40].

Table 2.3.: Baseline target system parameters. Values taken from [40].

Parameter	**Value**
Target type	Free mercury jet
Jet diameter	8 mm
Jet velocity	20 m/s
Jet/solenoid axis angle	96 mrad
Proton beam/solenoid axis angle	96 mrad
Proton beam/jet angle	27 mrad
Capture solenoid (SC-1) field strength	20 T
Front-end π/μ transport channel field strength	1.5 T
Length of transition from 20 T to 1.5 T	15 m

The pions produced in the target, and the muons they decay into, have a wide energy range (100-300 MeV) in a short time pulse (~3 ns RMS). In order for the muons to be efficiently accelerated in subsequent RF cavities, the longitudinal phase-space must change, and therefore a drift, buncher and a phase rotator are used (shown in fig. 2.3). Moreover, the muons produced from pion decays have large transverse emittance, which needs to be decreased in order for the muons to be efficiently transported into downstream accelerator systems; an ionisation cooling channel therefore follows the phase-rotation system.

2.4.1. Pion Decay Channel

The initial proton bunch is relatively short resulting in short pion bunches. As the secondary pions travel from the target with a large energy spread, they drift longitudinally in a 57.7 m RF-free drift channel (or decay channel). Therefore these pions and their daughter muons develop a position-energy correlation in the decay channel [40]; the higher energy particles are at the head and the lower energy particles at the tail of the bunch (see fig. 2.3).

In this channel, the magnetic field is adiabatically reduced from 20 T to 1.5 T over a distance of 15 m. Within this distance, the radius of the beam pipe increases from 0.075 m to 0.3 m. This arrangement captures a secondary pion beam with a large energy spread. At the end of this decay channel, there are ~0.4 muons of each sign per incident 8 GeV proton.

2.4.2. Buncher and Phase Rotator

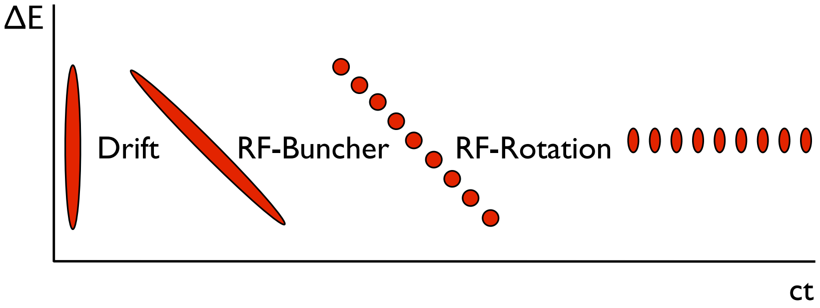

Figure 2.3.: The longitudinal phase-space of the muon beam can change using a drift, Buncher and Rotator. Pions and their daughter muons develop an energy-position correlation when passing through a drift channel. A train of muon bunches is created by the Buncher. The downstream Rotator reduces the energy spread and increases the time spread of the muon beam. Note that the diagram could be misleading as it shows the lower energy bunches moving further than the high energy ones; what really happens is that the low energy bunches arrive later in *time*.

Downstream of the drift channel, the buncher forms the muon beam into a train of bunches using RF cavities, suitable for capture and acceleration in a 201 MHz RF system. The frequencies of the RF cavities decrease from 320 to 232 MHz along the 33 m long Buncher, while the gradient increases from 0 to 9 MV/m. There is still a substantial energy correlation in the resultant bunch train, as the higher energy bunches are first, followed by progressively lower energy bunches [51, 52].

The buncher is followed by an energy-rotating section where the leading high-energy bunches are decelerated and the late low-energy bunches are accelerated, forming in this way bunches with the same momentum of 232 MeV/c. The bunch train delivered by the buncher is less than 80 m long. The rotator uses 0.5 m long RF cavities with gradient at 12 MV/m placed in a 0.75 m long solenoidal field, and the RF frequency decreases from 230.2 MHz to 202.3 MHz along the 42 m long rotator region. This phase rotation increases the accepted muons by a factor of four.

2.4.3. Cooling

The baseline cooling channel is formed by a sequence of 1.5 m identical cells. Each cell consists of two 0.5 m-long 201 MHz normal conducting RF cavities that have 1.1 cm thick LiH absorber discs placed at both ends of each cavity. Two coils of opposite polarity are placed in each cell, producing a magnetic field with a peak-value of 2.8 T. The total length of the cooling section is assumed to be 75 m, which was decided based on simulation results. It is expected that the cooling channel will reduce the RMS[5] transverse normalised emittance by a factor of 2.4, from ϵ_N= 0.018 m to ϵ_N=0.0075 m [40]. The RMS longitudinal emittance is $\epsilon_L = 0.07$ m/bunch.

The ionisation cooling technique assumed in the cooling section still needs to be demonstrated, which is the aim of the Muon Ionisation Cooling Experiment (MICE) [53]. The cooling will be experimentally verified over a range of muon beam momenta, initial emittances and absorber materials, which will be used for the final optimisation of the Neutrino Factory cooling channel. A more detailed description of MICE follows in chapter 4.

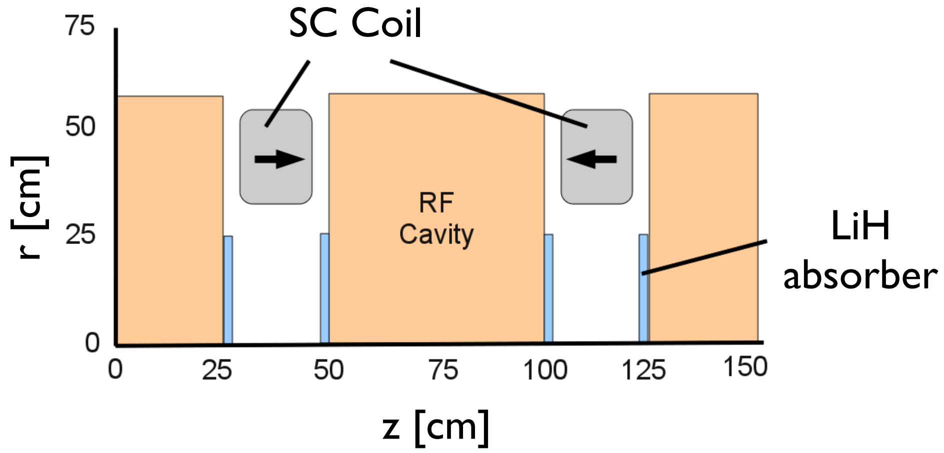

Figure 2.4.: Radial cross-section of the Neutrino Factory baseline cooling cell. Figure taken and edited from [40].

2.5. Accelerators

The muon acceleration chain in the Neutrino Factory consists of a linac, two recirculating linacs (RLAs) and an FFAG. This accelerator chain will increase the energy of the muon beam exiting the ionisation cooling channel from ∼0.24 GeV to 25 GeV.

2.5.1. Linac and RLA

The acceleration starts downstream of the ionisation cooling channel, where the beam energy will increase from ∼0.24 GeV to 12.6 GeV. In order for an

---

[5] RMS emittance is defined in section 3.3.

effective acceleration to be possible in the RLA, a linear pre-accelerator (or simply linac) decreases the large phase-space of the muon beam adiabatically, while accelerating it to relativistic energies. The RLA then further compresses and shapes the beam phase-space while increasing the energy. The proposed "dog-bone" configuration of the RLAs facilitates simultaneous acceleration of both muon species. The linac uses superconducting iron-shielded solenoids whereas the RLAs use Alternating Gradient (AG) focusing; both, linac and RLAs use 201.25 MHz Niobium (Nb) sputtered superconducting RF cavities for acceleration, to minimise the cost.

A single pass in the linac raises the muon beam energy from ∼0.24 GeV to 0.9 GeV. As a result, the muons are sufficiently relativistic to obtain further acceleration in the RLA. A double chicane, "chicane 1", transfers the muons from the linac to RLA I, where the beam will perform 4.5 passes at an average gain of 0.6 GeV/pass. A second double chicane, "chicane 2", transfers the 3.6 GeV beam to RLA II where the beam again performs 4.5 passes, only this time the average energy gain is 2 GeV/pass. When the beam reaches 12.6 GeV it is directed towards and injected into the FFAG [40]. A schematic of the linac and RLAs is shown in figure 2.5.

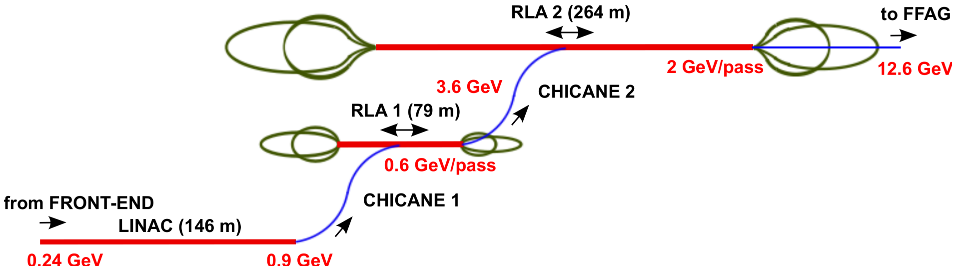

Figure 2.5.: Layout of the linac and recirculating linacs (RLAs) for the Neutrino Factory, connected by chicanes. Figure taken from [40].

2.5.2. FFAG

For the final part of acceleration, a machine that will allow a large energy range within a fixed-field arc is needed, so that the muons will be accelerated to the desired energy quickly enough, before they decay. Therefore, the final acceleration component is chosen to be a Fixed Field Alternating Gradient (FFAG) accelerator. In order to keep the machine's cost low and to allow the use of fixed frequency 201.25 MHz RF cavities, a linear non-scaling (NS), rather than scaling, FFAG will be used. The scaling FFAG employs a nonlinear variation of the average magnetic field, whereas in the NS-FFAG the magnetic field variation is linear. The linear magnetic field variation results in a large dynamic aperture, allowing the acceleration of large emittance beams.

Moreover, the orbit excursion, and hence the magnet aperture, can be much smaller than in other fixed field accelerators, which is cost-effective. Another important aspect of this kind of accelerator is that a fixed frequency RF system can be used, thanks to the quasi-isochronous optics[6] minimising the time of flight variation as a function of muon energy. This allows for a rapid beam acceleration within ∼11 turns over the entire energy range [54]. Finally, the magnets of the NS-FFAG are more compact than those of a comparable scaling FFAG [40]. The principles of NS-FFAG are now being tested at the Electron Model for Many Applications (EMMA) experiment [55, 54], the world's first NS-FFAG, located at the STFC Daresbury Laboratory, UK. The first result of EMMA, published in [56], showed that the principle of NS-FFAG is working.

2.6. Decay Ring

In the Neutrino Factory, neutrinos are generated from muon decays according to $\mu^- \rightarrow e^-\bar{\nu}_e\nu_\mu$ and $\mu^+ \rightarrow e^+\nu_e\bar{\nu}_\mu$. Muons will be accumulated into storage rings with long straight sections pointing at far detectors where neutrinos will be sent. The storage rings dip into the ground with the large angles of 18^o, pointing to the intermediate detector at ∼4,000 km distance, and 36^o, pointing to the far detector at ∼7,500 km.

---

[6] In the isochronous optics the time difference between particles of different energies is zero, i.e. Δt is constant with energy; in the quasi-isochronous optics, Δt has a parabolic behaviour with energy.

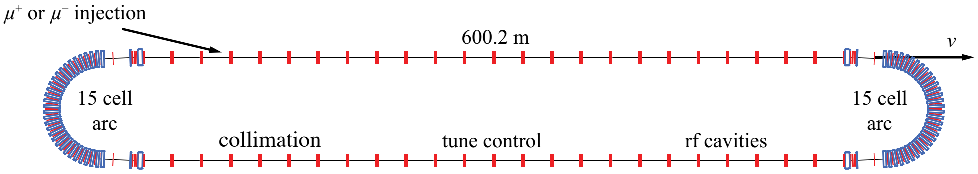

(a) Racetrack design for the Neutrino Factory storage rings. Figure taken and edited from [40].

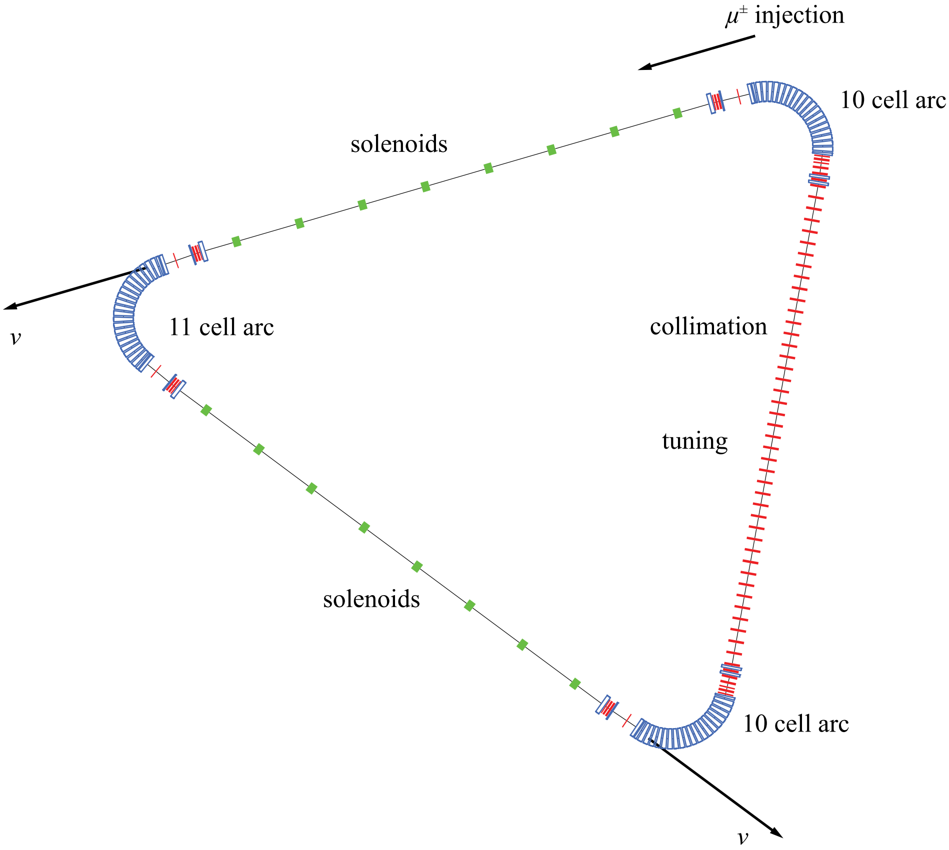

(b) Muon storage ring of triangular shape able to send neutrinos to detectors in two different directions. Figure taken from [40].

Figure 2.6.: Storage rings for the Neutrino Factory.

A racetrack and a triangular design have been considered. The racetrack option, shown in fig. 2.6a, was designed to store muons or anti-muons with a single straight section pointing into the ground and with the return straight section used for collimation, RF and tune control. This development can accommodate counter-rotating muons of both signs. An alternative is a triangular lattice (fig. 2.6a) with two production straights pointing to different directions; in this way the neutrinos will be sent to two detectors simultaneously. As the beam has to travel in a unique direction, two triangular rings would be built side by side in the same tunnel, each serving each muon sign. The maximal tunnel depths for rings of this size are 444 m for the racetrack and 493 m for the triangle. The racetrack design has been chosen as the baseline [40].

2.7. Detectors

2.7.1. Far Detectors

In order to optimise for δ, θ_{13}, and the sign of Δm^2_{13} (which will determine the mass hierarchy), two Magnetised Iron Neutrino Detectors (MIND) are needed. The first one should be of a 100 kTon fiducial mass, and placed at ~4,000 km from the decay point, and the second, which is called the "magic baseline", should be placed at ~7,500 km. The "magic baseline" term is used as matter effects cancel the CP violation effect at this distance of propagation through the Earth. This detector is optimised to carry out the "golden channel" ($\nu_e \rightarrow \nu_\mu$) through the wrong-sign muon signature[7]. This strategy provides better sensitivity than e.g. measuring the "golden" and "silver" ($\nu_e \rightarrow \nu_\tau$) channels simultaneously. This strategy is also more efficient for resolving degeneracies[8] in the neutrino oscillation formulae.

A cuboidal geometry has been adopted with a cross-sectional area of 15×15 m^2 and length between 63 m and 125 m, depending on the detector's mass. Each iron plane is of 3 cm thickness, followed by two planes of scintillator of 1 cm thickness each. These three planes form a module of 5 cm thickness. The resolution requirement is 1 cm, provided by having co-extruded scintillator bars 15 m long and 3.5 cm wide, read out using optical fibres and silicon photomultipliers (SiPMT). This baseline uses 1 T dipole field. The key parameters of the two far detectors are shown in table 2.4. It should be noted that 1 T dipole field is not practical from an engineering point of view, and therefore a more realistic octagonal geometry (14 m octagonal iron plates, 3.0 cm thick) is studied, with a toroidal field[9] between 1 T and 2.2 T over the whole fiducial area. A 3D diagram of a MIND plate is shown in fig. 2.7. For more information on the iron plates, magnetisation, scintillator, photo-detector and electronics, see section IIIB1 of [40].

---

[7] In the $\nu_e \rightarrow \nu_\mu$ oscillation a muon of opposite charge to that stored in the storage ring (wrong-sign muon) would be produced in a far detector by the charge current (CC) interactions of the oscillated ν_μ. By using magnetised detectors the two muon signs can be discriminated.

[8] The problem of neutrino oscillation parameter degeneracy describes the fact that a set of measurements of the oscillation probabilities and its CP conjugate (e.g. $P(\nu_\mu \rightarrow \nu_e)$ and $P(\bar{\nu}_\mu \rightarrow \bar{\nu}_e)$) at a particular neutrino energy (no matter how accurate the measurement is), does not uniquely determine the values of θ_{13} and δ. For more information on these degeneracies see [57, 58].

[9] The toroidal field of MIND will be like that of MINOS [34].

Table 2.4.: Baseline parameters for the Magnetised Iron Neutrino Detectors (MIND). MIND 1 refers to the detector at ∼4,000 km and MIND 2 to the detector located at ∼7,500 km.

Parameter	**MIND 1**	**MIND 2**
Distance (km)	3000-5000	7000-8000
Fiducial mass (kTon)	100	50
Size iron plates (cm^3)	1400×1400×3	1400×1400×3
Detector length (m)	125	62.5
Number of iron plates	2500	1250
Dimensions scintillator bars (cm^3)	1500×3.5×1	1500×3.5×1
Number scintillator bars per plane	429	429
Total number of scintillator bars	2.14×10^6	1.07×10^6
Total number of readout channels	4.28×10^6	2.14×10^6
Photon detector type	SiPMT	SiPMT
Magnetic field (T)	>1	>1

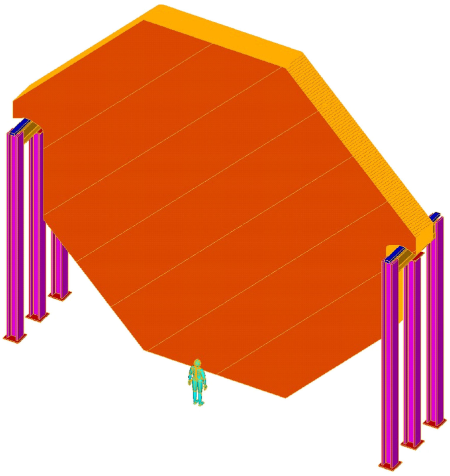

Figure 2.7.: 3D diagram of MIND plate. Figure taken from [40].

2.7.2. Near Detectors

Four near detectors are required, as each straight section of the storage ring requires one near detector at each of the two polarities. These four detectors will be designed to carry out measurements essential for the neutrino oscillation analysis, that include measurement of neutrino-electron scattering (for the determination of the neutrino flux), the neutrino-beam properties (required for the flux to be extrapolated with accuracy to the far detectors), the charm production cross sections (charm production in far detectors is one of the principal backgrounds to the oscillation signal), and measurement of the neutrino-nucleon deep inelastic, quasi-elastic, and resonant-scattering cross sections.

As a result of the intense neutrino beam delivered by the Neutrino Factory, a unique neutrino-physics programme can be carried out at the near detector. The general design features of the near detector are micron scale resolution for charm and tau identification, low atomic number and a high-resolution target, and a magnetic field for charged particle momentum measurement. In addition the near detectors will have electron identification capabilities, and excellent energy resolution for flux extrapolation (goal is to achieve $\delta E/E \sim 1\%$). Finally the detectors will use different nuclear targets to measure cross-sections in iron and as a function of the nuclear target mass number.

The two options currently being considered are one that includes a high resolution scintillating fibre tracker, and one that includes a transition-radiation straw-tube tracker. Both options will be studied in order for their capabilities to be determined.

Chapter 3

Theoretical Introduction in Accelerator Physics

Accelerators are devices that increase the energy of charged particles using electromagnetic fields. The early particle accelerators were motivated by nuclear physics; now they have a wide variety of applications. Accelerators can be used for elementary particle physics, nuclear physics research, in material science, and in fusion reactor experiments. Moreover, accelerators are used for medical purposes, for oil and natural gas exploration, and for food sterilisation [59]. This section provides a theoretical introduction in the physics of accelerators.

A beam of charged particles is directed to an ideal predescribed path along a desired beam transport line, or along a closed orbit in case of circular accelerators. The forces that guide the charged beam to the ideal path are the Lorentz forces, and they are derived from the electric and magnetic fields, $\vec{E}$ and $\vec{B}$, through the Lorentz equation:

$$\frac{d\vec{p}}{dt} = \vec{F} = q(\vec{E} + \vec{u} \times \vec{B}), \tag{3.0.1}$$

where q is the electric charge, $\vec{p} = \gamma m \vec{u}$ is the momentum, $\vec{u}$ is the velocity, m is the invariant mass and γ is the Lorentz factor:

$$\gamma \equiv \frac{1}{\sqrt{1 - \frac{u^2}{c^2}}} \tag{3.0.2}$$

with $u \equiv \sqrt{\vec{u} \cdot \vec{u}}$. The charged particles are accelerated by the electric field, whereas both the magnetic and electric fields change their orbit (here acceleration implies change of speed, not of orbit, with time). $\vec{E}$ and $\vec{B}$ must satisfy Maxwell's equations, which in a vacuum are (differential form):

$$\nabla \cdot \vec{E} = \frac{1}{\epsilon_0} \rho(\vec{r}, t), \tag{3.0.3}$$

$$\nabla \cdot \vec{B} = 0, \tag{3.0.4}$$

$$\nabla \times \vec{E} = -\frac{\partial \vec{B}}{\partial t}, \tag{3.0.5}$$

$$\nabla \times \vec{B} = \mu_0 \vec{j}(\vec{r}, t) + \frac{1}{c^2} \frac{\partial \vec{E}}{\partial t}, \tag{3.0.6}$$

where ρ is the charge and $\vec{j}$ is the current density [59].

As mentioned above, the Lorentz forces are applied to guide the particles along a predefined path as well as to focus the beam to a narrow vicinity of the ideal path. The terms *beam dynamics* or *beam optics* refer to the evolution of particle trajectories under the influence of Lorentz forces. The collection of bending and focusing magnets installed along the ideal path is called the *magnet lattice*, and the complete optical system that will transport the beam from point A to point B, including the bending and focusing parameters, is called a *beam transport system* [59].

3.1. Synchrotron Oscillations

The first particle accelerators were electrostatic accelerators (DC accelerators), in which the beam gains energy from a constant electric field. However, these type of accelerators face a limitation of their maximum achievable energy and are therefore usually used for low energy (MeV scale) acceleration (Cockcroft-Walton, Van de Graaff, etc) [59, 60, 61].

On the other hand, oscillating field accelerators use radio-frequency (RF) cavities. An RF cavity accelerates traversing particles with the use of standing waves, the frequency of which is chosen such as to give an accelerating "push" to particles that pass through. For instance, if a series of negative charged bunches passes through an RF cavity, the sign of the RF wave will flip from positive to negative when the bunch passes through the cavity, in order to repulse the bunch; the sign will then flip back to positive as the new bunch arrives, in order to attract it. RF cavities are the core ingredient of every accelerator, and the dominant machine component of a linear accelerator [62, 63].

The RF acceleration cavity provides a longitudinal electric field at an RF frequency that ranges from a few hundred kHz to 10-30 GHz. The energy gain or loss per passage through a cavity gap for a particle with charge e is:

$$\Delta E = e\Delta V T_t, \tag{3.1.1}$$

where $\Delta V = V_0 \sin(\omega t + \phi)$ is the effective voltage, ω is the angular RF frequency, V_0 is the effective peak accelerating voltage and ϕ is the phase angle (defined below) [60]. T_t is the transit time factor:

$$T_t = \frac{\sin\left(\frac{\omega\lambda_{RF}}{4u}\right)}{\frac{\omega\lambda_{RF}}{4u}}, \tag{3.1.2}$$

where u is the particle's velocity and λ_{RF} the wave length of the RF cavity. For large velocities the transit time factor is $T_t \approx 1$.

The ideal particle, or *synchronous* particle, is the one that, at each moment of time, has the right energy and time (or phase) of passage through the accelerating structure to receive exactly the right increment of energy. This specific phase is called the *synchronous phase*, and is defined as:

$$\phi_s = \omega t - kz = constant, \tag{3.1.3}$$

where ω, as mentioned above, is the oscillating frequency of the RF field, k is the RF wave number, and z is the distance along the beam-axis. Since $dz/dt = \beta c$, the time derivative of eq. 3.1.3 gives the synchronicity condition:

$$\dot{\phi_s} = \omega - k\beta c = 0, \tag{3.1.4}$$

and therefore ω is equal to:

$$\omega = k\beta c = \frac{2\pi}{L}\beta c, \tag{3.1.5}$$

where L is the distance between two consecutive accelerator stations. Obviously, any integer multiple of the frequency ω satisfies the synchronicity condition:

$$\omega_h = h\omega = k_h \beta c = \frac{2\pi}{L} h\beta c, \tag{3.1.6}$$

where h is an integer called the harmonic number, and $k_h = hk$. This condition can be applied to a circular accelerator as well, where one would replace L with $2\pi R$, R being the radius of the circular accelerator [64]. The harmonic number is often chosen for practical reasons: to increase the RF frequency, or to keep the cavity's dimensions and wave-guides reasonably small [65].

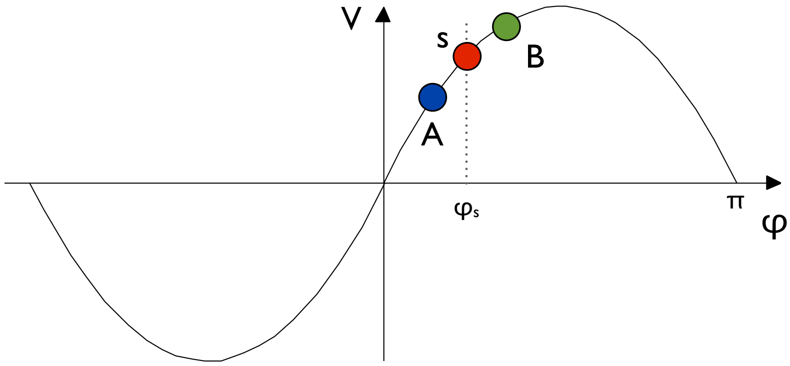

(a) The synchronous particle, s, arrives at time t_s at the first cavity, whereas a fast particle A arrives at a smaller phase (time), and a slow particle B at a later time.

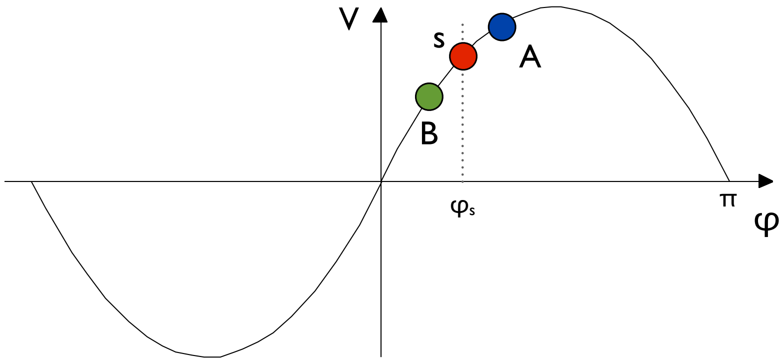

(b) In the next cavity, the synchronous particle will again arrive at t_s, whereas B will arrive at a smaller time and A will arrive later.

Figure 3.1.: Voltage with respect to phase in an accelerator showing how synchrotron oscillations work. Particles A and B oscillate about the synchronous particle, s.

In fig. 3.1 three particles are shown: the synchronous particle (s), a slow (B) and a fast particle (A). The synchronous particle arrives at the cavity at time t_s. The fast particle, A, arrives at $t_\alpha < t_s$ and gains energy $\Delta E_\alpha < \Delta E_s$, whereas the slow particle, B, arrives at $t_b > t_s$ and gains energy $\Delta E_b > \Delta E_s$ (fig. 3.1a). According to its definition, the synchronous particle will arrive at the next cavity at the same phase, ϕ_s. However, since A gained less energy and velocity it will arrive later than s at the next cavity, while B, which gained higher energy, will arrive earlier. The repetition of this procedure results in an oscillation of A and B in phase-space about the synchronous particle [66]. Since these oscillations were first analysed for the synchrotron, they are called *synchrotron oscillations* [59].

The longitudinal phase-space is formed by the variables ΔE and Δt (or $\Delta\phi$), where $\Delta E = E_p - E_{ref}$ is the difference in energy between a particle and the reference (or synchronous) one (similarly for time, $\Delta t = t_p - t_{ref}$). These variables, evaluated at subsequent RF cavities trace out an ellipse, the shape of which depends on the RF phase (see fig. 3.2). The longitudinal emittance, ϵ_L, is the area of this ellipse devided by π.

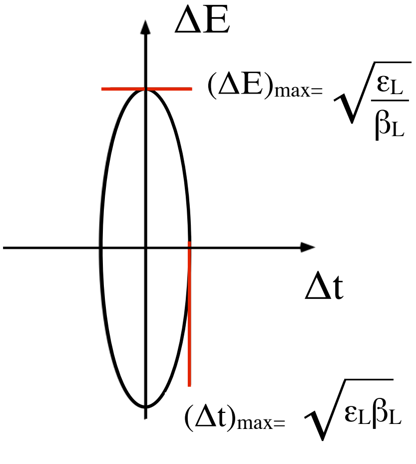

Figure 3.2.: Longitudinal phase-space ellipse, representing the energy and time (phase) difference between a particle and the reference (synchronous) particle. β_L is the longitudinal betatron function (betatron function is defined in sec. 3.3.). Figure taken and edited from [66].

Liouville's theorem (described in more detail in section 3.3) implies conservation of the phase-space area. Since the local phase-space density in the longitudinal phase-space stays constant, ϵ_L stays constant even if the synchronous energy, velocity and phase change, or if the RF voltage changes[1]. If the RF volt-

---

[1] This stands as long as the changes are slow in comparison to a synchrotron oscillation period.

age, V, or the energy are increased, the energy spread $(\Delta E)_{max} \propto (\beta_s^2\gamma_s^3)^{\frac{1}{4}}$ increases, but the time spread $(\Delta t)_{max} \propto (\beta_s^2\gamma_s^3)^{-\frac{1}{4}}$ decreases. This phenomenon is called adiabatic bunch compression in longitudinal phase-space. It should be noted that in the case in which the particle reaches the non-linear part of the RF wave, it will still oscillate about the stable phase, as long as it does not receive less voltage than the synchronous particle. The shape of its orbit in this case is not elliptical but somehow a fish-shape (still the trajectory is closed and stable). If a particle receives less voltage than the reference particle and is at a larger phase than ϕ_s, then that particle's motion will be unstable. Fig. 3.3 shows the separatrix, the very well defined boundary between stable and unstable motion.

The area in phase-space within the separatrix is called a bucket (shown in pink in fig. 3.3), and the collection of particles sharing a specific bucket is called a bunch. Note that not all buckets need to be populated. If the synchronous phase is 0 or π, then the ideal particle is not accelerated, in which case the buckets are called stationary buckets.

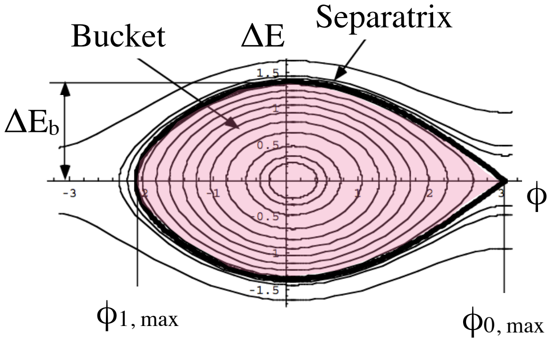

Figure 3.3.: The separatrix, is the boundary between stable and unstable motion. The area in the separatrix, shown in pink, is called bucket, and $\phi_{1,max}, \phi_{2,max}$ correspond to the maximum extent of bounded motion possible. Figure taken and edited from [66].

3.2. Need for Transverse Focusing

The need for beam focusing was recognised by Wideroe [67] when he constructed and tested the first (and unsuccessful) beam transformer. The first theories on beam stability and focusing were pursued by Walton [68] and later by Steenbeck [69]. Kerst and Serber [70] solved the focusing problems in a betatron accelerator in a detailed orbit analysis [64].

As seen in section 3.1, an RF field can be used to accelerate charged particles in such a way that stable oscillations about the design energy will be maintained. In this section it will be shown that if these fields were the only ones acting on the particles, motion in at least one direction transverse to the direction of motion would be unstable [59]. For example, figure 3.4 (top) shows the RF voltage as a function of time. Here, the reference particle arrives at z_s when the voltage is at a value $V \sin \phi_s$. The electric field of the same wave, as a function of z instead of t, is shown in figure 3.4 (bottom). When transforming to the rest frame of the synchronous particle, the longitudinal component of the electric field, E_z, appears to be unchanged. In this frame, E_z will have a negative gradient[2]: $\partial E_z / \partial z < 0$. Since there is no magnetic field in this region[3] then $\nabla \cdot \vec{E} = 0$, which implies the existence of another electric field component with a positive gradient. In the cartesian coordinate system (from $\nabla \cdot \vec{E} = 0$):

$$\frac{\partial E_x}{\partial x} + \frac{\partial E_y}{\partial y} + \frac{\partial E_z}{\partial z} = 0, \tag{3.2.1}$$

and so:

$$\frac{\partial E_x}{\partial x} + \frac{\partial E_y}{\partial y} > 0. \tag{3.2.2}$$

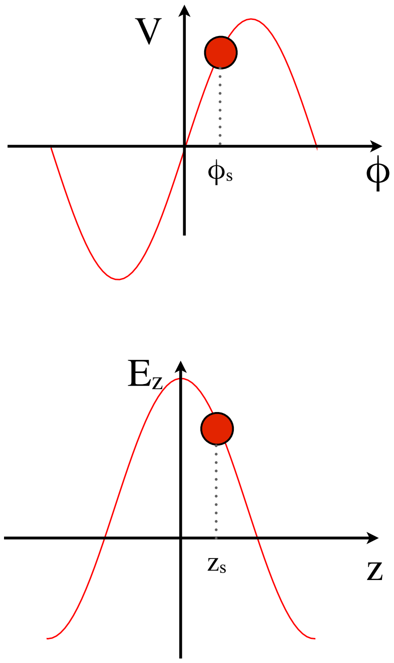

Figure 3.4.: (top) RF voltage as a function of time as seen at a specific longitudinal location, z; (bottom) longitudinal electric field as a function of longitudinal location, z, as seen at a particular time t.

From equation 3.2.2 it is deduced that the particles will be experiencing out-

---

[2] $\vec{E} = -\nabla V$.

[3] Fields due to the particles themselves are being neglected.

ward transverse forces that increase with x and y, which results in an unstable transverse motion. Therefore, accelerators could not operate without transverse focusing; transverse focusing is *essential* to ensure transverse stability.

3.3. Transverse Optics

In particle beam dynamics, the equation of motion in periodic lattices is similar to those studied by the astronomer Hill in the last century. In this subsection, the equation of motion, called Hill's equation, is discussed, together with its solutions and properties [64].

In periodic systems, given the amplitude of a particle's betatron motion[4] is small, the linearised betatron equation of motion is:

$$u'' + K(s)u = 0, \tag{3.3.1}$$

where u can be either x or y, and prime denotes derivative in s. $K(s)$ is an arbitrary periodic function of s with period L:

$$K(s) = K(s + L), \tag{3.3.2}$$

resembling the particular distribution of focusing along a beam line. For a general solution an ansatz with an s-dependent amplitude and phase is applied:

$$u(s) = \sqrt{\epsilon}\sqrt{\beta(s)}\cos[\psi(s) - \psi_o], \tag{3.3.3}$$

where ϵ and ψ_o are integration constants. Note how this ansatz is similar to the solution of a harmonic oscillator equation with a constant coefficient K. From [64] and appendix A.3 it is seen that the above ansatz is a real solution of the equation of motion 3.3.1, and that from the derivative of this solution a constant of motion is obtained, called the $Courant - Snyder\ invariant$:

$$\gamma u^2 + 2\alpha u u' + \beta u'^2 = \epsilon. \tag{3.3.4}$$

---

[4] Same as betatron oscillations, it is the particle motion around a closed orbit, as defined later in this section, see [71].

The phase $\psi(s)$ is called the *phase advance* and is defined as:

$$\psi(s) = \int_o^s \frac{d\bar{s}}{\beta(\bar{s})} + \psi_o, \tag{3.3.5}$$

and the parameters α, β and γ are found to satisfy:

$$\beta' = -2\alpha \tag{3.3.6}$$

and:

$$\gamma = \frac{(1+\alpha^2)}{\beta}. \tag{3.3.7}$$

Using statistical mechanics methods, the evolution of a large number of particles forming a particle beam could be described, since it is impractical to calculate trajectories along a beam line for each individual particle. Liouville's theorem states that under the influence of conservative forces the density of the particles in the six-dimensional phase-space, (x, y, z, p_x, p_y, p_z), stays constant (for a detailed proof see [64]). The strict version states:

"In the vicinity of a particle, the particle density in phase-space is constant if the particles move in an external magnetic field or in a general field in which the forces do not depend upon velocity".

This statement implies conservation of the phase-space area but is not applicable to situations where space-charge forces[5] within the beam play a role, or when particles emit synchrotron light, which is a velocity-dependent effect [65].

The invariance of ϵ in 3.3.4 is an alternative statement of Liouville's theorem. The physical interpretation of ϵ is that of a single particle trajectory in phase-space along the contour of an ellipse with the parameters α, β, and γ, and with the area $\pi\epsilon$. Since α, β, and γ are a function of s, the form of the ellipse (shape and orientation) changes constantly; however, due to Liouville's theorem, any particle starting on that ellipse will stay on it. α, β, and γ are the lattice functions, known as Twiss parameters, and the oscillatory motion of a particle along the beamline (eq. 3.3.3), is called the betatron oscillation. A single particle can be selected to define a phase ellipse, as it is now known that all particles with lesser betatron oscillation amplitudes will stay within that ellipse.

Liouville's theorem is a powerful tool as it allows the determination of the location and the distribution of the beam at any place along the transport line. This determination is done simply by knowing the area occupied by the beam

---

[5] The space-charge forces are caused by the electromagnetic fields created from the bunch, when there is high intensity. These fields can influence the bunch movement.

at the beginning of the beam transport line without the need of individual particle trajectory evaluation.

The transverse phase-space is formed with the variables x, x', y, y', where in paraxial approximation (small-angle approximation):

$$x' = \frac{p_x}{p_z}, \tag{3.3.8}$$

and

$$y' = \frac{p_y}{p_z}. \tag{3.3.9}$$

In the two-dimensional space of the transverse phase-space, the beam phase ellipse, the ellipse that surrounds all particles of a beam in phase-space (see fig. 3.5), is described by the equation:

$$\gamma x^2 + 2\alpha x x' + \beta x'^2 = \epsilon, \tag{3.3.10}$$

with α, β, γ and ϵ representing the ellipse parameters. The area of the ellipse in phase-space occupied by particles in a beam is equal to the beam emittance multiplied by π:

$$\int_{ellipse} dx dx' = \pi\epsilon \tag{3.3.11}$$

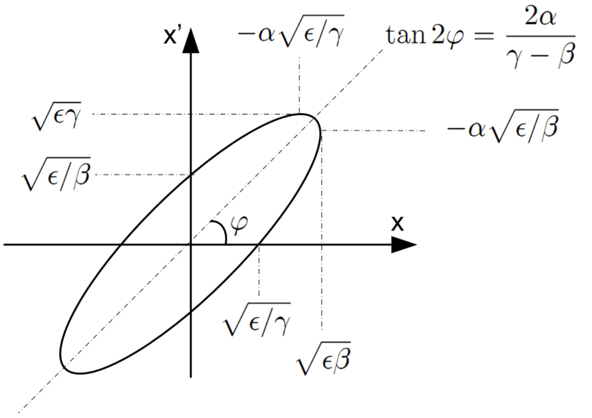

Figure 3.5.: Two-dimensional transverse phase-space ellipse from equation 3.3.10. Here x' is plotted against x, where $x' = \frac{p_x}{p_z}$ in paraxial approximation.

Often in literature, the RMS emittance is given rather than emittance. The RMS emittance of the beam is defined as the area divided by π of the ellipse containing 39% of the particles[6] [66].

Because of Liouville's theorem it is only necessary to know how the beam ellipse parameters change along the beam line in order to describe the whole particle beam. At the starting point $z = 0$ the phase ellipse equation is:

$$\gamma_o x_o^2 + 2\alpha_o x_o x_o' + \beta_o x_o'^2 = \epsilon. \tag{3.3.12}$$

Any trajectory of a particle can be transformed from $z = 0$ to any other point $z \neq 0$ with:

$$\begin{pmatrix} x \\ x' \end{pmatrix} = \mathbf{M} \begin{pmatrix} x_o \\ x_o' \end{pmatrix} = \begin{pmatrix} C(z) & S(z) \\ C'(z) & S'(z) \end{pmatrix} \begin{pmatrix} x_o \\ x_o' \end{pmatrix}, \tag{3.3.13}$$

where $C(z)$=$\cos(\sqrt{K}z)$ and $S(z)$=$\frac{1}{\sqrt{K}}\sin(\sqrt{K}z)$, with K representing the magnet's strength. Note that although only the (x, x') phase-space is shown here, the results are valid for the (y, y') phase-space as well. The new ellipse will have a different orientation and shape due to the different parameters (now α, β and γ) but the same area. The ellipse parameters transform like [64]:

$$\begin{pmatrix} \beta \\ \alpha \\ \gamma \end{pmatrix} = \begin{pmatrix} C^2 & -2SC & S^2 \\ -CC' & (S'C + SC') & -SS' \\ C'^2 & -2S'C' & S'^2 \end{pmatrix} \begin{pmatrix} \beta_o \\ \alpha_o \\ \gamma_o \end{pmatrix}. \tag{3.3.14}$$

The beam parameters can be calculated anywhere along the beam line using this equation, if the initial Twiss parameters are known, and from ellipse geometry we have [64]:

$$\beta\gamma - \alpha^2 = 1. \tag{3.3.15}$$

The transformation rules for these ellipses through a transport system have been derived for a two-dimensional phase-space. For an n-dimensional ellipse, the equation can be written as:

$$\mathbf{u^T}\sigma^{\mathbf{-1}}\mathbf{u} = \mathbf{1}, \tag{3.3.16}$$

where σ is still to be determined and $\mathbf{u^T}$ is the transpose of the coordinate vector $\mathbf{u}$. The beam matrix from point P_o to P_1 transforms with the help of

---

[6] In addition, often emittance is defined to be the area of the ellipse rather than the area over π; in this case "emittance" is written in the form $\epsilon\pi$, e.g. emittance of 10 π $mm \cdot mrad$ would correspond to $\epsilon = 10$ $mm \cdot mrad$ [66].

M like [64]:

$$\sigma_1 = \mathbf{M}\sigma_o\mathbf{M}^T. \tag{3.3.17}$$

In the two-dimensional space $u_{2D} = (x, x')$, and equation 3.3.16 then gives (with $\sigma_{12} = \sigma_{21}$):

$$\sigma_{22}x^2 + 2\sigma_{12}xx' + \sigma_{11}x'^2 = \epsilon^2, \tag{3.3.18}$$

which compared with equation 3.3.12 defines the beam matrix (covariance matrix) [64, 72]:

$$\sigma = \left(\begin{array}{cc} \sigma_{11} & \sigma_{12} \\ \sigma_{21} & \sigma_{22} \end{array} \right) = \epsilon \left(\begin{array}{cc} \beta & -\alpha \\ -\alpha & \gamma \end{array} \right) = \left(\begin{array}{cc} \langle x^2 \rangle & \langle xx' \rangle \\ \langle xx' \rangle & \langle x'^2 \rangle \end{array} \right). \tag{3.3.19}$$

The two-dimensional "volume" or phase-space area is:

$$V_{2D} = \pi\sqrt{|\sigma|} = \pi\sqrt{\sigma_{11}\sigma_{22} - \sigma_{12}^2} = \pi\epsilon_{2D}, \tag{3.3.20}$$

which agrees with the earlier emittance definition since $\beta\gamma - \alpha^2 = 1$.

A linear variation of beam emittances with energy is introduced when particles are accelerated or decelerated, called adiabatic damping. Under adiabatic damping, the beam emittance varies like:

$$\epsilon = \frac{p_o}{p}\epsilon_o, \tag{3.3.21}$$

where p_o, p are the initial and final momenta of the beam, before and after being accelerated. The quantity which remains conserved in the process of beam acceleration or deceleration is called normalised emittance, and is defined as:

$$\epsilon_N = \beta\gamma\epsilon = \frac{p\epsilon}{m_0 c}, \tag{3.3.22}$$

where m_0 is the rest mass; here $\gamma = E/m_0c^2$, where E is the particle's energy, and $\beta = u/c$, and they should not be confused with the Twiss parameters. ϵ_N stays constant even when the particle energy is changing due to external electric fields. However, ϵ_N does not stay constant in the presence of dissipating processes like synchrotron radiation, scattering or damping, as Liouville's theorem of phase-space conservation is not valid anymore [64, 73].

In four and six dimensions we have[7]:

$$u_{4D} = (x, p_x, y, p_y) \tag{3.3.23}$$

$$u_{6D} = (x, p_x, y, p_y, E, t), \tag{3.3.24}$$

and emittance can be then defined as[8]:

$$\epsilon_{2D,N} = \frac{1}{m_0 c}\sqrt{|V_{2D}|} \tag{3.3.25}$$

$$\epsilon_{4D,N} = \frac{1}{m_0 c}\sqrt[4]{|V_{4D}|} \tag{3.3.26}$$

$$\epsilon_{6D,N} = \frac{1}{m_0 c}\sqrt[6]{|V_{6D}|}, \tag{3.3.27}$$

where $|V_{nD}|$ is the determinant of the n-dimensional covariance matrix in phase-space. Note that the n-dimensional covariance matrix in phase-space relates to the one in trace space by $|V| = (m_0 c)^2 |\sigma|$.

3.4. Stability Criterion

In a long beam transport system, or a synchrotron, it is not obvious what relationships between lens strengths and spacing can lead to stable oscillations. In this subsection, the condition which establishes a stability criterion will be introduced.

An accelerator is usually constructed with repetitive modules. The transfer matrix $\mathbf{M}$ of one repetitive period composed of n elements is a periodic function of s with a period L, where L is the length of a module:

$$\mathbf{M}(s) = \mathbf{M}(s + L|s) = \mathbf{M}_n ... \mathbf{M}_2 \mathbf{M}_1, \tag{3.4.1}$$

and $\mathbf{M}_i$'s are the transfer matrices of the constituent elements (note that $s \equiv z$, and $L|s$ denotes the distance L from the point s). So, if $\mathbf{M}(s + L|s)$ is the transfer matrix for one periodic cell, then for N cells, $\mathbf{M}(s + N \cdot L|s) = [\mathbf{M}(s + L|s)]^N$. Stable solutions will be obtained as long as all the elements of the total transfer matrix stay finite as N increases indefinitely. $\mathbf{M}$ can be written

---

[7] Note that this description in phase-space substitutes the previous one in trace space by replacing p_x and p_y with x' and y'.

[8] For the derivation of equation 3.3.26 see section 3.7.

as:

$$\mathbf{M} = A\mathbf{I} + B\mathbf{J}, \tag{3.4.2}$$

where:

$$\mathbf{I} = \begin{pmatrix} 1 & 0 \\ 0 & 1 \end{pmatrix}, \mathbf{J} = \begin{pmatrix} \alpha(s) & \beta(s) \\ -\gamma(s) & -\alpha(s) \end{pmatrix}. \tag{3.4.3}$$

Here A and B are constants, and $\alpha(s), \beta(s)$, and $\gamma(s)$ are functions of s, and periodic in s with period L. One of the properties of $\mathbf{M}$ is that $|\mathbf{M}| = 1$ [74]. Therefore:

$$A^2 + B^2\left(-\alpha(s)^2 + \beta(s)\gamma(s)\right) = 1. \tag{3.4.4}$$

The s-dependent coefficient of B^2 must be constant, and since $\alpha(s), \beta(s)$, and $\gamma(s)$ are arbitrary functions of s, they can be chosen to be:

$$-\alpha(s)^2 + \beta(s)\gamma(s) = constant = 1, \tag{3.4.5}$$

which results in $A^2 + B^2 = 1$. Allowing $A = \cos\mu$ and $B = \sin\mu$, where μ could be imaginary, then:

$$\mathbf{M} = (\mathbf{I}\cos\mu + \mathbf{J}\sin\mu) = \begin{pmatrix} \cos\mu + \alpha(s)\sin\mu & \beta(s)\sin\mu \\ -\gamma(s)\sin\mu & \cos\mu - \alpha(s)\sin\mu \end{pmatrix}. \tag{3.4.6}$$

Note that $\mathbf{J}^2(s) = -\mathbf{I}$, and hence:

$$\mathbf{M}(s) = e^{\mathbf{J}(s)\mu}, \tag{3.4.7}$$

which implies $[\mathbf{M}(s)]^N = e^{\mathbf{J}(s)N\mu} = \mathbf{I}\cos N\mu + \mathbf{J}\sin N\mu$. Therefore μ needs to be real in order for the matrix elements to be finite as $N \to \infty$. Eq. 3.4.7 also implies that:

$$|Tr\mathbf{M}(s)| = |\mathbf{M}_{11} + \mathbf{M}_{22}| = |2\cos\mu| < 2, \tag{3.4.8}$$

or:

$$-2 \leq Tr\mathbf{M} \leq 2. \tag{3.4.9}$$

The result of eq. 3.4.9 is called the stability criterion for periodic beam transport lattices.

3.5. Equations of Motion in a Solenoid Magnet

Due to the symmetry between x and y axes, solenoids have larger acceptances and obtain stronger beam focusing than quadrupoles at low energies. Since stronger beam focusing increases the amount of achieved cooling, the transverse focusing in ionisation cooling channels is usually achieved using solenoids.

The equations of motion in a solenoid magnet, derived in appendix A.2 and [73] are:

$$\begin{aligned} x'' - S(z)y' - \frac{1}{2}S'(z)y = 0, \\ y'' - S(z)x' - \frac{1}{2}S'(z)x = 0, \end{aligned} \tag{3.5.1}$$

where $S(z) = \frac{e}{cp}B(z)$ is the magnet's strength[9], z is the beam-axis, and x, y are the horizontal and vertical coordinates of the transverse plane. There is an obvious coupling between the two planes, x and y. However, an applied rotation called the *Larmor frame*, R, will give two uncoupled equations, as demonstrated below. R can be defined as:

$$R = (x + iy)e^{-i\phi(z)}, \tag{3.5.2}$$

where ϕ is a rotation angle. From eq. 3.5.1 a single differential equation can be formed:

$$(x + iy)'' + iS(z)(x + iy)' + i\frac{1}{2}S'(z)(x + iy) = 0. \tag{3.5.3}$$

The rotation of eq. 3.5.2 can be applied to eq. 3.5.3, and by using:

$$(x + iy)' = R'e^{i\phi} + i\phi' Re^{i\phi} \tag{3.5.4}$$

and:

$$(x + iy)'' = R''e^{i\phi} + 2i\phi' R'e^{i\phi} + i\phi'' Re^{i\phi} - \phi'^2 Re^{i\phi} \tag{3.5.5}$$

then:

$$R'' - [S(z)\phi' + \phi'^2]R + i2[\phi' + \frac{1}{2}S(z)]R' + i[\phi'' + \frac{1}{2}S'(z)]R = 0. \tag{3.5.6}$$

---

[9] Note that a different notation is being used here for the magnet's strength. In previous subsections magnet's strength was instead noted with K. For instance, in the case of a quadrupole, $S = \frac{0.2998\ (dB/dx[T/m])}{p_0\ [GeV/c]}$.

By defining the rotation angle:

$$\phi(z) = -\frac{1}{2}\int_{z_o}^{z} S(\bar{z})d\bar{z}, \tag{3.5.7}$$

with z_o representing the start of the solenoid field, then $\phi' = -\frac{1}{2}S(z)$ and $\phi'' = -\frac{1}{2}S'(z)$. Eq. 3.5.6 then becomes a simple equation of motion:

$$R'' + \frac{1}{4}S^2(z)R = 0, \tag{3.5.8}$$

and with $R = u + iw$, the two uncoupled equations are finally created:

$$\begin{aligned} u'' + \frac{1}{4}S^2(z)u &= 0, \\ w'' + \frac{1}{4}S^2(z)w &= 0. \end{aligned} \tag{3.5.9}$$

At the entrance to the solenoid field the rotation angle is zero, and $u_o = x_o$ and $w_o = y_o$. In order to determine the particle's motion through the solenoid field, the particle coordinates (u, w) should be followed.

3.6. Transfer Matrix for Solenoid Magnet

Each coordinate depends on the initial values of all coordinates[10]. The transfer through a solenoid can be performed in two steps. The first is the solution of eq. 3.5.9 in matrix form, $\mathbf{M}_z$, and the second is a coordinate rotation applied with matrix $\mathbf{M}_r$ resulting in a total transformation of:

$$\begin{pmatrix} x \\ x' \\ y \\ y' \end{pmatrix} = \mathbf{M}_r\mathbf{M}_z \begin{pmatrix} x_o \\ x'_o \\ y_o \\ y'_o \end{pmatrix}. \tag{3.6.1}$$

---

[10] $x(z)$=$x(x_o, x'_o, y_o, y'_o)$ etc.

Analogous to [64], the transformation matrix $\mathbf{M}_z$ from the beginning of the solenoid field, z_o to a point z in the solenoid magnet becomes:

$$\mathbf{M}_z(z_o|z) = \begin{pmatrix} \cos\phi & \frac{2}{S}\sin\phi & 0 & 0 \\ -\frac{S}{2}\sin\phi & \cos\phi & 0 & 0 \\ 0 & 0 & \cos\phi & \frac{2}{S}\sin\phi \\ 0 & 0 & -\frac{S}{2}\sin\phi & \cos\phi \end{pmatrix}, \tag{3.6.2}$$

with $\phi = \frac{1}{2}Sz$, and the strength parameter $\frac{1}{4}S^2$ assumed to be constant along the magnet's length. As explained in [73], the rotation matrix at the point z within the solenoid field is given by:

$$\mathbf{M}_r = \begin{pmatrix} \cos\phi & 0 & \sin\phi & 0 \\ -\frac{S}{2}\sin\phi & \cos\phi & \frac{S}{2}\cos\phi & \sin\phi \\ -\sin\phi & 0 & \cos\phi & 0 \\ -\frac{S}{2}\cos\phi & -\sin\phi & -\frac{S}{2}\sin\phi & \cos\phi \end{pmatrix}. \tag{3.6.3}$$

For a solenoid magnet from $z_o = 0$ to z, where z is any point inside the solenoid, the transfer matrix, which is the product of 3.6.2 and 3.6.3 becomes:

$$\mathbf{M}_{sol}(0|z < L) = \begin{pmatrix} \cos^2\phi & \frac{1}{S}\sin 2\phi & \sin\phi\cos\phi & \frac{2}{S}\sin^2\phi \\ -S\sin\phi\cos\phi & \cos 2\phi & \frac{S}{2}\sin 2\phi & \sin 2\phi \\ -\sin\phi\cos\phi & -\frac{2}{S}\sin^2\phi & \cos^2\phi & \frac{1}{2}\sin 2\phi \\ -\frac{S}{2}\cos 2\phi & -\sin 2\phi & -S\sin\phi\cos\phi & \cos 2\phi \end{pmatrix}. \tag{3.6.4}$$

It should be noted that this transfer matrix is correct only for any z inside the solenoid. By setting $z = L_z$ the result would be inaccurate due to the discontinuity caused by the fringed field. Due to the solenoid fringe field, the rotation matrix exhibits a discontinuity. For $z = L_z + \epsilon$, where $\epsilon \to 0$ the phase is $\phi(L_z) = \Phi$ and the solenoid strength, S, is zero. Therefore the rotation matrix becomes:

$$\mathbf{M}_r = \begin{pmatrix} \cos\Phi & 0 & \sin\Phi & 0 \\ 0 & \cos\Phi & 0 & \sin\Phi \\ -\sin\Phi & 0 & \cos\Phi & 0 \\ 0 & -\sin\Phi & 0 & \cos\Phi \end{pmatrix}. \tag{3.6.5}$$

Multiplying eq. 3.6.2 with eq. 3.6.5, and with $\phi = \Phi$ the transformation matrix for a complete solenoid magnet becomes:

$$\mathbf{M}_{sol}(0|L) = \begin{pmatrix} \cos^2\Phi & \frac{1}{S}\sin 2\Phi & \sin\Phi\cos\Phi & \frac{2}{S}\sin^2\Phi \\ -\frac{S}{2}\sin\Phi\cos\Phi & \cos^2\Phi & -\frac{S}{2}\sin^2\Phi & \sin\Phi\cos\Phi \\ -\sin\Phi\cos\Phi & -\frac{2}{S}\sin^2\Phi & \cos^2\Phi & \frac{1}{2}\sin 2\Phi \\ \frac{S}{2}\sin^2\Phi & -\sin\Phi\cos\Phi & -\frac{S}{2}\sin\Phi\cos\Phi & \cos^2\Phi \end{pmatrix}. \tag{3.6.6}$$

It can also be shown that the focal length of a solenoid:

$$\frac{1}{f_{sol}} = \frac{1}{4}S^2 L_z = \frac{1}{4}\left(\frac{e}{cp}\right)^2 B_z^2 L_z, \tag{3.6.7}$$

is always positive and therefore a solenoid will always be focusing independently of the sign of the field or the sign of the particle charge.

3.7. Linearised Envelope Equations in a Solenoid

A four-dimensional beam distribution[11] with a cylindrical symmetry is in general a function of the angular momentum L_{can} and $(A_1^2 + A_2^2)$. In [75] it is shown that A_1 and A_2 are $\sqrt{\epsilon_x}$ and $\sqrt{\epsilon_y}$, and that the total amplitude[12] is:

$$A_\perp^2 \equiv \sqrt{1+\mathcal{L}^2}(A_1^2 + A_2^2) - 2\mathcal{L}\frac{L_{can}}{p_0}, \tag{3.7.1}$$

where $\mathcal{L}$ is the constant canonical angular momentum normalised to the beam emittance:

$$\mathcal{L} = \frac{m_0 c \epsilon_N}{L_{can}}, \tag{3.7.2}$$

and:

$$L_{can} = x p_y^c - y p_x^c. \tag{3.7.3}$$

Note that $\vec{p^c}$ denotes canonical conjugate momentum:

$$\vec{p^c} = \vec{p} + \frac{e}{c}\vec{A}, \tag{3.7.4}$$

where $\vec{p} = \gamma m_0 \vec{\beta} c$ (m_0 is the rest mass), and $\vec{A}$ is the vector potential.

---

[11] The distribution is 4-dimensional because of the coupling between x and $y-$coordinates.

[12] Amplitude is a conserved quantity and can be interpreted as follows: when the ellipse that corresponds to the RMS emittance is plotted around a beam distribution, amplitude is the area of the ellipse on which a random particle of that distribution sits on.

In [75] it is also shown that under the assumption of a cylindrically symmetric beam of a gaussian beam distribution given by:

$$F = \frac{Np_0^2}{4\pi^2 m_0^2 c^2 \epsilon_N^2} e^{-\frac{p_0 A_\perp^2}{2m_0 c\epsilon_N}}, \tag{3.7.5}$$

where N is the number of particles, then:

$$A_\perp^2 \approx \frac{x^2+y^2}{\beta_\perp} + \beta_\perp \left(x' - ky + \frac{\mathcal{L}}{\beta_\perp} y + \frac{\alpha_\perp}{\beta_\perp} x\right)^2 + \beta_\perp \left(y' + kx - \frac{\mathcal{L}}{\beta_\perp} x + \frac{\alpha_\perp}{\beta_\perp} y\right)^2, \tag{3.7.6}$$

where k is the linearised focusing term: $k(z) = qB(z)/2P_z$, and that the transverse covariance matrix can be written as[13]:

$$\mathbf{V}_\perp = m_0 c\epsilon_N \begin{pmatrix} \beta_\perp/p_0 & & & \\ -\alpha_\perp & \gamma_\perp p_0 & & \\ 0 & \beta_\perp k - \mathcal{L} & \beta_\perp/p_0 & \\ -(\beta_\perp k - \mathcal{L}) & 0 & -\alpha_\perp & \gamma_\perp p_0 \end{pmatrix}. \tag{3.7.7}$$

The 4D normalised emittance is then:

$$\epsilon_N = \frac{1}{m_0 c} \sqrt[4]{det \mathbf{V}_\perp} = \frac{1}{m_0 c} \sqrt[4]{\left[\langle x^2\rangle\langle p_x^2\rangle - \langle xp_x\rangle^2 - \langle xp_y\rangle^2\right]^2}. \tag{3.7.8}$$

The transverse betatron function, $\beta_\perp$, is related to $\alpha_\perp, \gamma_\perp$ and $\mathcal{L}$ by:

$$\gamma_\perp \equiv \frac{1 + \alpha_\perp^2 + (\beta_\perp k - \mathcal{L})^2}{\beta_\perp}, \tag{3.7.9}$$

and in general it can be calculated by:

$$\beta_\perp = \frac{(< x^2 > + < y^2 >)p}{m_0 c\epsilon_N}. \tag{3.7.10}$$

$\alpha_\perp$ is related to $\beta_\perp$ by:

$$-2\alpha_\perp = \beta'_\perp = \frac{d\beta_\perp}{dz}, \tag{3.7.11}$$

and [75]:

$$2\beta_\perp\beta''_\perp - (\beta'_\perp)^2 + 4\beta_\perp^2 B_0^2 - 4(1+\mathcal{L}^2) = 0. \tag{3.7.12}$$

---

[13] Terms above the diagonal are not included as the covariance matrix is symmetric.

This formalism is implemented in the G4MICE software and is extensively used for the results presented in this thesis in later chapters.

3.8. Ionisation Cooling Equations

In muon ionisation cooling, particles pass through absorbers where they lose energy in every direction (since the losses are parallel to the particle motion) through ionisation interactions, and then through RF cavities, where the lost energy is restored only in the longitudinal direction. The decrease of transverse momentum results in transverse emittance reduction, or "cooling" of the beam. Nevertheless, the random process of multiple scattering in the material medium increases the RMS beam divergence, and hence a heating term is added which needs to be controlled. Ionisation cooling will not work for protons as they interact strongly with the absorber, neither for electrons due to bremsstrahlung, but is practical for muons where cooling can occur within the muon lifetime [76].

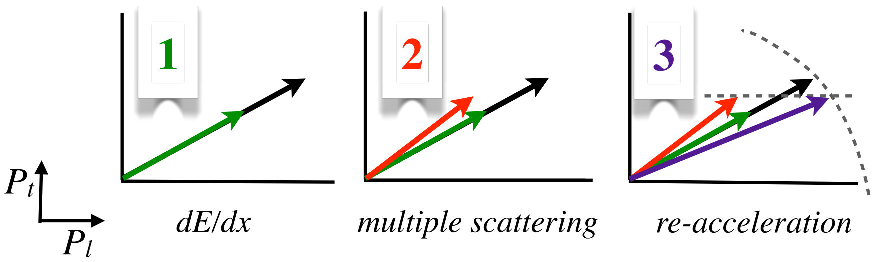

Figure 3.6.: Ionisation cooling schematic: first the particle's momentum reduces in direction opposite to that of motion, while passing through absorber (1). There is some random change in its transverse momentum due to multiple scattering (2). Finally, while the particle passes through the RF cavities, the transverse momentum stays the same and the energy lost in the absorbers is restored only longitudinally (3). P_t, P_l refer to the transverse and longitudinal momentum respectively.

3.8.1. Transverse Cooling

The RMS transverse cooling is given in the following differential equation[14] [76]:

$$\begin{aligned}\frac{d\epsilon_N}{ds} &= -\frac{1}{\beta^2 E}\frac{dE}{ds}\epsilon_N + \frac{\beta\gamma\beta_\perp}{2}\frac{d\langle\theta^2_{RMS}\rangle}{ds} \\ &= -\frac{1}{\beta^2 E}\frac{dE}{ds}\epsilon_N + \frac{\beta_\perp E_s^2}{2\beta^3 m_\mu c^2 L_R E},\end{aligned} \tag{3.8.1}$$

where the first term is the energy-loss effect (the cooling term) and the second is the multiple scattering heating term. In equation 3.8.1:

- ϵ_N is the normalised emittance (as described in sec. 3.3, the normalised emittance is related to the geometric emittance $\epsilon_\perp$ by $\epsilon_N = \epsilon_\perp\beta\gamma$. The beam size is given by $\sigma_x = \sqrt{\epsilon_\perp\beta_\perp}$)
- E the beam energy
- β and γ are the usual kinematic factors
- dE/ds is the energy loss rate ($s \equiv z$, as before both symbols denote the distance along the beam-axis)
- θ_{RMS} is the RMS multiple scattering angle and:

$$\frac{d\langle\theta^2_{RMS}\rangle}{ds} = \frac{E_s^2}{(p\beta c)^2 L_R} \tag{3.8.2}$$

- L_R is the material radiation length, defined as (for chemical elements):

$$L_R = \frac{716.4A}{Z(Z+1)ln(287/\sqrt{Z})}\mathrm{g}\cdot\mathrm{cm}^{-2} \text{ [77]}, \tag{3.8.3}$$

  where A and Z are the atomic weight and number of the absorbing material respectively

- $\beta_\perp$ is the betatron function
- E_s is the characteristic scattering energy, ~13.6 MeV [76].

From equation 3.8.1 it can be deduced that the more focused the beam is (the smaller the $\beta_\perp$), the less heating it undergoes, since the multiple scatter is

---

[14] $m_\mu \equiv m_0$.

smaller relative to the angular spread of the beam. The equilibrium emittance is defined as the ϵ_N for which the two terms of equation 3.8.1 are equal:

$$\epsilon_{N(equilibrium)} = \frac{\beta_\perp E_s^2}{2\beta m_0 c^2 L_R \frac{dE}{ds}}. \tag{3.8.4}$$

Since the cooling term is proportional to emittance, below $\epsilon_{N(equilibrium)}$, beam heating rather than cooling will occur.

3.8.2. Longitudinal Cooling

The longitudinal cooling with energy loss is described by the following equation [76]:

$$\frac{d\sigma_E^2}{ds} = -2\frac{\partial(dE/ds)}{\partial E}\sigma_E^2 + \frac{d\langle\Delta E_{RMS}^2\rangle}{ds}, \tag{3.8.5}$$

where the first term is the cooling term and the second is the heating term resulting from random fluctuations in the particle energy loss, called straggling (σ is the energy spread). Beam cooling can occur if the derivative $\frac{\partial(dE/ds)}{\partial E} > 0$, and the energy loss, $\frac{dE}{ds}$, can be estimated using the Bethe-Bloch equation:

$$\frac{dE}{ds} = 4\pi N_A r_e^2 m_e c^2 \rho \frac{Z}{A}\left[\frac{1}{\beta^2} ln\left(\frac{2m_e c^2\gamma^2\beta^2}{I}\right) - 1 - \frac{\delta}{2\beta^2}\right], \tag{3.8.6}$$

where:

- N_A is Avogadro's number
- ρ the density
- m_e and r_e are the mass and classical radius of the electron ($4\pi N_A r_e^2 m_e c^2 =$ 0.3071 MeV·cm^2/g)
- I is the ionisation constant and is approximately equal to $16Z^{0.9}$ eV
- δ is the density effect factor (small for low-energy muons)

The term $\frac{\partial(dE/ds)}{\partial E}$ is negative for $E_\mu <\sim 0.3$ GeV, and positive but small for higher energies.

In the Gaussian approximation, the second term of equation 3.8.5 can be expressed as:

$$\begin{aligned}\frac{d\langle\Delta E_{RMS}^2\rangle}{ds} &= 4\pi(r_e m_e c^2) n_e \gamma^2 (1 - \frac{\beta^2}{2}) \\ &\approx 0.157\rho\frac{Z}{A}\gamma^2\left(1 - \frac{\beta^2}{2}\right) (\text{MeV})^2\text{cm}^2/\text{g}, \qquad (3.8.7)\end{aligned}$$

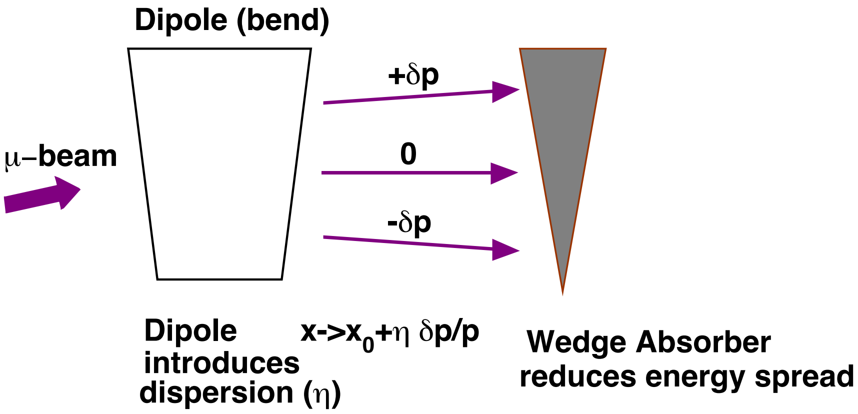

Figure 3.7.: Emittance exchange overview. Dipoles create dispersion, an energy-position correlation, and wedge absorbers create a correlation between energy loss and position. Since the more energetic particles follow a different path than the less energetic ones, they can also pass through more absorber material. Figure taken from [76].

where n_e is the electron density in the material ($n_e = N_A \rho Z/A$). Since this expression increases rapidly with higher energy, and therefore larger γ, it counteracts the cooling process; with the increase of this energy straggling effect, the longitudinal cooling provided by ionisation cooling is not adequate [76].

3.8.2.1. Emittance Exchange

Longitudinal cooling can be achieved in a process called "emittance exchange". By placing the absorbers at non-zero dispersion positions, i.e. where the transverse position depends upon energy, and where the absorber's thickness (and therefore energy loss) depends upon position (e.g. by using a wedge absorber), the high energy particles can pass through more absorber material. As a result, these particles will lose more energy and therefore the beam energy spread will decrease.

The longitudinal cooling derivative can be rewritten like:

$$\frac{\partial \frac{dE}{ds}}{\partial E} \rightarrow \left.\frac{\partial \frac{dE}{ds}}{\partial E}\right|_0 + \frac{dE}{ds}\frac{\eta \rho'}{\beta c p \rho_0}, \tag{3.8.8}$$

where ρ'/ρ_0 is the relative density change with respect to transverse position, ρ_0 is the reference density associated with dE/ds, and η is the dispersion, given by:

$$\eta = \frac{dx}{d(\Delta p/p)}. \tag{3.8.9}$$

In this way, the longitudinal cooling rate is increased by the same amount the transverse cooling decreases. Now the transverse cooling term is:

$$\frac{d\epsilon_N}{ds} = -\frac{1}{\beta^2 E}\frac{dE}{ds}\left(1 - \frac{\eta\rho'}{\rho_0}\right)\epsilon_N. \tag{3.8.10}$$

On the other hand the longitudinal emittance equation is given by:

$$\frac{d\epsilon_L}{ds} = -\frac{g_L}{\beta^2 E}\frac{dE}{ds}\epsilon_L + \frac{\beta_\phi}{2}\frac{d\langle\Delta E^2_{RMS}\rangle}{ds}, \tag{3.8.11}$$

where g_L is the partition number for longitudinal cooling (see appendix A.1), β_ϕ is a focusing function:

$$\beta^2_\phi = \frac{\langle\phi^2\rangle}{\langle\Delta E^2\rangle} = \frac{1}{\beta^3\gamma e V'\sin\phi_s}\frac{2\pi}{\lambda_0}\frac{\alpha_c}{mc^2}, \tag{3.8.12}$$

and V and α_c are the RF voltage ($V' = \frac{dV}{dz}$) and the momentum compaction factor respectively. The momentum compaction factor is defined as the variation of the path length with momentum:

$$\alpha_c = \frac{\Delta L/L_o}{\Delta p/p_o}, \tag{3.8.13}$$

where ΔL is the deviation of a particle's path from the ideal path L_o, and Δp is the momentum deviation from the reference momentum p_o. In [76] it is also shown that the optimal momentum for muon cooling, P_μ, is in the range of P_μ=200-400 MeV/c. Cooling is not optimal at low energies, and it becomes less efficient at high energies, where energy straggling increases.

3.8.3. 6D Cooling

As shown in section 3.8.2.1, the longitudinal cooling comes at the expense of the transverse phase-space increase, and therefore in order to achieve 6D cooling (transverse *and* longitudinal cooling), RF cavities as well as wedge absorbers and a dispersion mean should be used. 6D cooling could be useful for a Neutrino Factory but is essential for a Muon Collider. A description and analysis results of a novel 6D ionisation cooling channel are given in chapter 10.

Chapter 4

The Muon Ionization Cooling Experiment (MICE)

The muon beam, produced by pions decaying in flight, has a very large transverse emittance which needs to be reduced, in a process called “beam cooling”. Beam cooling is essential in order for the beam to fit inside the acceptance of downstream accelerator systems. Because of the muons short lifetime the only viable cooling technique is ionisation cooling (the theory behind the ionisation cooling technique is described in detail in section 3.8). However, although the physics of ionisation cooling is straightforward, this technique has never been experimentally demonstrated. The Muon Ionisation Cooling Experiment (MICE), will be the first experiment to demonstrate ionisation cooling. Based at the Rutherford Appleton Laboratory (RAL), MICE will design, engineer and fabricate a section of cooling channel. This channel will be placed in a muon beam and its performance will be measured in a variety of operating modes and beam conditions, validating finally the cooling simulations (this procedure is needed for the optimisation of the Neutrino Factory and Muon Collider cooling channels design) [78].

4.1. Experimental Layout

MICE is a single-particle experiment in which the position and momentum of each muon is measured before the muon enters the MICE channel, and again after it has left. The MICE channel includes liquid-hydrogen absorber and high-gradient RF cavities, all packed in a solenoidal magnetic channel.

MICE aims to observe the transverse emittance reduction of the muon beam by more than 10%, for muon momenta between 140 and 240 MeV/c. The measurement of the beam transmission and emittance reduction is performed with an absolute precision of ±0.1% by spectrometers placed before and after the cooling section.

MICE is based at a dedicated muon beam line at RAL (fig. 4.1). A titanium target is dipped into the ISIS[1] 800 MeV proton beam with a frequency of 0.3 Hz. The proton-titanium collisions produce pions which are focused by a quadrupole triplet (Q1-3) and momentum selected at 400 MeV/c by the first dipole, D1. Most of the pions decay to muons in a 5 m long, 5 T superconducting solenoid (DS). Further downstream a second dipole (D2) selects muons of 200 MeV/c ensuring muon purity of 99.9%. Two quadrupole triplets (Q4-6 and Q7-9) follow the second dipole, which transport the beam to the lead diffuser where a tuneable input emittance is generated (1-12 π mm·rad) for the cooling measurements.

Various detectors for beam characterisation and particle-identification (PID) (two time-of-flight (TOF) scintillator detectors (TOF0 and TOF1), together with threshold Cherenkov counters (CKOVA and CKOVB), a rate counter (GVA1), and beam-profile monitors (BPM1 and BPM2)) are located upstream of the cooling channel allowing a pure muon beam to be selected. A final TOF detector (TOF2) and KLOE-Light (KL) detector, placed downstream the cooling channel, allow muon decay identification. KL forms half of the downstream electromagnetic calorimeter (which will distinguish muons from decay electrons), and the other half is an electron-muon ranger (EMR), a fully active scintillator detector which is still under construction.

The two solenoidal spectrometers that are placed before and after the cooling channel, provide charged-particle tracking (trajectory reconstruction). Each spectrometer consists of a 4 T superconducting solenoid, instrumented with a tracker composed of five planar scintillating-fibre stations[2] (see fig. 4.2). Each station consists of three doublet-layers of scintillating fibres. The MICE trackers are read out using the DØ Central Fibre Tracker (CFT) optical readout and electronics systems. Visible Light Photon Counters (VLPCs) with a high quantum efficiency (~80%) and high gain are used to detect the scintillation light. The VLPC signals are digitised using the Analogue Front End with Timing (AFE IIt) board developed by the DØ collaboration. A high track-finding efficiency is expected to be provided from the trackers themselves, in the presence of background that is induced by X-rays (the X-rays are pro-

---

[1] ISIS is a spallation neutron source. The accelerator consists of an injector and a 163 m circumference ring [79]. "ISIS" is not an acronym; it refers to the ancient Egyptian goddess and the local name for the river Thames.

[2] Imperial College MICE team proposed the scintillating-fibre tracking that forms the baseline instrumentation for the MICE spectrometers.

duced in the RF cavities). For more information on the design, construction and performance of the MICE scintillating fibre trackers see [80].

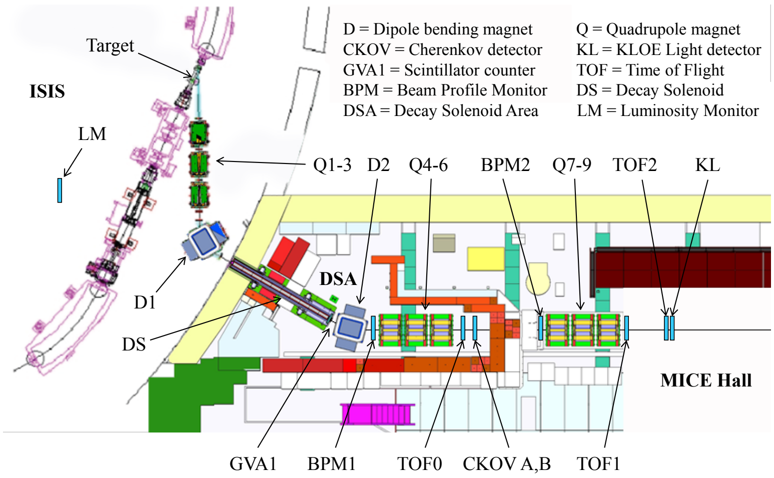

Figure 4.1.: The MICE beamline at ISIS, RAL. The target, the magnets transporting the beam, and the various detectors are shown. Figure courtesy of Dr. A. Dobbs [81].

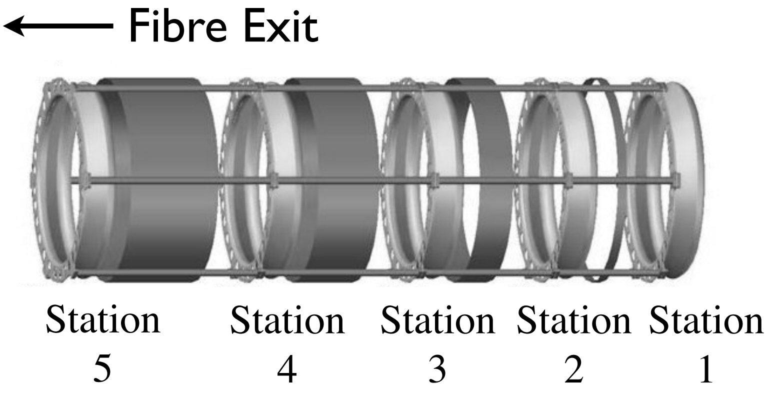

Figure 4.2.: MICE tracker schematic diagram. The five stations are shown, supported by the carbon-fibre space frame (fibres omitted for clarity). The beam direction is from left to right. Note this diagram represents the upstream tracker. The stations of the downstream tracker start with Station 1 on the left, and end with Station 5 on the right. Diagram taken and edited from [80].

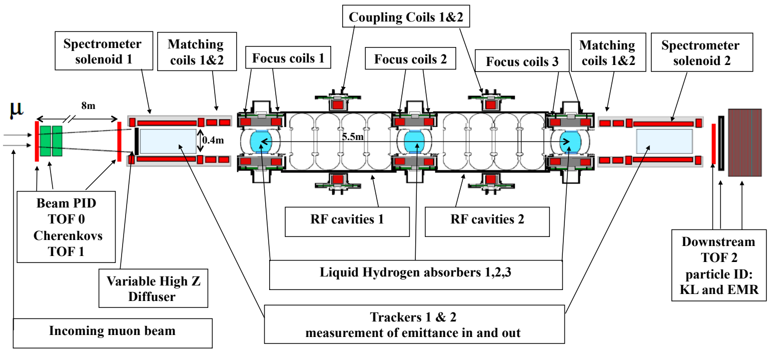

Figure 4.3.: The MICE cooling channel. Figure taken from [82].

The 5.5 m long MICE cooling channel is shown in fig. 4.3. The channel, located downstream of the first tracker, consists of three absorbers that alternate with two RF coupling coil modules (RFCC)[3]. The absorbers, made of liquid Hydrogen (LH_2), or solid Lithium Hydride (LiH), are inside an absorber-focus-coil module (AFC) with superconducting coils, which provide strong focusing at the absorbers. Each RFCC module contains four normal-conducting RF cavities of 201 MHz that sit inside a focusing magnetic field. A MICE status update can be found at [83].

---

[3] The final absorber is used to protect the trackers against dark currents emitted by the RF cavities (more on the dark currents in section 5).

Chapter 5

RF Breakdown

The cooling lattices of both the Neutrino Factory and Muon Collider [84, 85] require high gradient RF and strong focusing solenoids. However, it has been experimentally demonstrated that serious problems can occur when operating RF cavities in the required magnetic fields.

5.1. The Kilpatrick Limit

In the 1950s, W. D. Kilpatrick analysed data on the RF breakdown, the process which limits the maximum achievable electric field in the cavity, and defined the conditions that could lead to a breakdown-free operation. The results of this analysis were expressed in a formula, by T. J. Boyd [63]:

$$f(\mathrm{MHz}) = 1.6\mathrm{E}_{\mathrm{K}}^{2}\mathrm{e}^{-8.5/\mathrm{E}_{\mathrm{K}}}, \tag{5.1.1}$$

where f is the frequency, and E_K is the Kilpatrick limit in MV/m. However, due to the fact that the Kilpatrick criterion is based on old experimental results, it is considered to be conservative. Nonetheless, expression 5.1.1 is used for choosing the field level design for accelerating cavities, except that the actual peak surface field, E_s, is expressed as $E_s = bE_K$, with b being the bravery factor [63].

Recent experiments have also shown that operating RF in the required magnetic fields reduces the RF performance and leads to RF breakdown. Fig. 5.1 shows the maximum achievable gradient decrease with the increase of the magnetic field for different wall materials[1].

---

[1] Rather than constructing the entire RF cavity with a new material, different material "buttons" are manufactured and placed at the position of the RF iris, i.e. where the

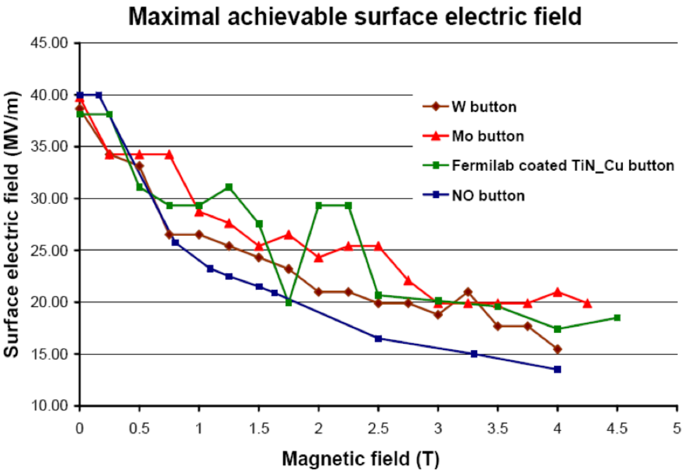

Figure 5.1.: Maximum achievable gradient as a function of the external magnetic field for different button materials. Figure taken from [86].

5.2. RF Breakdown Mechanism in the Absence of Magnetic Field

The breakdown models without magnetic fields are described in detail in [87]. In all models, the breakdown is initiated by asperities, where the local electric field is higher by a factor β_{FN}, introduced by Fowler-Nordheim [88]. Each asperity emits electron currents (dark current), and has a specific value of β_{FN}. The field emitted average electron current density J_F $(\frac{\mathrm{A}}{\mathrm{m}^2})$ for a surface field[2] $\mathbf{E}$ $(\frac{\mathrm{V}}{\mathrm{m}})$, and local field $\mathbf{E}_{local} = \beta_{FN}\mathbf{E}$ is given by:

$$J_F = \left(6 \times 10^{-12} \times 10^{4.52\phi^{-0.5}}\right) \frac{\mathbf{E}_{local}^{2.5}}{\phi^{1.75}} \exp\left[-\frac{\zeta\phi^{1.5}}{\mathbf{E}_{local}}\right], \tag{5.2.1}$$

where ϕ is the material work function in eV, and $\zeta = 6.53 \times 10^9\ (\mathrm{eV})^{-1.5} \left(\frac{\mathrm{V}}{\mathrm{m}}\right)$.

It is assumed that the breakdown occurs where the local field is maximum and therefore higher than the average value by a factor α. The average value is determined from the gradient dependence of the dark current from many asperities:

$$\frac{\mathbf{E}_{local}}{\alpha} = \langle\beta_{FN}\rangle\langle\mathbf{E}\rangle, \tag{5.2.2}$$

where $\alpha \geq 1$ depends on the probability distribution of β_{FN} [87].

---

beam will collide after being focused by the magnetic field.

[2] Note that, although in the other sections a vector V was represented with a letter and an arrow ($\vec{V}$), in this section a vector is represented with a bold letter ($\mathbf{V}$).

It is found that observed breakdown gradients depend on frequency ($\propto\sqrt{f}$), RF pulse length, and cavity dimensions. It is also found that over a range of frequencies, and for differing pulse lengths, cavity dimensions and waveguides, $\frac{\mathbf{E}_{local}}{\alpha}$ falls in a narrow range ~7 GV/m. Therefore, breakdown could be related to the local electric fields at asperities, or to the field emitted currents that strongly depend on these fields.

Possible mechanisms that initiate the RF breakdown, are [87]:

1. **Mechanical fracture model**: the local field at the top of a surface asperity is given by the average field multiplied by the Fowler-Nordheim field enhancement factor, β_{FN}. The outward electrostatic tension:

$$F_s = \frac{\epsilon_o}{2}(\beta_{FN}\mathbf{E})^2, \tag{5.2.3}$$

breaks off the tip, and the small piece moves away, being bombarded by field emitted electrons from the initial point. The piece vaporises and ionises, forming a local plasma which spreads, due to other mechanisms, leading to breakdown. So, in this model, the breakdown occurs when F_s is equal to the tensile strength of the material $\mathbf{T}$. Assuming the local field $\mathbf{E}_{local} = \alpha\langle\beta_{FN}\rangle\langle\mathbf{E}\rangle$, the average field at the surface of the asperity can be expressed as:

$$\langle\mathbf{E}\rangle \propto \frac{\sqrt{\mathbf{T}}}{\langle\beta_{FN}\rangle\alpha}. \tag{5.2.4}$$

2. **Ohmic heating model**: breakdown is initiated by ohmic heating, which results in melting down the tip of an asperity when the field emission current density is sufficiently high. Then the liquefied electrostatic forces pull the molten material away (like the broken piece of the asperity that was pulled away in the first model). While the molten material lifts from the remains of the asperity, it will be exposed to field emission from the initial point. This will result in further heating, vaporisation and ionisation of the molten material, that will finally form a plasma. In [87] it is shown that for a fixed emission area A_o and the asperity tip with the opening cone angle Ω (see fig. 5.2), the field needed to melt the material is proportional to $\mathbf{E}_{local} \propto (\frac{KT_m}{\rho})^{1/20}$, where $\mathbf{E}_{local}$ is the local electric field, K is the thermal conductivity, ρ is the electrical resistivity, and T_m is the melting temperature. It should be noted that a number of approximations is used for this expression: it is assumed the parameters have no temperature dependence, the shape of the asperity is assumed to be a cone of fixed angle, and the field emission is approximated by a power law. Nevertheless, the result should be able to qualitatively

reproduce the effect.

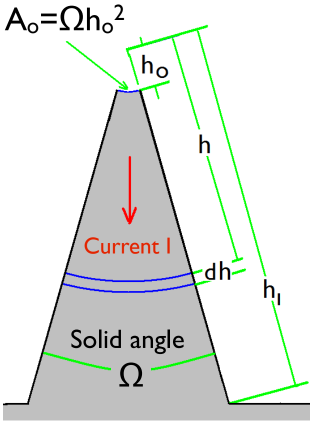

Figure 5.2.: Asperity heating calculation schematic. For this conical shape of the asperity, Ω is the solid angle, and $A_o = \Omega h_o^2$ is the emitting area of the asperity. Picture taken and edited from [87].

3. **Thermal runaway model**: resistivity and thermal conductivity are not independent of temperature, although in the ohmic heating model it was incorrectly assumed they are. In the thermal runaway model, an effective temperature is assumed to exist, called $T_{effective}$, in which the expressions given in the ohmic heating model are approximately valid. For small current densities, which result in temperatures smaller than a critical value ($T_{effective} < T_{critical}$) cooling increases faster than heating and a stable temperature is possible. However, for high current densities that lead to $T_{effective} > T_{critical}$, the rate of heating *vs* temperature increases faster than the cooling. In this case the temperature will rapidly increase which may result in breakdown.

4. **Reverse bombardment model**: this model assumes that some initial mechanism generates a local plasma, called "plasma spot". The plasma spot on its own does not directly cause breakdown. Breakdown occurs when the associated electrons emitted by the plasma are returned to their source spots by the RF electric field. The energy deposited in the source by these returning electrons increases the plasma size and causes the actual breakdown.

5. **Surface damage by heating model**: for up to 10 GHz, breakdown gradients rise approximately as the root of the RF frequencies. Above 10 GHz, the gradients are limited by the damage from cyclical surface heating, which is worse at points with maximum surface currents. Nonetheless, this phenomenon is only observed at very high frequencies

and therefore is not directly related to the cavities of Neutrino Factories or Muon Colliders, which have a frequency of 200-800 MHz.

It has been argued in the discussion above that the breakdown is initiated by ohmic heating. However this is based on a limited experimental evidence and it can therefore be deduced that the associated mechanism which initiates a breakdown is not understood completely. Nevertheless, there are some dependencies that appear typically, which arise due to changes in β_{FN}: over a range of frequencies (0.2-3 GHz), breakdown gradients are approximately proportional to $\sqrt{f}$, where f is the RF frequency. In addition there is a breakdown dependency on the required energy to melt a given volume of the electrode material. Finally, breakdown occurs at lower gradients for long RF pulses than for short pulses [87].

5.3. RF Breakdown Mechanism in the Presence of External Magnetic Field

The twist model, a published breakdown model with magnetic fields [89] suggests that the magnetic field dependence on breakdown originates from the torque forces on an asperity. These forces occur due to the inflow of current that feeds the field emission and in the presence of external magnetic field produces a force: $F \propto I \times B$, where $I \propto \mathbf{E}^{10}$ [89], and $\mathbf{E}$ is the cavity electric field gradient. So for a breakdown at a fixed force F it is expected that [87]:

$$\mathbf{E}_{breakdown} \propto B^{-\frac{1}{10}}. \tag{5.3.1}$$

In [87], a new model of breakdown in the presence of external magnetic field is proposed, which is independent of the breakdown mechanism in the absence of magnetic field. It should be noted that in this mechanism, breakdown occurs only if the breakdown gradient is lower than the gradient limit in the case without magnetic field.

In this model, dark current electrons, are accelerated by the RF fields and impact another location in the cavity. If there is no magnetic field then these impacts are spread over large areas and do not cause a problem. However, with sufficient magnetic field, these electrons are focused to small spots, melting the surface and creating a local damage. At a low gradient location this damage will not cause an immediate breakdown, but a hole can be made after the damage has been accumulated. In the case that the electrons are focused on a high surface RF gradient location, then electrostatic forces will pull the molten metal out and away from the surface. As the metal leaves the now damaged location, it will be exposed to field emitted electrons from the damaged area, and will be vaporised and ionised. This will lead to a local plasma and a subsequent breakdown. If the electrons have higher energies, then the melting will start deeper in the material, where the ionisation loss is larger. The melting will expand to the surface, at which point significant quantities of molten metal can be sprayed onto other surfaces in the cavity.

This model depends on a) β_{FN} that determines the strength of the field emitted current; b) the local geometry of the asperity; c) the geometry and magnetic fields that focus the electrons.

Fig. 5.3 shows how the trajectories of field emitted electrons are affected with an increase of the external field, B, from zero to 1 T. Note that the most sensitive place with respect to the RF breakdown is at the radius corresponding to the iris.

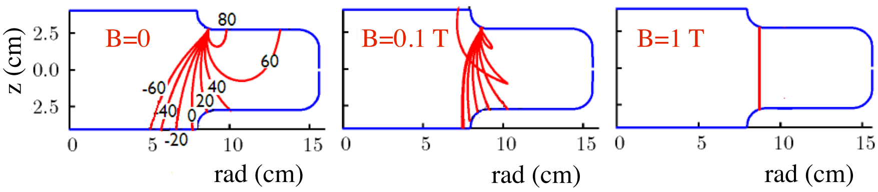

Figure 5.3.: 805 MHz pillbox cavity cross-section in no external magnetic field (left plot), axial field of 0.1 T (middle plot), and axial field of 1 T (right plot). Note that the vertical axis corresponds to the beam-axis, whereas the horizontal axis is the radius. The trajectories of electrons emitted at different phases are shown (phases are in degrees relative to the maximum) from the highest surface field location of the cavity. Figure taken and edited from [87].

5.4. Possible Solutions to the RF Breakdown

FSIIA (Feasibility Study IIA), is the current reference ionisation cooling channel of the Neutrino Factory. Despite the good transmission and cooling performance FSIIA presents, this lattice has a very large magnetic field at the RF position and therefore its feasibility has come under question. Finding a satisfactory solution is the important goal and the subject of this thesis.

Several possible solutions have been proposed in order to reduce the RF breakdown problems for a Muon Collider or Neutrino Factory. A brief description of each solution follows:

- **Redesign of the phase rotation and cooling channel:** the phase rotation and cooling channels could be redesigned so that they will use lower RF fields. This approach though would affect the performance.

- **Gas-filled RF cavities:** experiments have shown that RF breakdown can be suppressed in high magnetic fields when using hydrogen (H_2) gas-filled RF cavities. This technique can also provide superior cooling to Lithium Hydride (LiH) slabs since H_2 has less multiple scattering[3]. However, replacement of the LiH slabs would require a pressure of 120 atm of H_2 at room temperature, and this would be challenging to implement. Gallardo and Zisman [90] proposed to use sufficient pressure to suppress the breakdown (10-34 atm at room temperature) and introduce thinner LiH slabs in order to provide the added energy loss. This technique will provide adequate cooling with a minimal number of thickness of vacuum windows. It should be noted though, that studies [91, 92] have concluded that the electrons and ions produced by the ionisation of muons passing through gas filled RF cavities, have longer lifetimes compared to the muon beam. Such electrons in the cavity would be driven back and forth as the RF voltage oscillates, leading to heating the gas which would drain energy from the cavities. Moreover, the use of pressurised hydrogen raises serious safety issues.

- **Magnetically shielded RF cavities:** a cooling lattice has been developed [93] with much longer cell length and iron shielding of cavities, such that the magnetic field in the cavities is < 0.1 T. The increased cell length will result in weaker focusing and worse cooling performance, or decreased acceptance and worse transmission. Nonetheless, by using liquid H_2 absorbers, an adequate cooling could be obtained. With this method, the cooling channel requires little additional hardware development and can reproduce the nominal performance of the FSIIA channel, albeit with an increased hardware requirement and therefore additional cost. The lattice layout is illustrated in fig. 5.4.

---

[3] FSIIA uses LiH absorbers

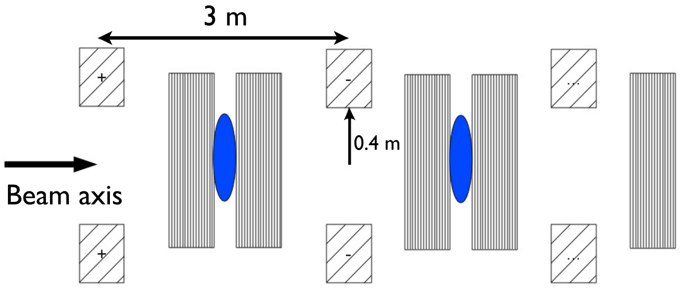

Figure 5.4.: Shielded RF lattice schematic. Diagonal and vertical hatching represent coils and RF cavities respectively. The filled ellipses represent hydrogen absorbers. Taken and edited from [94].

- **Magnetically insulated cavities:** Cavities could be designed in such a way that the electric gradient surfaces would be parallel to the magnetic fields, providing 'magnetic insulation'. In this case, dark current electrons would be constrained to move within short distances from the surfaces, gaining little energy, and would therefore cause no X-rays and damage. However, cavities designed in this way would possibly not give optimum acceleration for given surface fields. In addition, multipaction[4] could occur since the energies with which electrons return to the surfaces are in the few hundred volt range, i.e. where secondary emission is maximal. A layout of this cavity is shown in fig. 5.5.

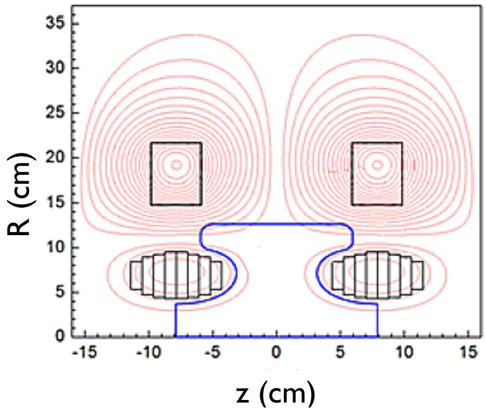

Figure 5.5.: Magnetically insulated cavity, modelled in Poisson Superfish. The red lines are the magnetic field lines, and the black lines are the coil configurations; the RF cavity is shown in blue. Picture taken and edited from [94].

---

[4] Multipaction is a combination of the phrase multiple impact. It is an electron multiplication phenomenon that can occur in the RF cavities when an electron from one surface hits the other surface, initiating the emission of one or more electrons. These electrons can hit again the surface, emitting more electrons (avalanche). For more information see [63].

- **Beryllium cavities:** In the case RF breakdown is found to be caused by surface heating, using a different cavity material could mitigate the problem. Using Beryllium could lead to less energy deposition per unit volume, as this material has low density. Additionally, this material has low thermal expansion which could result in less damage. However, Beryllium dust is toxic and therefore several handling and safety issues would need to be overcome [95].

- **Bucked Coils:** I proposed a novel idea, to use a "Bucked Coils" configuration, and designed the "Bucked Coils lattice". Instead of using a single coil (i.e. what is used for the FSIIA lattice), I used two coils with different radii and opposite polarities, placed at the same position (homocentric coils). The polarity of each pair of coils alternates with every repeat. The characteristics of this coil configuration lead to a significant magnetic field reduction at off-axis positions at desired locations (e.g. the walls of the RF cavity) without compromising the cooling efficiency of the lattice. More details on the Bucked Coils lattice are given in chapter 7.

Experiments are needed to study the RF breakdown problem, and the validity of its possible solutions. The Muon Test Area (MTA) at Fermilab, designed to develop and test muon ionisation cooling apparatuses, provides a needed boost to the efforts of those working on muon colliders for the entire Muon Collaboration. Several different configurations like 805 MHz RF cavities and High Pressure RF cavities are being studied at the MTA facility [96, 97].

Chapter 6

Lattices with increased cell length

Reducing the magnetic field at the RF position is crucial, as described in chapter 5. With this in mind, several lattice configurations were taken into consideration aiming to mitigate the magnetic field issue while at the same time achieving a transmission (number of muons at a specific position) comparable to the FSIIA lattice.

The magnetic field could be reduced at the position of the RF cavities by increasing the cell's length. Therefore two new cells, Doublet-1 and Doublet-2, were designed with a larger cell length than FSIIA.

A description of the MICE[1], FSIIA, Doublet-1 and -2 cells geometries follows together with a comparison of the magnetic field, transmission and cooling dynamics obtained by each lattice.

6.1. Description of Lattice Geometries

- **MICE**: A half-cell of the MICE-like lattice consists of a liquid Hydrogen absorber (LH_2) followed by a set of four 201.25 MHz RF cavities, called RF-quadruplet. Three solenoidal coils of the same polarity are placed between two consecutive absorbers: the Focus, the Coupling and another Focus coil[2]. The coils' polarity alternates with every half-cell repeat. A full-cell of the MICE-like lattice is illustrated in fig. 6.1a.

- **FSIIA**: A half-cell of the FSIIA lattice consists of a coil, followed by one 200 MHz RF cavity that has Lithium Hydride (LiH) absorbers on

---

[1] The MICE-like cell was used as a pedagogical approach, in order to learn how to use effectively the G4MICE software, as well as for comparative reasons.

[2] These names have been adopted in the MICE experiment but obviously all coils are used to focus the muon beam.

each side. The absorbers are coated with a 25 μm thick Beryllium (Be) window, which seals the cavity electromagnetically, acting in this way as ionisation cooling element. The coil's polarity alternates with every half-cell repeat and therefore the on-axis magnetic field at the centre of each RF cavity is zero. Fig. 6.1b shows a full-cell of the FSIIA lattice.

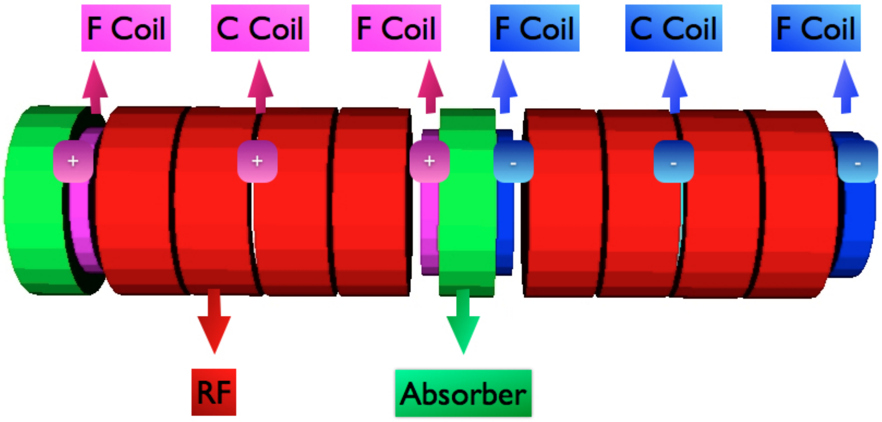

(a) MICE full-cell layout (5.5 m). F and C stand for Focus and Coupling coils respectively.

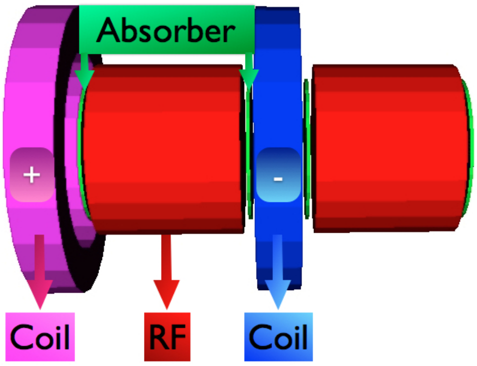

(b) FSIIA full-cell layout (1.5 m). The absorbers are coated with a thin layer of Beryllium windows that seal the cavity electromagnetically.

Figure 6.1.: Full-cell layouts of the MICE and FSIIA lattices. The beam direction is from the left to the right.

- **Doublet-1**: A full-cell of the Doublet-1 lattice, shown in fig. 6.2a, consists of one LiH absorber, five 200 MHz RF cavities and two coils of opposite polarity. The first RF cavity is adjacent to the absorber. The coils follow, with three more RF cavities in between them called RF-triplet.

The fifth RF cavity comes after the second coil. The two RF cavities that are placed on each side of the LiH absorber form an RF-doublet.

- **Doublet-2**: A half-cell of Doublet-2 has the same components and length as a Doublet-1 full-cell. However, the coils in a Doublet-2 half-cell have the same polarity, which alternates with every Doublet-2 half-cell repeat (see fig. 6.2b). This results in a slightly different magnetic field behaviour and subsequently in a different beam focusing. Similarly with the Doublet-1 cell case, the three RF cavities that are between two coils of the same polarity form an RF-triplet, whereas the two RF cavities that are placed on each side of the LiH absorber form an RF-doublet.

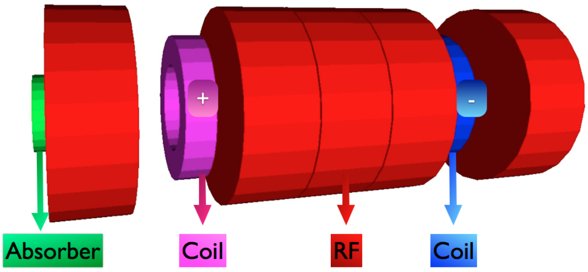

(a) Doublet-1 full-cell layout (3.85 m).

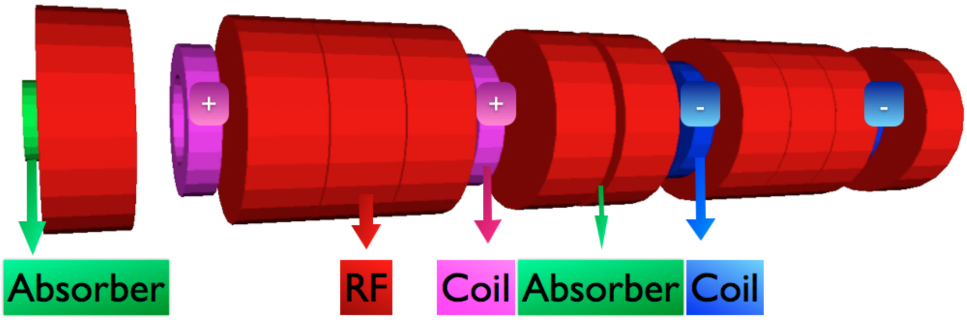

(b) Doublet-2 (7.70 m).

Figure 6.2.: Doublet-1 and -2 full-cell layouts.

The main characteristics of all lattices are presented in table 6.1.

Table 6.1.: Main characteristics of the lattices. Note that D-1 and D-2 correspond to “Doublet-1” and “Doublet-2” respectively, and F and C in the “Coils” section (under the MICE column) correspond to “Focus coil” and “Coupling coil”.

Lattice	**MICE**	**FSIIA**	**D-1**	**D-2**
Full-cell length [m]	5.5	1.5	3.85	7.70
Number of RF cavities	8	2	5	10
Number of Absorbers	2	4	1	2
Number of Coils	6	2	2	4
RF cavities				
Peak Electric Field [MV/m]	12.460	15.0	16.5	16.5
Phase [degrees]	40	40	50	50
Length [m]	0.46	0.50	0.50	0.50
Radius [m]	0.64	0.30	0.70	0.70
Absorbers				
Length [m]	0.3683	0.0115	0.0860	0.0860
Radius [m]	0.64	0.25	0.25	0.25
Coils				
Current Density [A/mm^2]	F: 113.950; C: 96.210	106.667	44.260	44.260
Inner Radius [m]	F: 0.263; C: 0.725	0.350	0.300	0.300
Thickness [m]	F: 0.840; C: 0.116	0.150	0.200	0.200
Length [m]	F: 0.210; C: 0.250	0.150	0.200	0.200

6.2. Methodology

Apart from the magnetic field reduction, the new lattices also aim to achieve a comparable transmission and emittance reduction to FSIIA. I order to check the transmission and cooling efficiency, a beam was created for each lattice using the Optics application of G4MICE [98]. This application creates a beam with a transverse beta ($\beta_\perp$) and transverse alpha ($\alpha_\perp$) matched to the lattice. The beam in every lattice was input at zero magnetic field. Ten extra coils were placed at the beginning and at the end of each lattice to ensure a symmetric magnetic field configuration after the field superposition.

The beam consists of 1,000 muons with 10 π mm·rad transverse RMS emittance and 0.07 ns RMS longitudinal emittance. The beam follows a gaussian distribution in momentum, centred at 232 MeV/c (σ_{RMS}: 18.33 MeV/c) for all lattices apart from the beam input at the MICE-like lattice, which is centred at 200 MeV/c (σ_{RMS}: 17.02 MeV/c). The choice of 200 MeV/c is based on the presence of resonances in this lattice at approximately 250 MeV/c (see fig. 6.9). The G4MICE software was set to only track muons and to allow muon decays; the absorber's thickness was chosen such as to keep the energy of the reference particle constant.

6.3. Results

6.3.1. Magnetic Field Comparison

Fig. 6.3a presents the longitudinal component of the magnetic field, B_z, of the Doublet-1 and -2 cells (in black and red respectively) along the beam-axis, z. The two new lattices have a similar magnetic field behaviour and in order to understand where exactly B_z differs between these two lattices, fig. 6.3b is plotted presenting the absolute value of B_z along z. As seen in this plot, the Doublet-2 cell achieves only 0.075 T smaller magnetic field than the Doublet-1 cell at the centre of the second RF cavity of the RF-triplet.

The magnetic field of each lattice is measured at the cavity's wall, since this is the most sensitive location with respect to the RF breakdown effect. In the case of Doublet-1 and -2 this position is at the start of the first RF cavity of the RF-triplet (or the end of the third RF cavity of the RF-triplet)[3].

Similarly in the MICE cell this position is at the end of the first (or last) RF cavity of each RF-quadruplet. Fig. 6.4 justifies this choice since, as indicated with the dashed red line in the figure, the first and fourth RF cavities experience higher magnetic field than the cavities in the centre.

---

[3] Since these two positions are symmetric with respect to the magnetic field it does not matter which one is chosen for the measurement. The first and third RF cavities of the RF-triplet are closer to a coil, experiencing in this way a larger sensitivity to the RF breakdown effect. Therefore the position of the RF-triplet was selected for the magnetic field calculation.

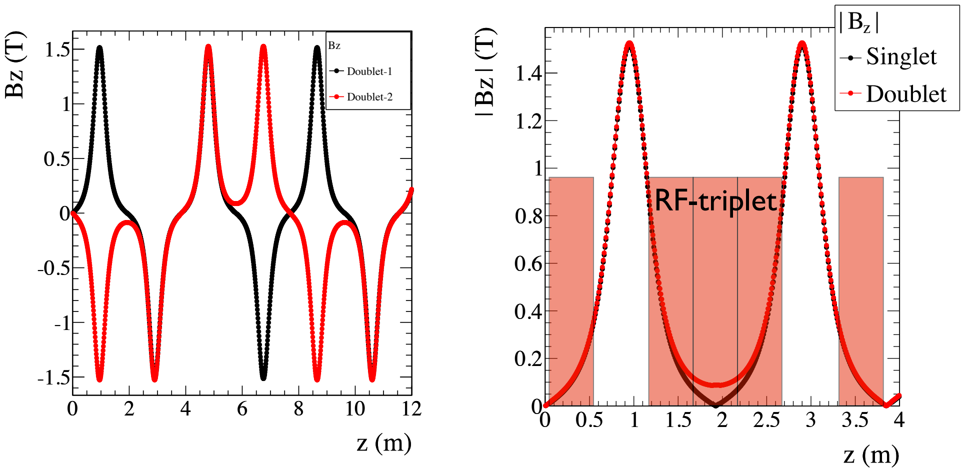

(a) B$_z$ along the beam-axis.

(b) Absolute value of B$_z$ along the beam-axis. The RF cavities are shown in pink, and the RF triplet is indicated.

Figure 6.3.: Longitudinal component of the magnetic field of Doublet-1 (black) and -2 (red) along the beam-axis, z. As shown in (b), the field of these lattices is very similar: Doublet-2 achieves only 0.075 T smaller B_z at the centre of the second RF cavity of the RF-triplet, which is at 1.925 m.

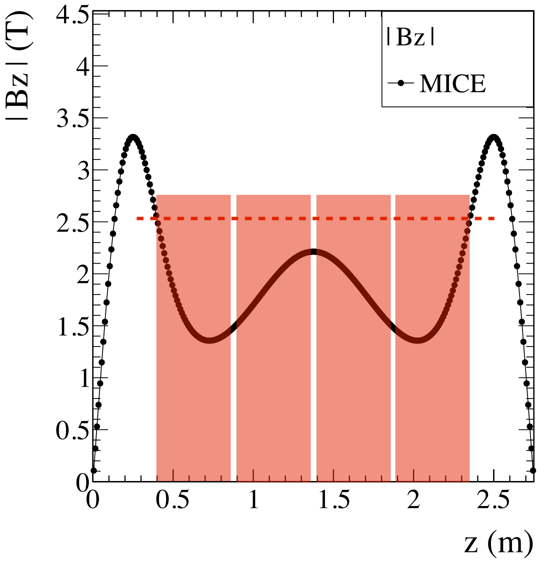

Figure 6.4.: Absolute B_z of MICE half-cell (2.75 m). The RF cavities are shown in pink, and the dashed red line indicates the magnetic field value at the RF cavities. Since the first and last RF cavities experience higher magnetic fields, the positions of these cavities have been chosen for the calculation of the total magnetic field.

Fig. 6.5 presents the total magnetic field, B_{tot}, as a function of the radius, R, at the z-position corresponding to the edge of the RF cavities for each lattice. The MICE-like cell is shown in black, FSIIA in red and Doublet-1 and -2 in green and blue respectively. The same colour code will apply for all the results presented in section 6.3. The magnetic field decrease achieved by the new lattices, Doublet-1 and -2, can be easily seen: the B_{tot} of the Doublet-1 and -2 cells is more than eight times smaller than that of the FSIIA lattice at 0.4 m radius, where FSIIA has its maximum B_{tot}. For R=0.5 m, Doublet-1 and -2 achieve almost the same magnetic field with the MICE-like cell whereas at 0 m radius Doublet-1 and -2 achieve a 2.7 and 2.35 times smaller magnetic field than the FSIIA and MICE-like lattices respectively.

The longitudinal component of the magnetic field, B_z, which is believed to have the greatest impact on the RF breakdown effect, is shown in fig. 6.6a. At 30 cm, where FSIIA has its maximum, both Doublets achieve approximately eight times smaller value than FSIIA.What is important to note, is that at ∼20 cm, i.e. at the position of the RF iris[4], the Doublet cells achieve four and 2.37 times smaller B_z than the FSIIA and the MICE-like cooling lattices respectively. Fig. 6.7 shows the RF quadruplet layout of MICE [78].

Fig. 6.6b presents the transverse component of the magnetic field, B_r, with respect to the radius at the end of the RF cavity. The MICE-like cooling cell has a similar behaviour as the Doublet cells, and at 40 cm radius all lattices achieve approximately eight times smaller magnetic field than the FSIIA cell.

---

[4] As mentioned in sec. 5, the RF iris is the most sensitive position with respect to the RF breakdown effect. It is therefore desired for any cooling lattice to achieve a very small magnetic field at this position.

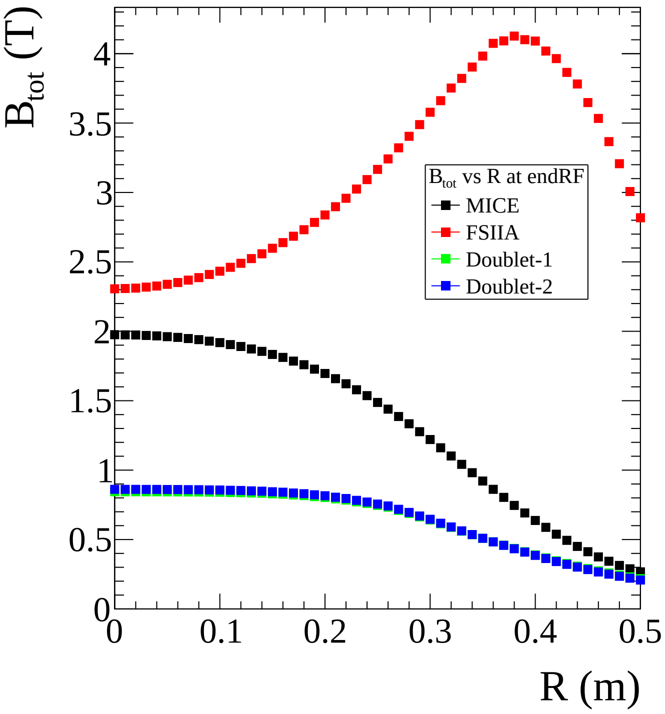

Figure 6.5.: Total magnetic field at the wall of the RF cavity with respect to the radius, R, for MICE (black), FSIIA (red), Doublet-1 (green) and Doublet-2 (blue). The magnetic field achieved in the Doublet cells is notably lower than that of MICE cell for small radii, and significantly lower than that of FSIIA for large radii (especially at ∼40 cm).

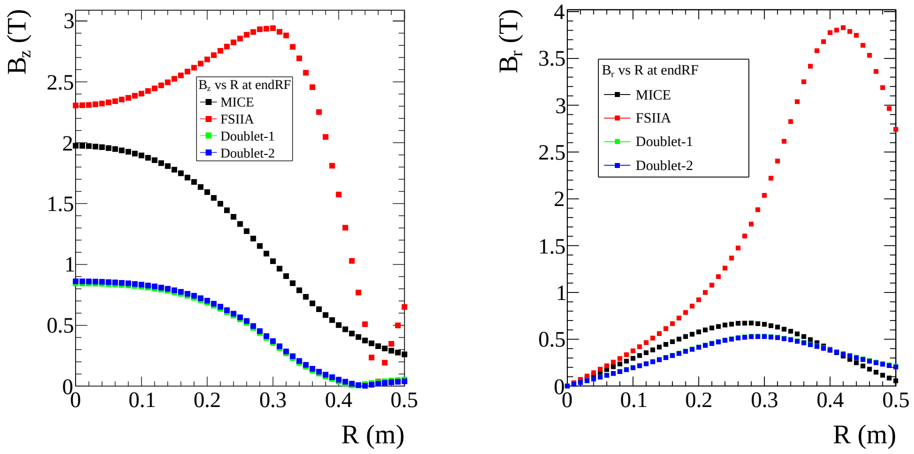

(a) B$_z$ with respect to z.

(b) B$_r$ with respect to z.

Figure 6.6.: Comparison of the longitudinal (B_z) and transverse (B_r) components of the magnetic field as a function of R. B_z is believed to have the greatest impact on the RF breakdown effect. Note that at the point where FSIIA has its maximum B_z, the Doublet cells achieve as high as eight times smaller magnetic field. At R=40 cm, all lattices achieve approximately eight times smaller B_r than FSIIA.

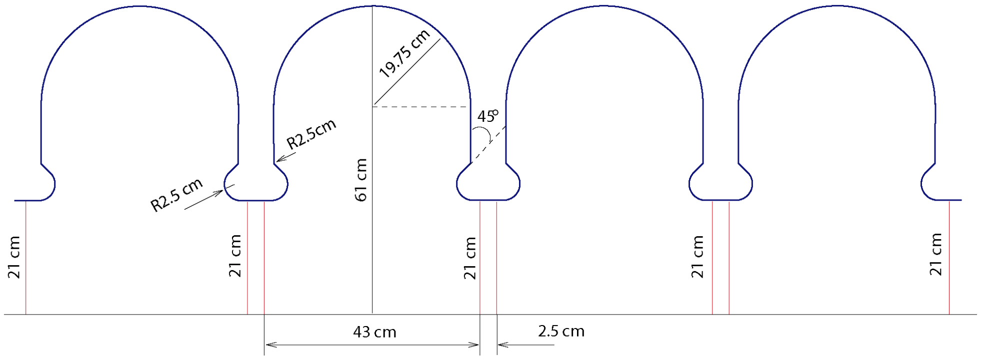

Figure 6.7.: Schematic of the RF cavities in the MICE cell. The irises of the cavities are shown at 21 cm. Figure taken from [78].

6.3.2. Optics

The transverse betatron function, $\beta_\perp$, along the beam-axis, z, is shown in fig. 6.8. The smallest value of $\beta_\perp$ is obtained by the MICE lattice ($\beta_\perp$ ~40 cm) as a result of the extra coil (coupling coil). Because of this low $\beta_\perp$ value the MICE-like cell is expected to achieve the lowest equilibrium emittance and therefore the best cooling out of all four lattices. It must be noted that the

MICE experiment needs to have a small equilibrium emittance, as measurable emittance reduction must be obtained for the cooling demonstration. This requirement can be relaxed in the final Neutrino Factory cooling lattice. The FSIIA cell, shown in red, has the smallest betatron variation amplitude, centred around $\beta_\perp$ =80 cm. Due to the small $\beta_\perp$ amplitude it is expected that the transmission of FSIIA will be better than the other lattices which have a larger amplitude. The different coil geometry in Doublet-1 and -2 results in a different betatron oscillation minima: Doublet-1 cell has minima at $\beta_\perp$ ~0.75 and at $\beta_\perp$ ~0.85 m whereas the Doublet-2 cell's minima are at $\beta_\perp$ ~0.79 and 0.77 m. Since one of Doublet-1 minima is relatively larger than those of Doublet-2, it is expected that Doublet-2 will achieve a better cooling than Doublet-1. Moreover, because of the similar amplitude of $\beta_\perp$ it is also expected that these two lattices, and the MICE-like cell, will have a similar transmission. Nevertheless, the betatron oscillations of the Doublet lattices have large variations which is expected to have a negative effect on the transmission of the two lattices.

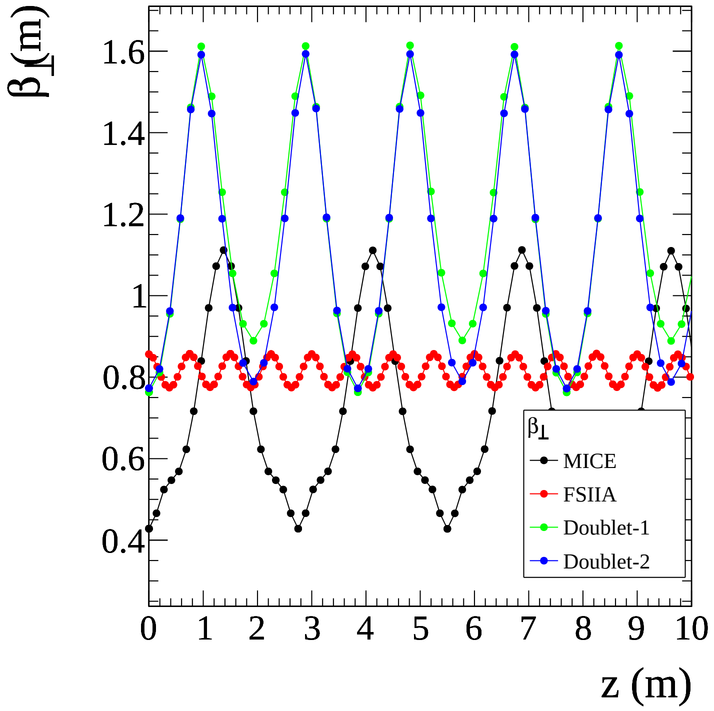

Figure 6.8.: Transverse betatron function, $\beta_\perp$, with respect to the beam-axis.

Fig. 6.9 illustrates the transverse betatron function, $\beta_\perp$, with respect to the momentum, P, for every lattice. As shown in this figure, MICE has a resonance close to ~250 MeV/c, which is the reason its beam was chosen to be input with momentum centred at 200 MeV/c. The Doublet lattices perform similarly, and MICE and FSIIA have a small gradient between 180 and 240 MeV/c, which suggests a good performance.

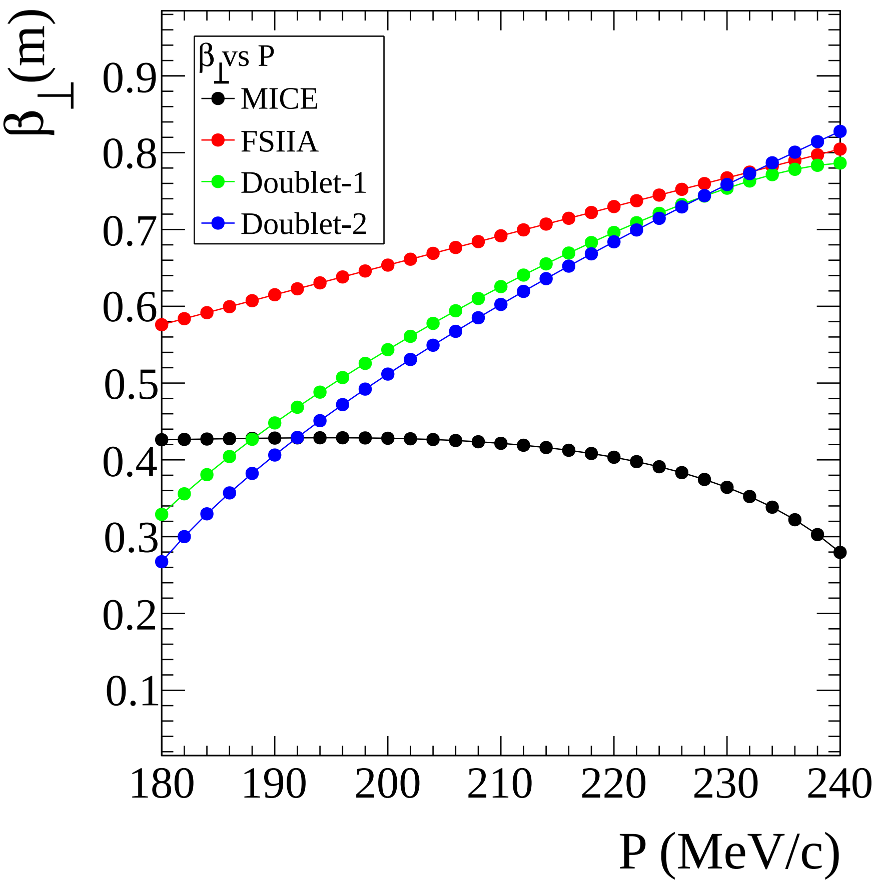

Figure 6.9.: Transverse betatron function, $\beta_\perp$, with respect to the total momentum, P, of each lattice. $\beta_\perp$ was calculated at zero magnetic field. The smaller gradient of MICE and FSIIA suggest a better efficiency for these two lattices.

6.3.3. Simulation

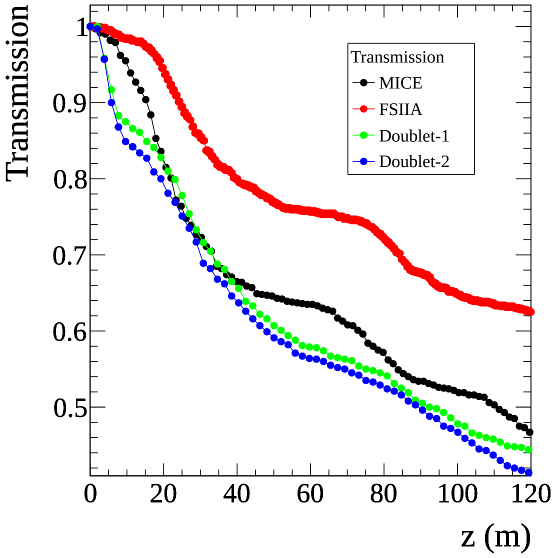

(a) Transmission along the beam-axis. FSIIA achieves the best transmission over all the lattices.

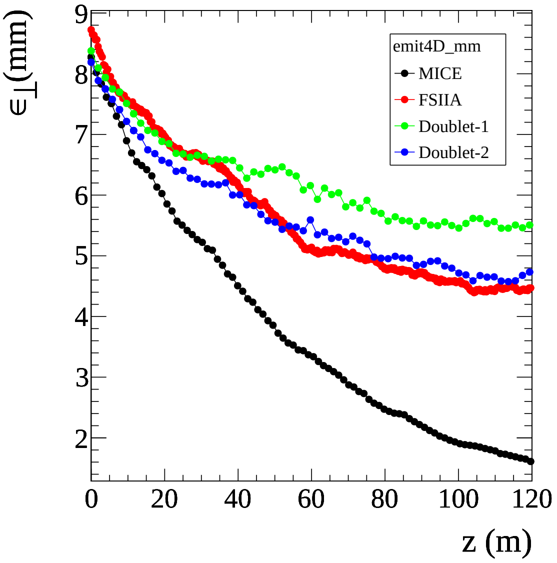

(b) Transverse emittance along the beam-axis. The best equilibrium emittance (less than 2 mm) is achieved by the MICE-like cell.

Figure 6.10.: Transmission and cooling dynamics in all lattices.

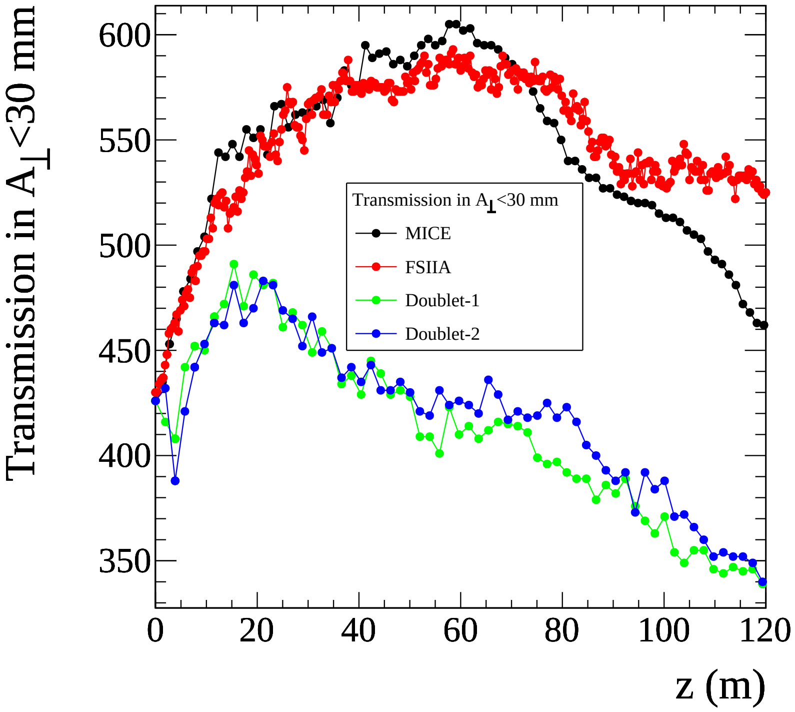

Figure 6.11.: Transmission within 30 mm of $\epsilon_\perp$ along the beam-axis. The Doublet lattices do not perform as well as the FSIIA and MICE-like cells, due to the large variations in $\beta_\perp$ (fig. 6.8) and the large gradient of $\beta_\perp$ vs P (fig. 6.9).

Fig. 6.10a shows the number of muons (transmission) along the beam-axis, z, throughout the lattices. No cuts were used for this plot. It is clear that the best muon transmission is obtained by the FSIIA lattice where ∼60% of the particles survive and manage to reach 120 m length. For the same length, the MICE-like cell and Doublets achieve a ∼45% transmission.

Fig. 6.10b presents the transverse emittance ($\epsilon_\perp$) reduction along the beam-axis. For this plot, only the particles that managed to reach the end of the lattices were taken into account. Therefore, even if the initial transverse emittance was 10 mm for all lattices, the initial emittance in fig. 6.10b is $\epsilon_\perp \neq 10$ mm. The best cooling performance ($\epsilon_\perp$ reduction: factor of five) is achieved by the MICE-like cell. This is expected as this lattice is shown to have the lowest betatron function out of all the lattices (see fig. 6.8). The FSIIA and Doublet-2 cells have a similar cooling effect on the beam, reducing the emittance by a factor of 2 and ∼1.7 respectively within 120 m. The Doublet-1 cell has a slightly smaller emittance reduction than the Doublet-2 cell (emittance reduction: factor of ∼1.5). Note that both the transmission and cooling results come in a perfect agreement to what was expected from fig. 6.8.

The cooling effect is defined by the number of simulated particles that are within the expected acceptance of the downstream accelerator. The squared amplitude, $A_\perp^2$, is defined by [40]:

$$A_\perp^2 = \frac{p_z}{m}\left[\beta_\perp(x'^2 + y'^2) + \gamma_\perp(x^2 + y^2) + 2\alpha_\perp(xx' + yy')\right] \\ + \frac{p_z}{m}\left[2(\beta_\perp k - L)(xy' - yx')\right], \tag{6.3.1}$$

where $\beta_\perp, \alpha_\perp, \gamma_\perp$ are the solenoidal equivalents of the Twiss parameters (defined in chapter 3), k is the solenoidal focusing strength and L is the dimensionless kinetic angular momentum. Fig. 6.11 presents the transmission within 30 mm of transverse acceptance, $\mathrm{A}_\perp$. The best transmission of 60% is achieved by MICE and FSIIA at similar distances (60 m and 70 m respectively). On the other hand, the Doublet cells do not perform as well as the other two lattices, with their maximum achieved transmission close to 50%. The low transmission of the two Doublets is a result of their large betatron variations and the large minimum β-function, together with their large gradient of $\beta_\perp$ *vs* P (see figures 6.8 and 6.9). Therefore, since FSIIA achieves the best transmission and the MICE-like cell the best cooling, more muons survive the 30 mm transverse acceptance cuts in these lattices than in the Doublet cells.

6.4. Conclusions

Two new lattices, Doublet-1 and Doublet-2, were designed aiming to achieve a low magnetic field at the position of the RF cavities in order to mitigate the RF breakdown, while at the same time achieving a comparable transmission within 30 mm of $A_\perp$ to the FSIIA lattice.

The Doublet cells were compared with respect to the transmission and cooling dynamics to a MICE-like cell, used for pedagogical reasons, and to the FSIIA cell. The magnetic field was significantly reduced in the two Doublet lattices with a B_{tot} field value eight times smaller than that of FSIIA (fig. 6.6).

The transmission and cooling performance of the Doublet cells were not, on the other hand, as good as in the MICE and FSIIA case. This was attributed to the large variations of the betatron function and the large gradient of $\beta_\perp$ vs P. The transmission within 30 mm of $A_\perp$ in the Doublet cells was found to be more than 10% smaller than in the other two lattices.

Therefore a new lattice still needs to be found that not only significantly reduces the magnetic field at the position of the RF cavities, but that also achieves a comparable transmission and cooling performance to the FSIIA lattice.

Chapter 7

The Bucked Coils Lattice

The use of Doublet-1 and Doublet-2 in chapter 6 has been shown to reduce the magnetic field at the RF position. However the muon transmission in those lattices was substantially lower than in the FSIIA lattice.

A *novel* idea is presented in this chapter, based on the use of two homocentric coils of opposite polarity, placed at the same position along the beam-axis. This pair of coils is called “Bucked Coils” (BC). The polarity of each coil will alternate with every repeat of the pair resulting in a magnetic field reduction at off-axis positions[1]. A new lattice design is proposed, based on the Bucked Coils configuration[2].

7.1. Lattice Description

The Bucked Coil layout can be seen in fig. 7.1. A pair of two homocentric coils, inner and outer, with opposite polarities (purple and blue represent positive and negative polarities respectively) form a pair of Bucked Coils, illustrated in fig. 7.1a. Fig. 7.1b shows how the polarity alternates with every repeat of a Bucked Coils pair.

---

[1] Of course, because of geometry, the magnetic field at the z position corresponding to the centre between two pairs of coils would have a full on-axis magnetic field cancellation (same as in the lattices presented in chapter 6).

[2] The concept of bucked coils was first discussed by Richard Fernow [99]; however the results he obtained were not optimistic. None of the values discussed in R. Fernow’s presentation were used for the results presented in this thesis, as his presentation was only found after this thesis’ viva.

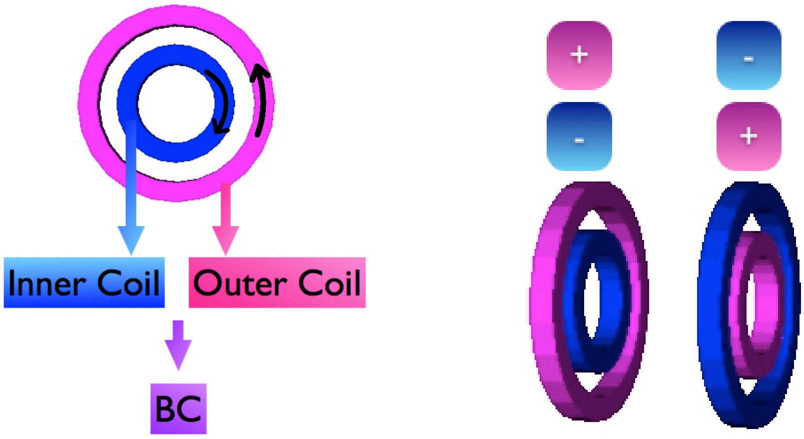

(a) A pair of Bucked Coils. The inner and outer coils are shown in blue and purple representing negative and positive polarities respectively.

(b) The polarity of the Bucked Coils alternates with every pair repeat.

Figure 7.1.: Visualisation of the Bucked Coils concept.

The "Bucked Coils lattice" (BC), shown in fig. 7.2a, makes use of two methods that can lower the magnetic field at the position of the RF cavities:

(a) a large cell length,

(b) the use of the Bucked Coils configuration.

This lattice has the same components as the FSIIA lattice, differing only in the cell length (BC has a larger cell length than FSIIA) and in the use of a *pair* of coils rather than a single coil that FSIIA uses (see FSIIA cell description in section 6.1): BC starts with a pair of Bucked Coils, followed by one RF cavity with a Lithium Hydride (LiH) absorber on each side. Fig. 7.2 presents the Bucked Coils and FSIIA cells to emphasise the similarities between them.

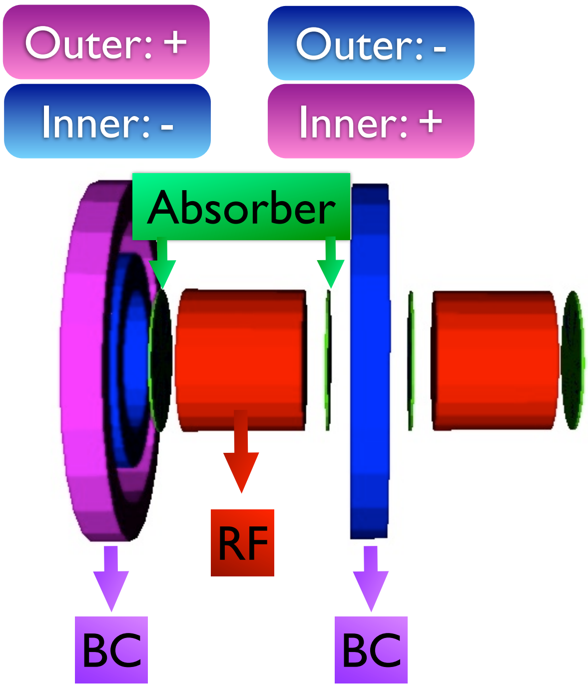

(a) Bucked Coils (BC) full-cell. BC starts with a pair of bucked coils, followed by one RF cavity that has a LiH on each side.

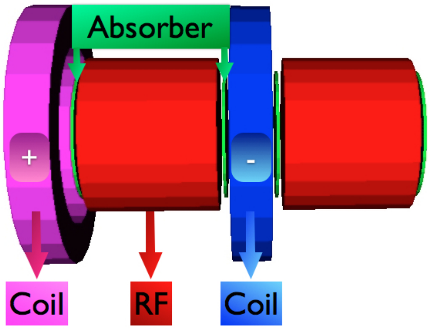

(b) FSIIA full-cell.

Figure 7.2.: (a) Bucked Coils and (b) FSIIA full-cells. These lattices consist of the same components apart from the fact that the Bucked Coils lattice uses a *pair* of coils and has a larger cell-length.

Numerous Bucked Coils lattices were created, differing in radius, length, and current densities, aiming to find the lattice that reduces the magnetic field without compromising the cooling dynamics and transmission.

Table 7.1.: Main characteristics of FSIIA and BC-I. Note that “IC” and “OC” correspond to “Inner Coil” and “Outer Coil” respectively.

Lattice	**FSIIA**	**BC-I**
Full-cell Length [m]	1.5	2.1
Number of RF cavities	2	2
Number of Absorbers	4	4
Number of Coils	2	4 (2 pairs)
RF Cavities		
Peak Electric Field [MV/m]	15.000	16.585
Phase [degrees]	40	30
Length [m]	0.5	0.5
Radius [m]	0.3	0.3
Absorbers		
Length [m]	0.0115	0.0100
Radius [m]	0.25	0.30
Coils		
Current Density [A/mm^2]	106.667 N/A	IC: 120.000; OC: 90.240
Inner Radius [m]	0.35 N/A	IC: 0.30; OC: 0.60
Thickness [m]	0.15 N/A	IC: 0.15; OC: 0.15
Length [m]	0.15 N/A	IC: 0.15; OC: 0.15

Four versions are presented in this chapter, which for simplicity are named BC-I, -II, -III and -IV. It should be stressed that BC-IV was created aiming not only to reduce the magnetic field, but to also reduce the hoops stress acting on the coils (hoops stress will be discussed thoroughly in chapter 9). Table 7.1 summarises the main characteristics of FSIIA and BC-I, whereas table 7.2 summarises the differences between the versions of the Bucked Coils lattice.

Table 7.2.: Summary of the differences between the four BC-versions presented in this section.

Lattice	**BC-I**	**BC-II**	**BC-III**	**BC-IV**
Full-cell Length [m]	2.10	1.80	1.80	1.80
Coils				
Current Density [A/mm^2]	IC: 120.000; OC: 90.240	IC: 128.070; OC: 112.800	IC: 132.000; OC: 99.264	IC: 120.000 OC: 90.000

7.2. Results

7.2.1. Magnetic field

The effect of the magnetic field reduction at the position of the RF cavities is shown in figure 7.3, with the individual outer and inner coil fields superimposed. The combination of the two fields is also indicated.

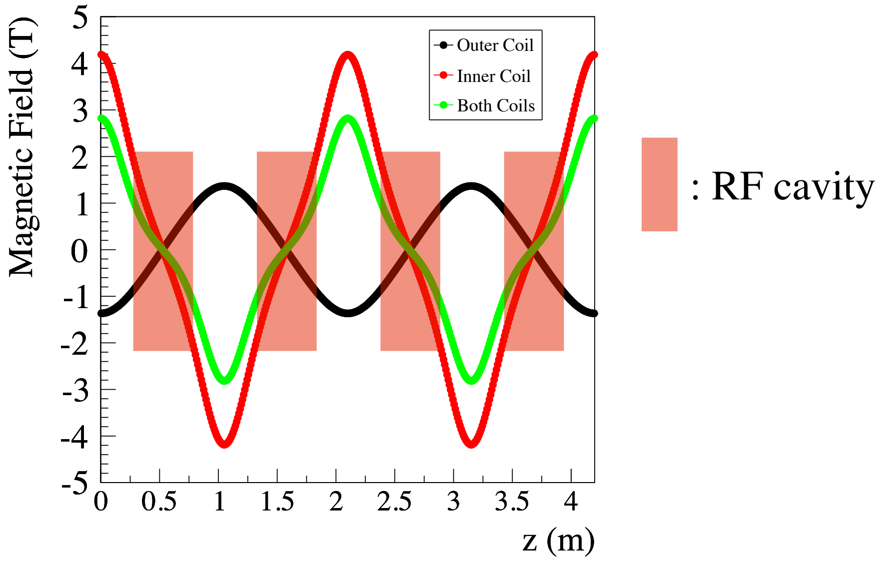

Figure 7.3.: Superposition of the Outer Coil (black) and Inner Coil (red) fields. The resulting field is shown in green. Only the the longitudinal on-axis fields (B_z) are shown. Note that the total magnetic field has a smaller gradient (smoother change) within the RF cavities.

Figure 7.4 shows the total magnetic field, B_{tot}, of FSIIA and BC-I[3] plotted with respect to the beam-axis, z, and radius, y (x was set to zero). The beam-axis in this plot starts from the centre of the lattices' coil(s) and ends at the centre of their RF cavities[4]. Note how, as was expected due to geometry, both lattices have zero on-axis B_{tot} at the centre of their cavities. What is interesting to note though is the extension, in both z and y, of the region with $0<B_{tot}<0.5$ T: this region is smaller than $y\sim10$ cm in radius in FSIIA, whereas it extends to more than $y\sim60$ cm in BC-I. Moreover, this region is significantly larger in the z-direction for BC-I than for FSIIA. Finally the areas with $B_{tot}<0.2$ T and $B_{tot}<0.1$ T are much larger in BC-I.

---

[3] The other BC-versions are not shown as they present similar results to BC-I. This comparison is only to emphasise the difference in the magnetic field behaviour when the Bucked Coils are used, rather than a single coil.

[4] Larger values of z are not shown as due to symmetry, the result will be the mirror image of this magnetic field.

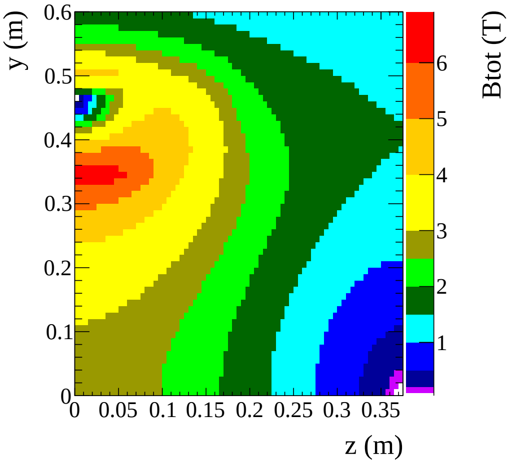

(a) FSIIA

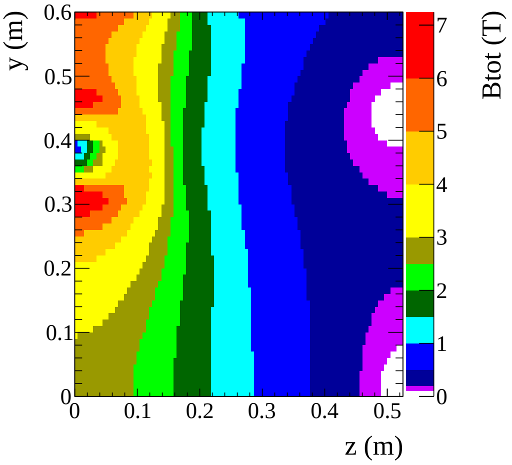

(b) BC-I

Figure 7.4.: Total magnetic field, B_{tot} (in T) of (a) FSIIA and (b) BC-I, with respect to the beam-axis, z, and radius, y (x was set to zero; length is in mm). In both plots, z=0 corresponds to the z-position at the centre of the coil(s), whereas z=375 mm and z=525 mm correspond to the z-positions at the centre of the RF cavities of FSIIA and BC-I respectively. Blue corresponds to $0.5<B_{tot}<1$ T, dark blue corresponds to $0.2<B_{tot}<0.5$ T, violet to $0.1<B_{tot}<0.2$ T and white to $0<B_{tot}<0.1$ T. Both plots have zero B_{tot} at the centre of their RF cavities, on-axis (for y=0 mm), which was expected since the polarity of the lattices' coils was alternating with every repeat. However, B_{tot} is decreased significantly in BC-I within the area of the RF cavities: in FSIIA the area with $B_{tot}<0.5$ extends to less than $y\sim10$ cm, whereas in BC-I, it extends to more than $y\sim60$ cm, and to much larger z values. Finally, the areas with $B_{tot}<0.2$ T and $B_{tot}<0.1$ T are notably larger in BC-I.

The magnetic field lines of FSIIA and BC-I are shown in fig. 7.5 from the coils' centre to the centre of their RF cavities in z, and from the coils' centre to 60 cm in radius. The main difference lays around radius ~40 cm, for z<~10 cm. The components of the magnetic field vectors shown here are (B_r, B_z). These plots were created using MATLAB [100].

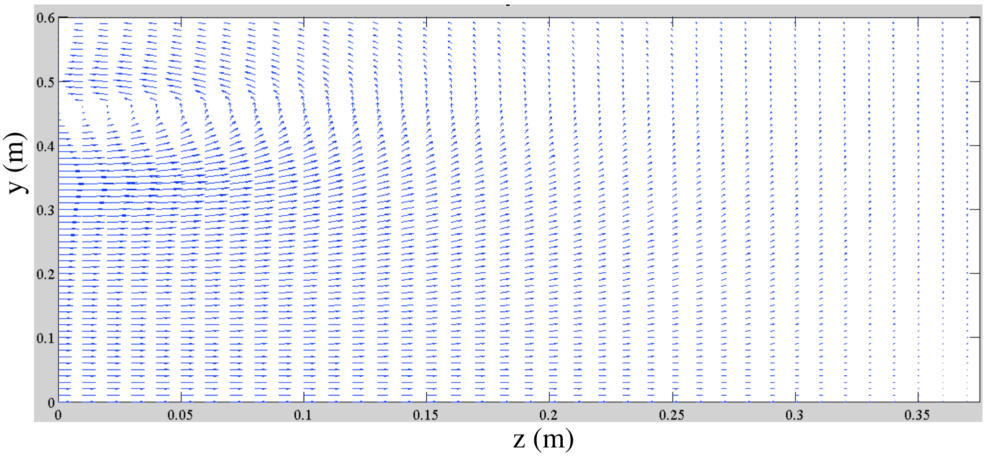

(a) FSIIA

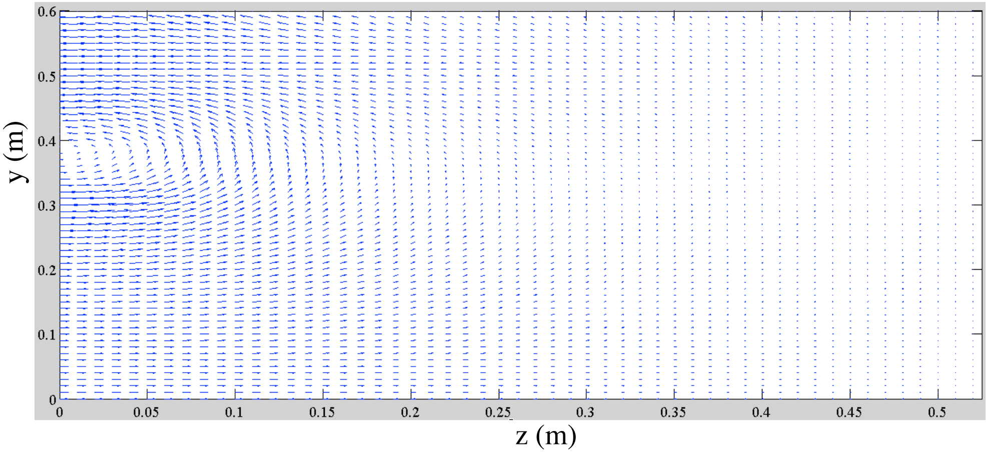

(b) BC-I

Figure 7.5.: Magnetic field lines of FSIIA and BC-I along the beam-axis and radius (y here corresponds to the radius, as x=0). The magnetic field vectors are (B_r, B_{tot}). The main difference between these plots lays around radius ~40 cm for z<~10 cm.

The magnetic field on the beam-axis at the position corresponding to the end of the RF cavity is plotted along the beam-axis, z, for each lattice. The same colour code is used for all the results in this chapter.

The total magnetic field, B_{tot}, achieved by the Bucked Coils is significantly lower than that of FSIIA (see fig. 7.6). At 38 cm FSIIA obtains more than

4 T. At this radius, BC-I achieves a B_{tot} value almost five times smaller, and the other BC lattices a value more than 2.5 times smaller.

For a better understanding, B_z and B_r are plotted as a function of the radius for the same z position. The maximum B_z of FSIIA is obtained at 30 cm, i.e. close to the iris position, and is three to five times larger than the B_z of all BC lattices. Most importantly, at this radius, which as mentioned in sec. 5.3 is the most sensitive with respect to the RF breakdown, all the BC lattices have practically zero B_z (33-35 cm, see fig. 7.7a). At 42 cm radius, the B_r of the FSIIA lattice (shown in fig. 7.7b) exceeds 3.8 T, and at this radius all the BC lattices achieve less than 1.3 T.

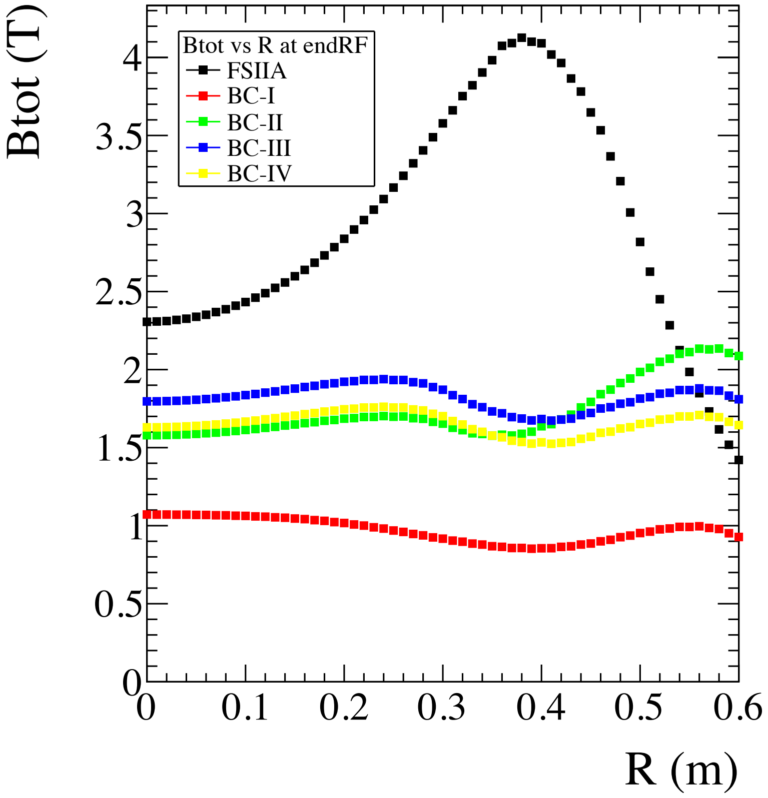

Figure 7.6.: Total Magnetic field with respect to the beam-axis, z. The magnetic field is significantly reduced when the Bucked Coils are used. FSIIA is shown in black, whereas BC-I, -II, -III and -IV are shown in red, green, blue and yellow respectively.

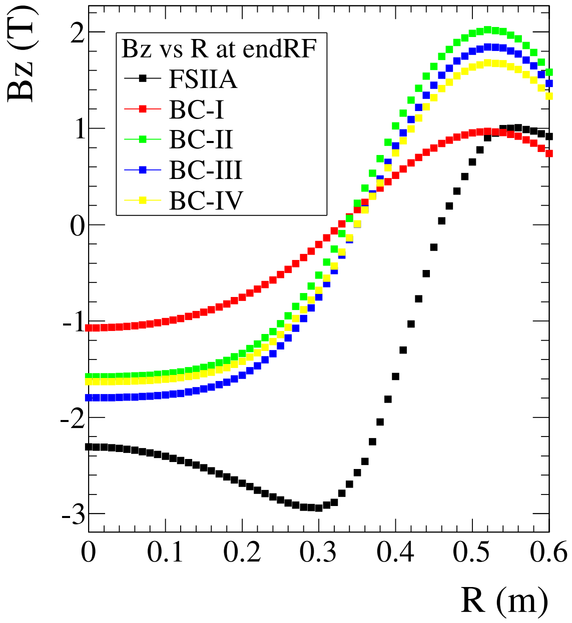

(a) B_z with respect to R. At ∼30 cm FSIIA achieves its maximum B_z whereas all BC lattices obtain virtually zero B_z.

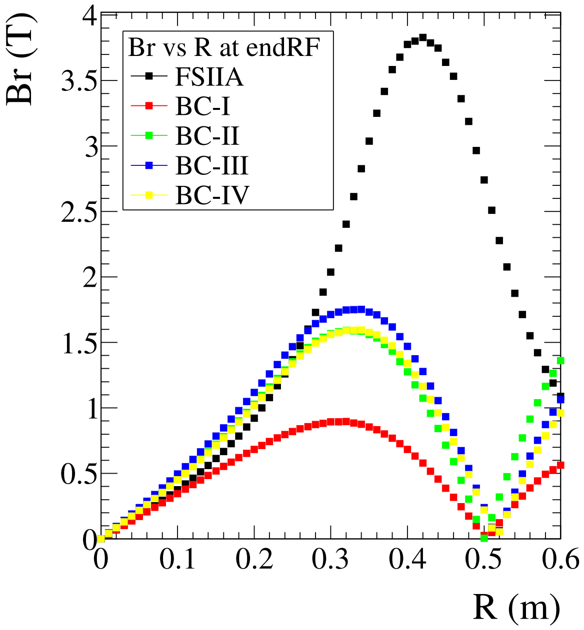

(b) B_r with respect to R. The maximum B_r of all the Bucked Coils is noticeably lower than that of FSIIA.

Figure 7.7.: Comparison of the longitudinal, B_z, and transverse, B_r, magnetic field components in the FSIIA and the Bucked Coils lattices.

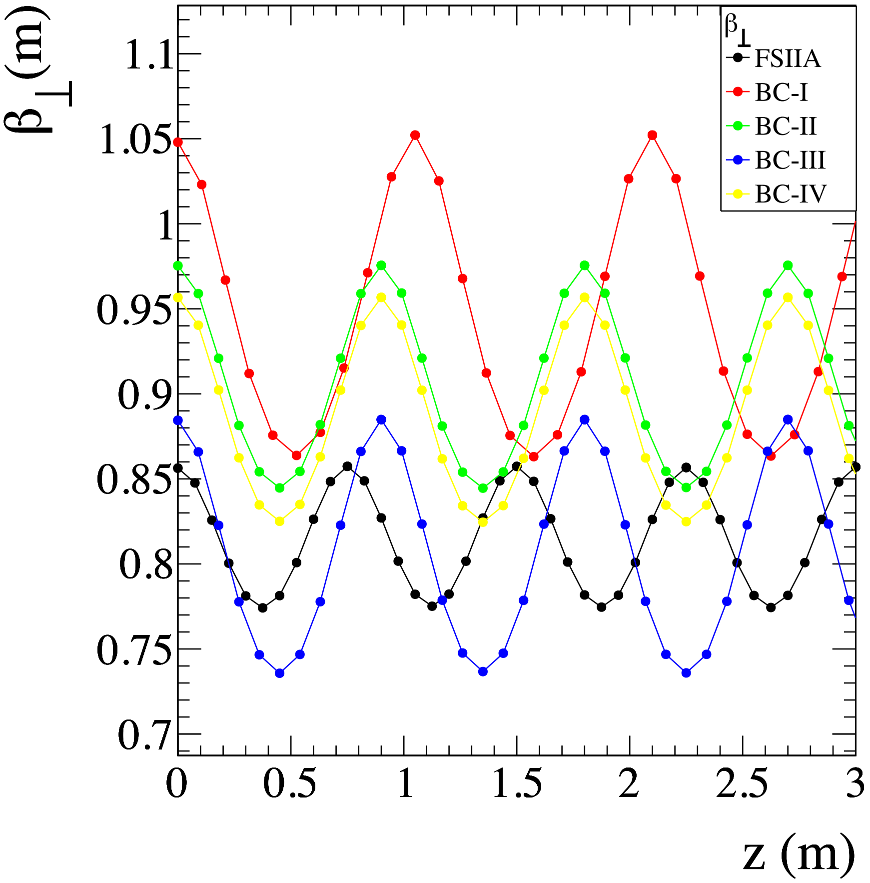

Figure 7.8.: Transverse betatron function, $\beta_\perp$, along the beam-axis, z.

The transverse betatron function oscillations, $\beta_\perp$, of all lattices is illustrated in fig. 7.8. BC-III (shown in blue), obtains the lowest betatron function minimum, closely followed by FSIIA (shown in black). Since equilibrium emittance is proportional to $\beta_\perp$ (see equation 3.8.4), these two lattices are expected to achieve the best cooling overall. Following this argument, the other BC lattices are expected to achieve a worse emittance reduction. Nonetheless they are within cooling limits.

Fig. 7.9 illustrates the transverse betatron function, $\beta_\perp$, at the coil's position with respect to the momentum, P, for each lattice. All lattices show a linear relation between $\beta_\perp$ and P. At P=232 MeV/c, the blue line, corresponding to BC-III, has the lowest $\beta_\perp$ and BC-I the largest $\beta_\perp$, which is consistent with fig. 7.8. The small gradient of BC-III and FSIIA suggests a good and similar transmission performance for these two lattices.

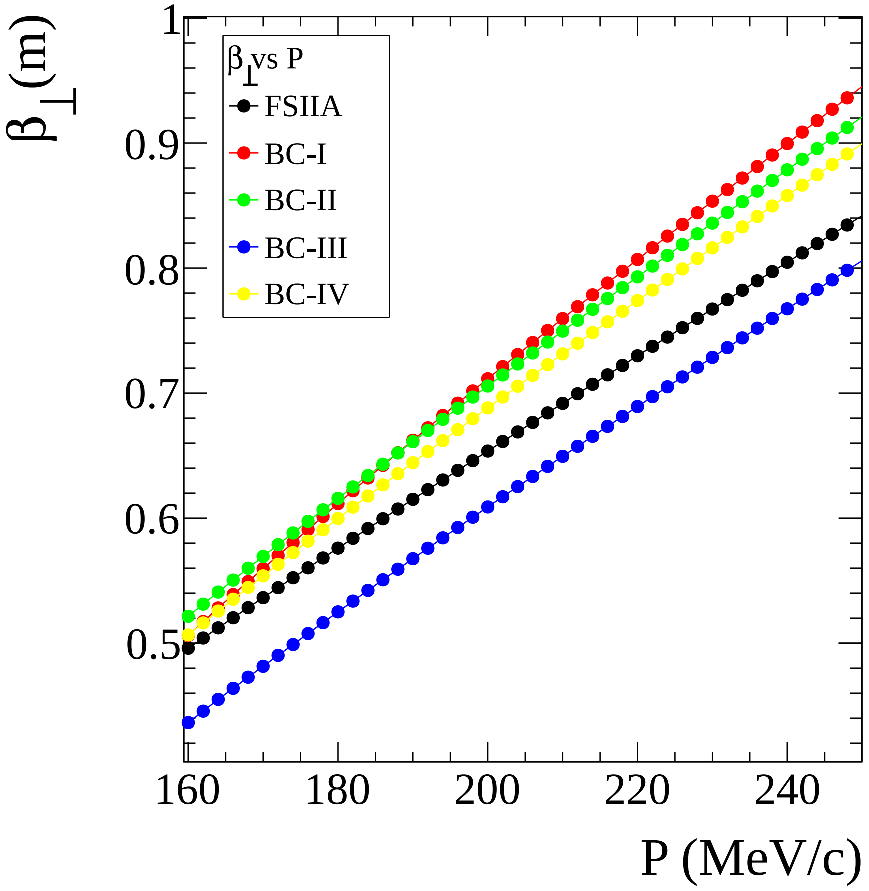

Figure 7.9.: Transverse betatron function, $\beta_\perp$, with respect to different momenta, P. $\beta_\perp$ was calculated at a zero magnetic field position for each lattice.

7.2.2. Simulation

The muon transmissions, obtained for each lattice without cuts, are shown in fig. 7.10a. All BC lattices achieve an appreciably larger transmission than FSIIA: at 150 m, FSIIA transmission is 15% lower than BC-I and -III, and 20% lower than BC-II and -IV.

The transverse emittance reduction along the beam-axis is shown in fig. 7.10b. As in sec. 6, the only particles that were taken into account for this plot, were those that managed to reach the end of the lattice; all other particles were neglected as they would give a wrong appreciation of the cooling factor. Therefore, as in section 6, although the initial transverse emittance was 10 mm for all lattices, the starting emittance in this plot is $\epsilon_\perp \neq 10$ mm. The expectations that arose from plot 7.8, are validated: FSIIA and BC-III achieve the best $\epsilon_\perp$ reduction within 150 m (factor of ∼2), followed by BC-IV and -II (factor of

$\sim$1.8), and BC-I (factor of $\sim$1.7).

One of the most important plots of this section is shown in fig. 7.11, which presents the muon transmission within 30 mm of transverse acceptance, $A_\perp$ (defined in section 6.3.1.). Some of the Bucked Coils versions result in a substantial increase in the transmission. The maximum transmission is obtained at 90 m by BC-II, closely followed by BC-III and -IV. The maximum transmission of FSIIA is found at 70 m, where all BC lattices, apart from BC-I, achieve a higher transmission. What is of great importance is that BC-I, i.e. the lattice that achieves almost five times smaller B_{tot} than FSIIA (see fig. 6.5), obtains *only* 1% smaller transmission at the position of FSIIA maximum, and this difference is of course insignificant. Note that at $\sim$80 m, BC-I and FSIIA have the same transmission, and at this location the transmission of all other BC lattices is larger.

It should be stressed that since BC lattices have a larger cell than FSIIA, a smaller number of cells will be needed for the construction of the same lattice length. For instance, for a 70 m lattice, FSIIA would need $\sim$93 0.75 m cells, whereas BC-I would need $\sim$67 1.05 m cells. Even though for each BC cell twice as many solenoidal coils are needed by definition, which may have an implication for the total cost, RF cavities are considered to be the most costly component.

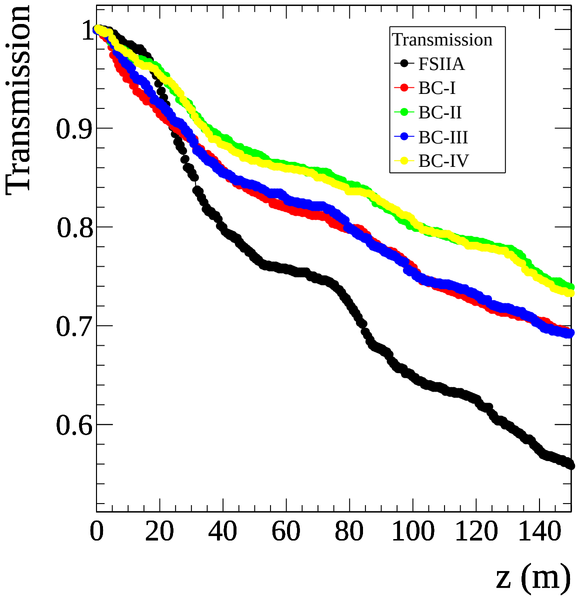

(a) Transmission along the beam-axis. All BC have a substantially better transmission than the FSIIA lattice.

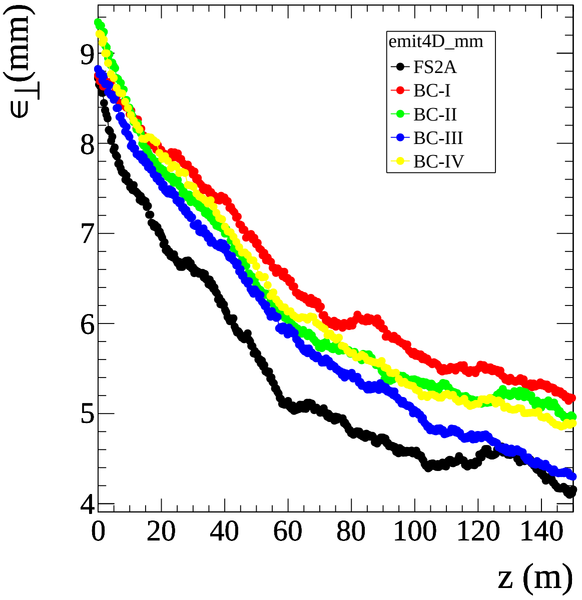

(b) $\epsilon_{\perp}$ decrease along the beam-axis. The FSIIA and BC-III have practically the same equilibrium emittance, closely followed by the other BC lattices.

Figure 7.10.: (a) Transmission and (b) transverse emittance along the beam-axis, z, for the FSIIA and BC lattices.

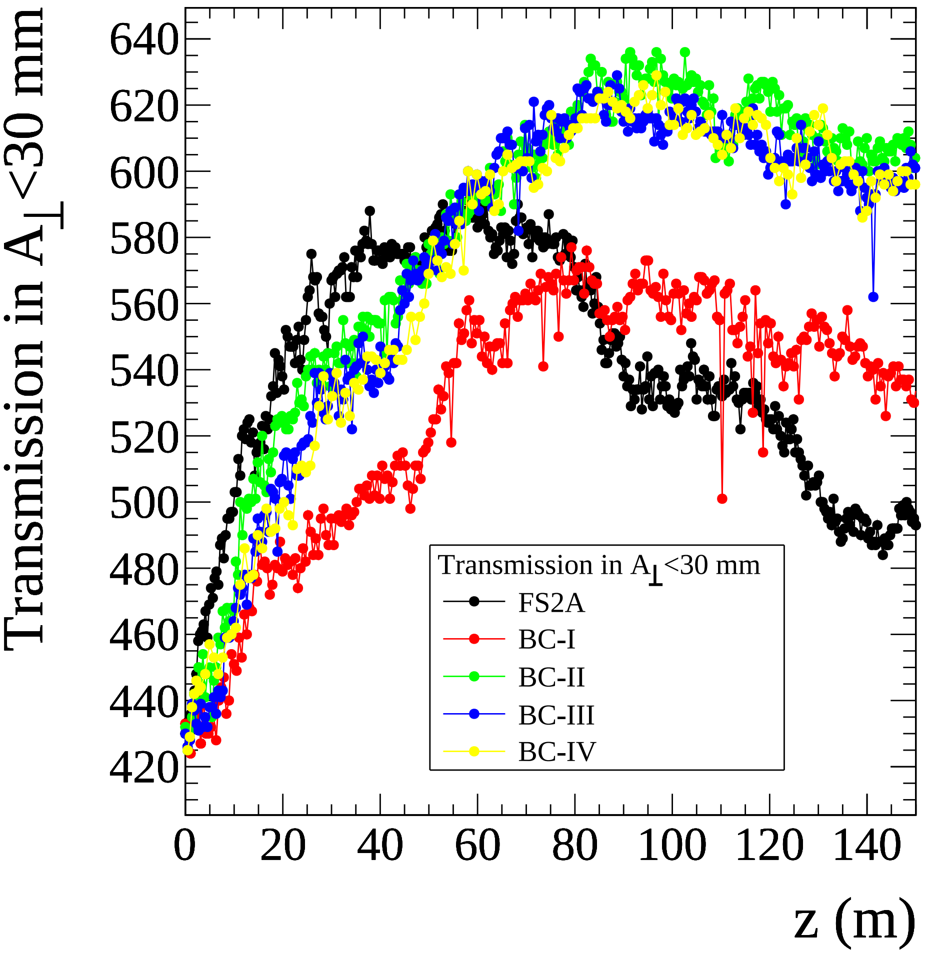

Figure 7.11.: Transmission within 30 mm of transverse acceptance, $A_\perp$, along the beam-axis, z. All the Bucked Coils lattices achieve a comparable or better transmission than the FSIIA lattice. It should be stressed that at 70 m, where FSIIA achieves its maximum transmission, BC-I (the lattice that obtains almost five times smaller B_{tot} at the RF position than FSIIA) has as little as 1% smaller transmission than FSIIA, which is an insignificant difference.

It should be highlighted that from fig. 7.9, a similar transmission performance was expected between the FSIIA and BC lattices, since they all present a similar gradient of $\beta_\perp$ with respect to P. In particular, BC-III behaviour is close to that of FSIIA, which should imply a comparable performance between these two lattices. In an attempt to explain the low transmission of the FSIIA lattice, the phase advance of each lattice was calculated. For this calculation the full-cell length was taken into account and equation 3.3.5 was used in a user-written script. The phase advance was calculated for three different momenta: for the reference momentum of 232 MeV/c and for ±20% momentum deviations (278.4 and 185.6 MeV/c). Note that this equation gives the phase advance in radians but the results given below are in degrees.

As can be seen in both table 7.3 and fig. 7.12, the phase advance of all lattices does not cross the main stability limits (at 0^o and 180^o) that would cause any immediate instabilities in the particles movement. This suggests that the low transmission of FSIIA in comparison to the BC lattices, is not due to the phase advance. It is possible that the non-linearities of the magnetic field affect differently the FSIIA and BC lattices. However, the effect was not fully understood.

Table 7.3.: Phase advance calculated for a full-cell length of each lattice.

Lattice	**232-20%**	**232**	**232+20%**
FSIIA	130.2	103.3	85.9
BC-I	157.7	125.1	103.3
BC-II	141.1	111.8	92.6
BC-III	158.8	125.8	104.5
BC-IV	143.9	113.3	94.6

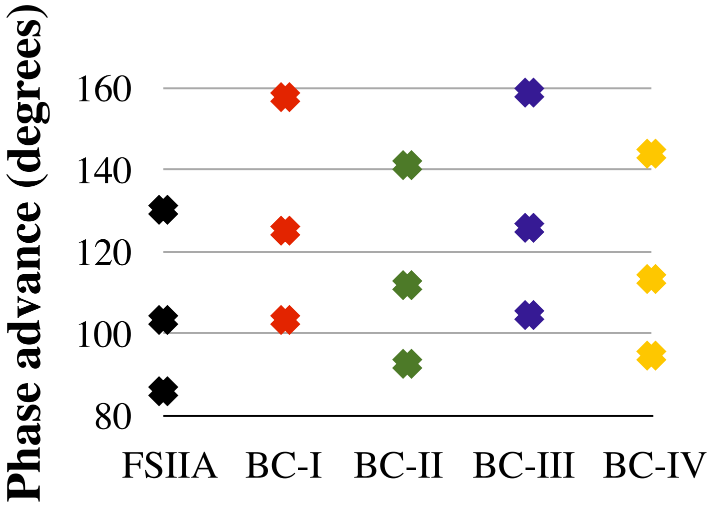

Figure 7.12.: Phase advance in degrees for each lattice. The lower value corresponds to $P = (232 + 232 \cdot 20\%)$ MeV/c, the middle to $P = 232$ MeV/c, and the higher value to $P = (232 - 232 \cdot 20\%)$ MeV/c.

7.3. Using a Realistic Beam

A “realistic” beam was created[5] to verify the results of the Bucked Coils lattices. The term “realistic” is used as this beam has the same characteristics as the one that will be produced at the Front End of the Neutrino Factory. The beam was simulated using the pion production model from the MARS code, taking into account the magnetic field in the decay channel and all the effects in the drift, buncher and phase rotation sections.

The momentum distribution of this beam, shown in fig. 7.13a, had a very large spread (RMS: 66.95 MeV/c) and therefore only particles with momentum within $(232\pm232\cdot20\%)$ MeV/c were taken into account for tracking. This initial momentum cut is illustrated in fig. 7.13a in blue. The new momentum distribution, with a mean momentum at 233.6 MeV/c (RMS: 20.73 MeV/c), is shown in fig. 7.13b.

---

[5] This beam was created by Dr. C. Rogers [101].

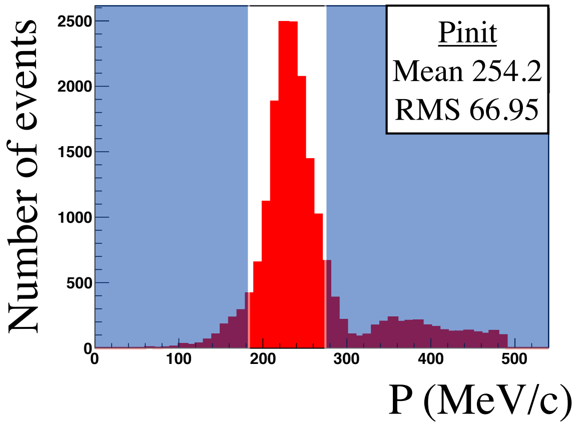

(a) Initial total momentum distribution of the realistic beam. Particles with momentum outside 232±20% (i.e. at the blue areas of the plot), were not included in the input file for the simulation.

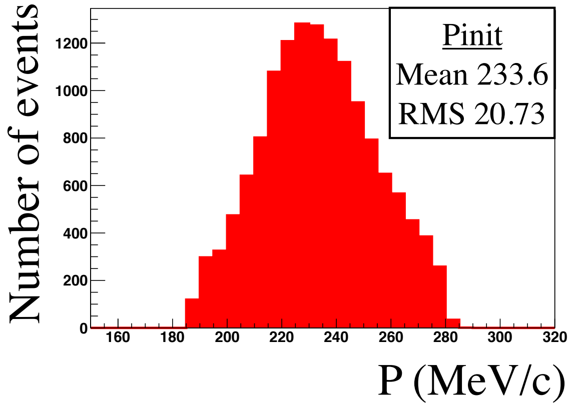

(b) Total momentum distribution after initial momentum cuts were applied.

Figure 7.13.: Momentum distribution of the realistic beam, (a) before and (b) after the initial momentum cuts were applied.

Tables 7.4 and 7.5 present the initial characteristics of this beam, before and after the initial momentum cuts respectively.

Table 7.4.: Realistic beam characteristics before momentum cuts.

Parameter	**Value**
Number of events	18,946
Transverse emittance (mm)	13.941
Transverse beta (mm)	815.128
Transverse alpha	-0.0058
Longitudinal emittance (ns)	0.566
Longitudinal beta (ns)	3.891
Longitudinal alpha	-0.030

Table 7.5.: Beam characteristics after momentum cuts.

Parameter	**Value**
Number of events	13,976
Transverse emittance (mm)	12.786
Transverse beta (mm)	781.713
Transverse alpha	0.040
Longitudinal emittance (ns)	0.120
Longitudinal beta (ns)	8.752
Longitudinal alpha	0.231

7.3.1. Results

After the initial momentum cut was applied, the beam was input at zero magnetic field and was tracked through 150 m. The number of particles that were within 30 mm of transverse acceptance is shown in fig. 7.14 for all lattices. The maximum transmission is achieved by BC-II, -III, and -IV at ∼120 m. FSIIA has its maximum transmission at ∼70 m, where BC-I transmission is only ∼4% smaller. The transmission of BC-I is maximum at ∼90 m, and at this point it is equal to the FSIIA transmission.

It should be noted that apart from the fact that BC-II, -III, and -IV achieve their maxima at a longer lattice-length, this plot comes in a good agreement with fig. 7.11, where a non-realistic beam was used. In both plots, the best transmission is achieved by BC-II, -III, and -IV, followed by FSIIA and BC-I.

Another interesting point to note is the local maximum of FSIIA at 20 m. It should be highlighted that this local maximum was significantly larger when the whole beam was used, i.e. before the initial momentum cuts were applied, and it is therefore strongly believed this fairly enigmatic transmission behaviour of FSIIA is related to the applied cuts. However, due to time constrains further investigation did not take place. Moreover, since this behaviour could be avoided if different cuts were adapted it is considered to be unimportant.

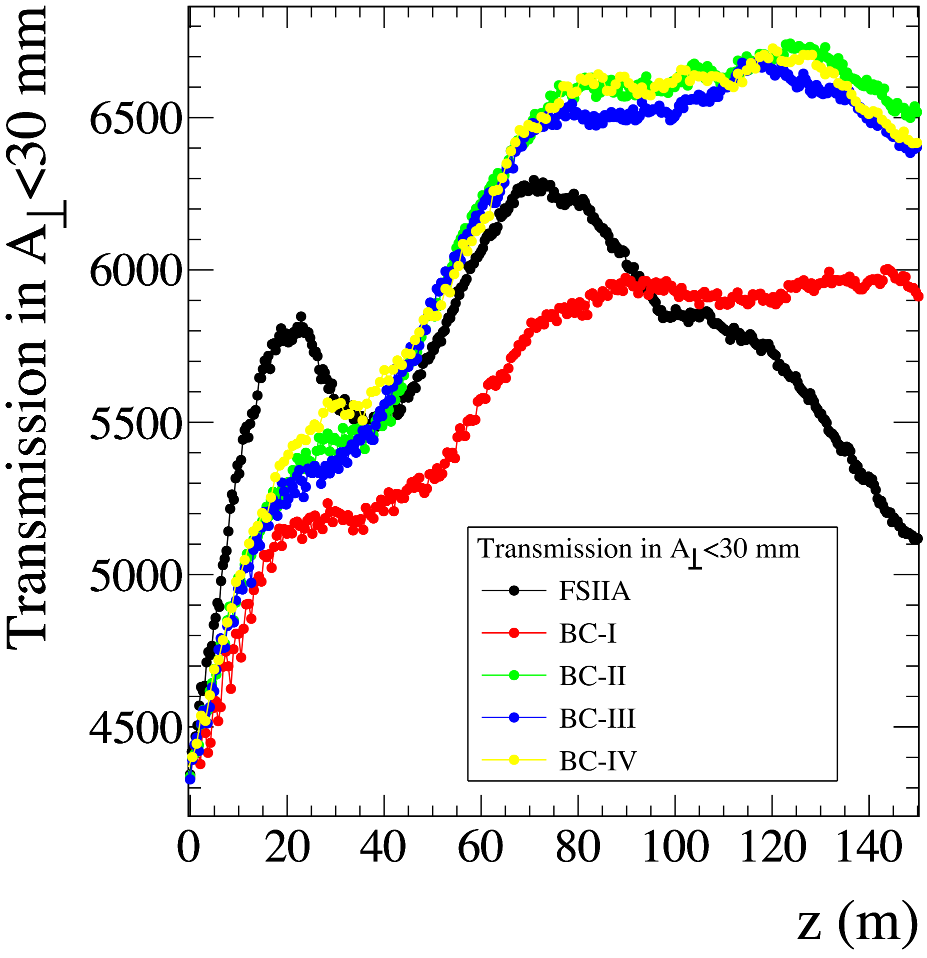

Figure 7.14.: Transmission within 30 mm of transverse acceptance, $A_\perp$, along the beam-axis. The results of this plot come in a good agreement with fig. 7.11 of chapter 7, where a non-realistic beam was used. The local maximum of FSIIA at ∼20 m is believed to be unimportant as it was found that depending on the initial momentum cuts, its amplitude changes; therefore different initial cuts could have completely eliminate it.

7.4. Conclusions

The Bucked Coils (BC), a *novel* idea, was used in the Bucked Coils lattice configuration aiming to mitigate the RF breakdown effect by reducing the magnetic field at the position of the RF cavities. Four different versions of the BC configuration (BC-I, -II, -III, and -IV) were compared to the FSIIA lattice with respect to the magnetic field, transmission, and cooling dynamics.

The total magnetic field, B_{tot} was significantly reduced when the BC configuration was used: B_{tot} was found to be almost five times smaller in BC-I than in the FSIIA at the end of the RF cavities. In addition, at 30 cm radius where FSIIA has its maximum B_z, all BC lattices obtain virtually zero B_z (fig. 7.7a).

The smallest $\beta_\perp$ minimum (fig. 7.8) was obtained by BC-III, closely followed by the FSIIA lattice. All other BC lattices had higher minima and oscillation amplitudes; nonetheless they were all within cooling limits.

The muon transmission (fig. 7.10a), was noticeably larger in the BC lattices: at 150 m BC-II and -IV obtained ∼20%, and BC-I and -III ∼15% better transmission than that of FSIIA. FSIIA and BC-III achieved practically the same $\epsilon_\perp$ reduction (factor of ∼2), closely followed by the performance of the other BC lattices (see fig. 7.10b).

One of the greatest and most important results is the transmission within 30 mm of transverse acceptance, $A_\perp$ (fig. 7.11). The best transmission was achieved by BC-II at ∼90 m with all other BC lattices, apart from BC-I, obtaining a similar transmission at that z position. The maximum transmission of FSIIA was achieved at ∼70 m; at this point, BC-I, the lattice which achieved almost five times smaller B_{tot} than FSIIA at the end of the RF cavities (see fig. 7.6), achieved only 1% smaller transmission than FSIIA, which is an insignificant difference. All other BC lattices at this z position achieved larger transmission than FSIIA.

A realistic beam was created and simulated having the same initial characteristics as the one to be used at the Front End of the Neutrino Factory. The transmission within 30 mm of transverse acceptance for the realistic beam was found to be in a good agreement to the transmission of a non-realistic beam (see fig. 7.11 and 7.14).

Chapter 8

Bucked Coils Optimisation

Optimisation of Bucked Coils involves several degrees of freedom. One could change the length of the cell, while keeping the other parameters constant; the current densities of either or both of the coils could be altered, their radii, and even their relative distance. Numerous configurations were designed to check how the change of these parameters affects the magnetic field and transmission. However, in this section only two methods will be described.

8.1. Decreasing the Length and Current Densities

Several efforts have been made aiming to further improve the transmission achieved by the BC-I lattice, described in sec. 7. Using as a reference the BC-I lattice, more lattices were created with a different cell length. The lattice resulting to the best transmission was the one with half-cell length set at 0.75 m[1]. It was found that the magnetic field of this lattice at the position of the RF walls, despite the resulting high transmission, is comparable in magnitude to that of FSIIA. Keeping the half-cell length at 0.75 m, the current densities of both coils were decreased in steps of 10%, and the transmission and magnetic field were studied. Table 8.1 lists the current densities of each configuration presented here, and the configurations names. Note that BC-0 simply refers to the 0.75 m long configuration, with current densities equal to that of BC-I.

---

[1] The current density of this lattice was the same as that in BC-I. Smaller lengths than 0.75 m were not studied as this length results in high magnetic field at the position of the RF cavities.

Table 8.1.: Current densities in A/mm^2 of the new BC lattices. The half-cell length is fixed at 0.75 m, and the current densities decrease in 10% step. BC-0 corresponds to a lattice with the same current density as BC-I of section 7, but with 0.75 m, rather than 1.05 m, half-cell length.

BC-	**Inner Coil**	**Outer Coil**
0	120.0	90.24
α	108.0	81.2
β	97.2	73.1
γ	87.5	65.8
δ	78.7	59.2

8.1.1. Magnetic Field

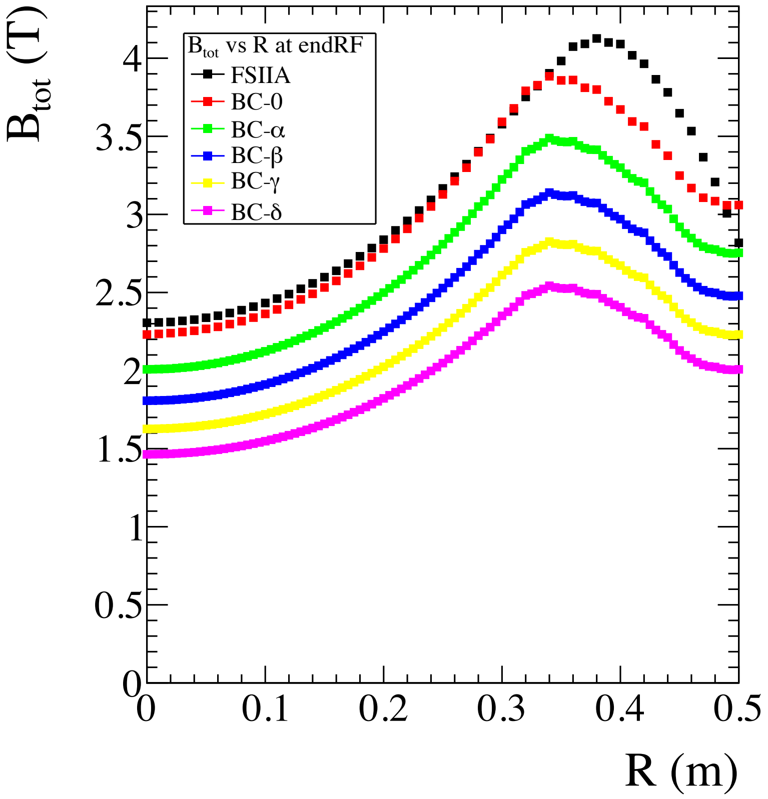

Figure 8.1.: Total magnetic field of FSIIA and the different versions of BC-0. A decrease of 10%, 20%, 30%, 35% and 40% of both inner and outer coils current densities are shown in green, blue, yellow, and purple.

The total magnetic field (fig. 8.1) decreases smoothly as the current densities decrease. The best magnetic field reduction is, as expected, achieved in the lattice with 40% decreased current densities (purple line).

The magnetic field reduction, as was also expected, had a negative effect on transmission (see fig. 8.2). However, it is interesting to note that the yellow and purple lines, although they have a significantly lower B_{tot} than FSIIA, they achieve a very similar, and even better transmission.

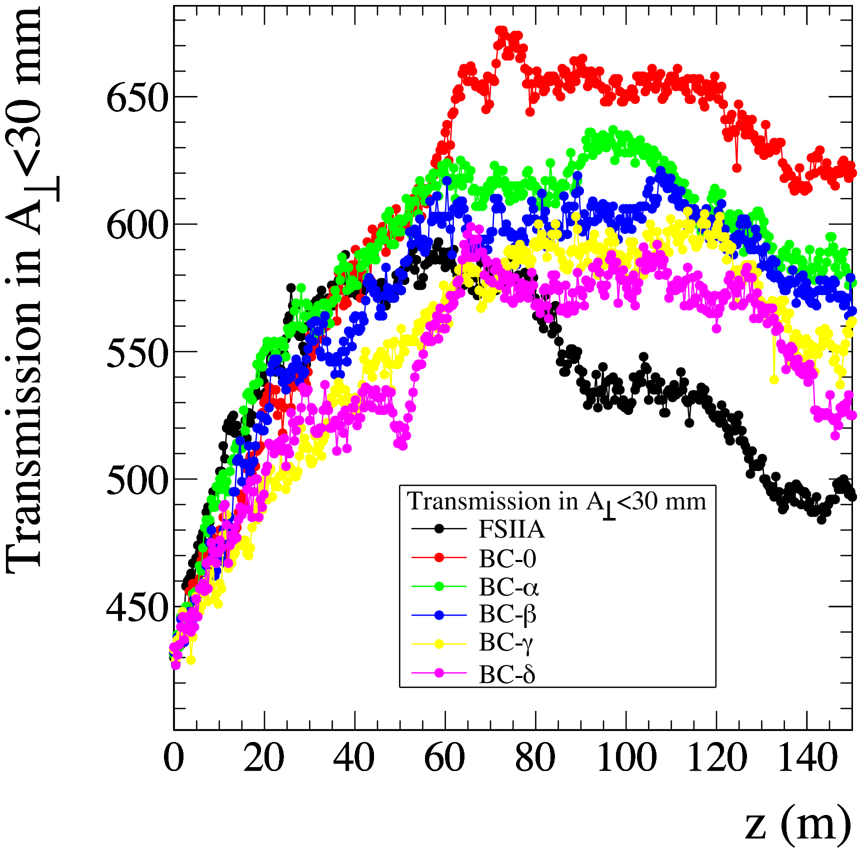

Figure 8.2.: Transmission within 30 mm of $A_{\perp}$. The effect the magnetic field reduction has in transmission is obvious. Nevertheless, the yellow and purple lines have comparable transmission and smaller magnetic field than FSIIA.

8.2. Changing BC-I Current Density

Aiming to find lattices with B_{tot} values that fall in the region between BC-I and the other BC lattices (see fig. 7.6), different current densities were applied using as base the BC-I lattice. This section shows how changes in BC-I current densities affect the magnetic field and transmission, while keeping the cell-length constant. Table 8.2 shows the current densities that were tested and their notation.

Table 8.2.: Current densities in A/mm^2 of the new BC lattices. The cell-length is equal to that of BC-I of chapter 7; the current densities are altered.

BC-	Inner Coil	Outer Coil
a	87.48	66.73
b	97.20	77.14
c	108.00	84.60
d	151.80	114.40
e	166.98	125.84
f	183.68	138.42
g	202.05	152.27

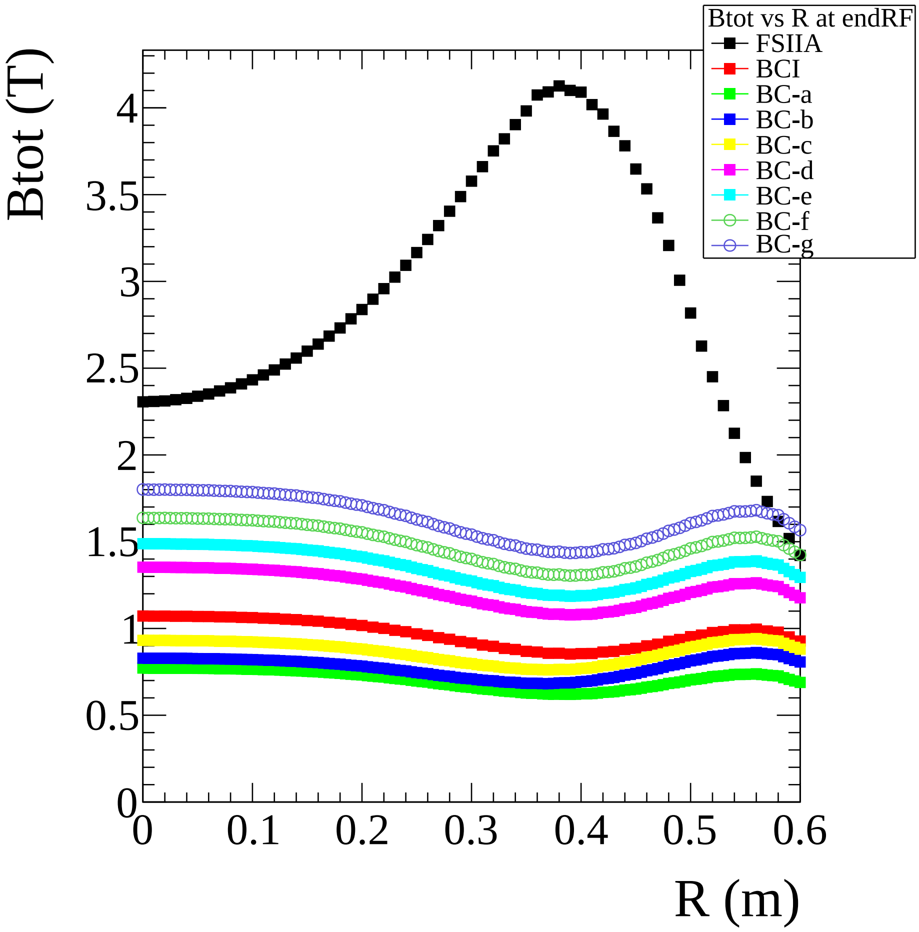

Figure 8.3.: Total magnetic field for different radii, at a fixed z. B_{tot} decreases smoothly from BC-g to BC-a.

The total magnetic field is shown in fig. 8.3. Starting from ~1.8 T (BC-g) the magnetic field decreases smoothly to less than ~0.8 T (BC-a).

What is of great interest is that transmission does not behave in a similar way to the 0.75 m cell-length, i.e. transmission does not decrease when the magnetic field decreases and vice-versa. In fig. 8.4 it can be seen that transmission actually decreases as the field increases from BC-d to -g. Nevertheless, the transmission of BC-a and -b, that achieved for than ~4-5 times smaller B_{tot} than FSIIA, achieve a comparable, or insignificantly lower transmission where FSIIA has its maximum.

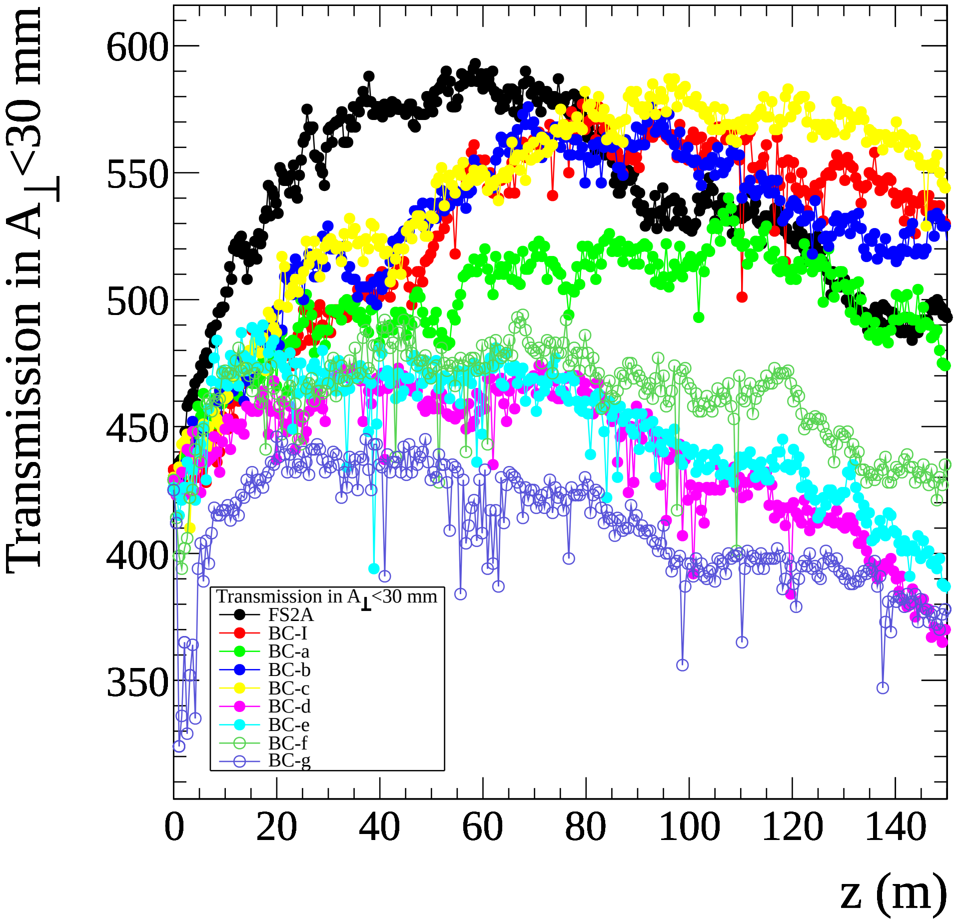

Figure 8.4.: Transmission within 30 mm of transverse acceptance cuts. Transmission increases from BC-a to -c, and then decreases from BC-d to -g. This is interesting, since instead of this behaviour, a gradual transmission increase would be expected to follow the gradually field increase from -a to -g.

The optics and tracking results of BC-a, -b, and -c can be found in appendix A.4. Although these lattices do not present as good emittance reduction as the previously seen lattices of chapter 7, they present a significantly better transmission. Hence the transmission within 30 mm of transverse acceptance of these lattices is comparable to the lattices of chapter 7.

Finally, as a summary of the two most important aspects, magnetic field reduction and transmission within 30 mm of $A_\perp$, fig. 8.5 is presented. This figure shows the maximum magnetic field at the walls of the RF cavities, with respect to the maximum achieved transmission within 30 mm of $A_\perp$, for every lattice presented in this thesis. It is clear that the majority of the Bucked Coils lattice presents a comparable, or better transmission than FSIIA, while achieving a notably lower magnetic field.

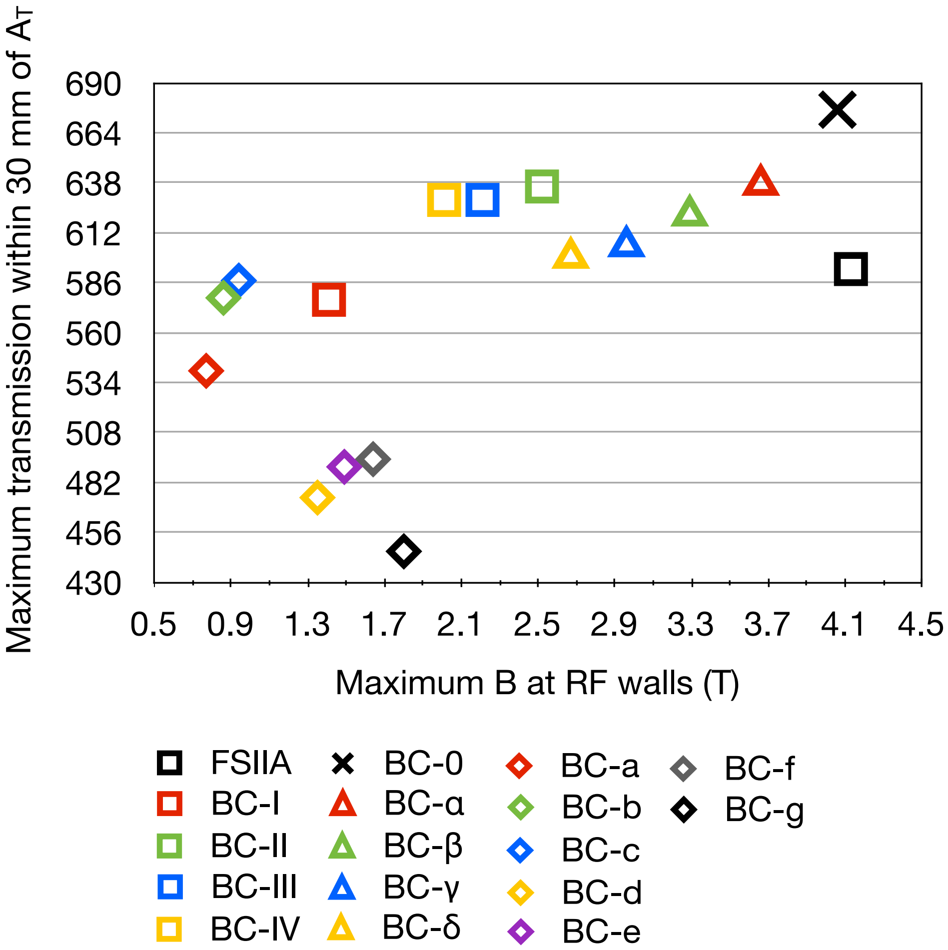

Figure 8.5.: Maximum magnetic field at the walls of the RF cavities, with respect to the maximum achieved transmission within 30 mm of $A_\perp$. The lattices presented in chapter 7 are shown in squares, those of section 8.1 are shown in triangles and black cross, and those of this section are shown in diamond shapes.

8.3. Conclusions

Different Bucked Coils lattices were created aiming to further improve the muon transmission and the magnetic field reduction at the RF positions. Initially a BC lattice with a cell-length equal to that of the FSIIA lattice (1.50 m full-cell length) was designed, but with different current densities (BC-0, -$\alpha, \beta, \gamma, \delta$). Although the magnetic field in the BC-0 lattice was slightly smaller than that of FSIIA, its transmission was ~10% larger. The other lattices presented a better magnetic field reduction and transmission equal or better than that of FSIIA.

More BC lattices were created equal in length to the BC-I lattice (2.10 full-cell length) but with different current densities (BC-a, -b, -c, -d, -e, -f, -g). BC-a was the lattice that presented the best reduction in the magnetic field (more than a factor of five smaller) while achieving a comparable transmission to the FSIIA lattice.

Chapter 9

Feasibility of Cooling Lattices

All cooling lattice design candidates require strong solenoidal magnets with large apertures. These magnets can only be constructed with superconducting technology, due to the high current densities of their coils. Still the feasibility of these magnets with respect to magnetic forces and tolerances must be analysed, taking into consideration their quench limits.

9.1. Hoop Stress

A precise knowledge and understanding of the forces acting on a magnet are of great importance, as they can limit its performance by the destruction of the coils themselves. In this subsection these forces are discussed, and the hoop stress concept is introduced together with some useful approximations for its calculation.

The Lorentz force acting on a solenoid has a radial and an axial component. The radial component, which is generated by the product of the current density, j_t, with the axial magnetic field component, B_z, is what generates the hoop stress, σ_t, in the coil. The axial component of the Lorentz force is generated by the product of the current with the radial component of the field, B_r, and results in a compressive stress, σ_z [102].

Using the “current sheet approximation”, in which the current flows in an indefinitely thin surface around the coil diameter, a simple method to approximately calculate the hoop stress in a magnet can be the following: the Lorentz force acting on a volume is given by [102]:

$$\frac{d\vec{F}}{du} = \vec{j} \times \vec{B}, \tag{9.1.1}$$

where u is the volume. When only taking into account the z-component of the field, the radial force component is given by:

$$dF_r = j_t B_z r dr dz d\phi, \tag{9.1.2}$$

(see diagram in fig. 9.1). Then, the hoop stress, σ_t, is:

$$\sigma_t = j_t B_z r. \tag{9.1.3}$$

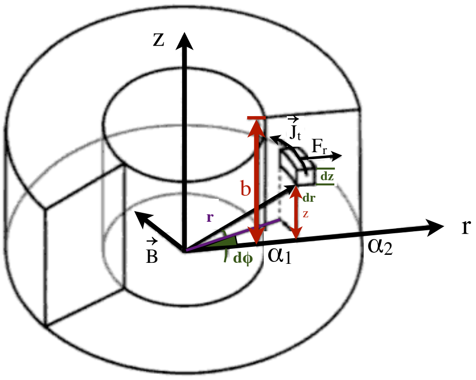

Figure 9.1.: Volume element $rdrdzd\phi$ of a solenoid with current density J_t, which generates a magnetic field $\vec{B}$ at the centre of the coil ($r = 0, z = 0$). Here, only the radial component of the Lorentz force is shown, F_r.

The typical hoop stress limit given in the up to date engineering literature for Nb-Ti SC (superconducting) coils is ~200 MPa [103]. Using equation 9.1.3, the stress acting on the coils of the FSIIA and BC lattices was estimated. This calculation was performed for the z position corresponding to the inner and outer radii of each coil[1]. Table 9.1 gives the stress at the FSIIA coils and table 9.2 the stress at the BC coils.

Table 9.1.: Hoop stress in MPa of FSIIA at 35 and 50 cm.

Lattice	**35 cm**	**50 cm**
FSIIA	238.9	232.0

---

[1] These points were selected after verifying they are the two points with the highest hoop stress.

Table 9.2.: Hoop stress in MPa of different BC lattice versions at 30, 45, 60 and 75 cm.

Lattice	**30 cm**	**45 cm**	**60 cm**	**75 cm**
BC-I	260.6	334.8	345.3	176.0
BC-II	288.2	403.4	521.1	279.2
BC-III	316.8	398.0	416.9	215.9
BC-IV	196.3	248.3	304.0	156.0
BC-0	263.5	326.2	378.8	182.7
BC-α	213.8	262.4	272.9	146.2
BC-β	172.0	214.3	223.7	120.6
BC-γ	139.1	173.2	180.0	98.7
BC-δ	113.4	141.7	145.6	75.5
BC-a	139.1	177.1	188.2	124.6
BC-b	169.1	223.1	249.9	130.2
BC-c	209.0	272.2	382.3	202.5
BC-d	419.0	544.7	556.0	283.1
BC-e	505.9	646.2	672.0	349.2
BC-f	610.8	777.0	812.3	419.4
BC-g	739.5	945.6	977.5	666.7

From tables 9.1 and 9.2 it can be easily seen that most of the lattices, including FSIIA, well exceed the hoop stress limit of 200 MPa. Although this limit is considered to be conservative, there are three lattices, BC-γ, -δ and -a, with hoop stress values close or lower than 200 MPa (the hoop stress of BC-γ is slightly larger 200 MPa, however this excess is considered to be negligible). Note that BC-IV, as described in section 7.1, was designed to achieve a lower hoop stress than BC-I, -II, and -III, something that is verified here.

It must be emphasised that the simplified estimation used here is for comparison reasons only, and must be followed by some rigorous mechanical design studies.

9.2. Critical Surface

The critical behaviour of a superconductor can be described in a 3D space, in terms of a critical surface (see fig. 9.2). This surface is formed by the applied magnetic field, B_{app}, transport current, J_{tr}, and temperature, T. The critical surface means that at a particular temperature, T, there is a specific critical field, $B_c(T)$, which will transform the superconductor to a normal conductor if applied in the absence of transport current. In a similar way, there is also a critical current density, $J_c(T)$, that will transform the superconductor to a normal conductor if applied at zero magnetic field. In addition, in the presence of an applied field, a smaller transport current than J_c will also drive the superconductor normal. Similarly if a transport current is already passing through a superconductor, an applied magnetic field smaller than B_c will also drive it to the normal conducting state (the quench effect) [104].

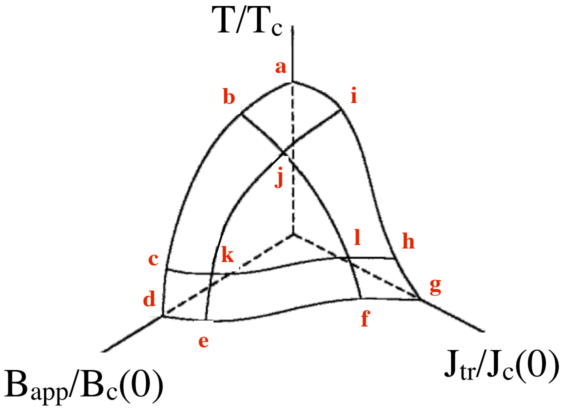

Figure 9.2.: The critical surface of a superconductor. The curve d-c-b-a is drawn for transport current $J_{tr} = 0$, g-h-i-a is drawn for applied magnetic field $B_{app} = 0$, and d-e-f-g for temperature $T = 0$. Values of B_{app}, J_{tr} and T below and above the critical surface are in the superconducting and normal region respectively. Figure taken and edited from [104].

Several practical critical surface fits have been produced in the literature, however they are often tailored to restricted ranges of the magnetic field and temperature, or are defined as complex piecewise polynomial fits.

A self-consistent fit formula providing the critical current density as a function of temperature and field for Nb-Ti is given in [105]. Despite the simplicity of this formula, the approach followed has a good engineering value.

In [105], the reduced temperature t and the reduced field b are introduced and defined as:

$$t = \frac{T}{T_{c0}}, \tag{9.2.1}$$

and

$$b = \frac{B}{B_{c2(T)}}, \tag{9.2.2}$$

where T_{c0} is the maximum critical temperature (at B=0), $B_{c2} = B_{c20}(1 - t^n)$, is the upper critical field, and B_{c20} is the maximum upper critical field (at T=0).

The function chosen for the fit of the critical surface as a function of the reduced parameters t and b is:

$$J_c = \frac{C_0}{B} b^a (1-b)^\beta (1-t^n)^\gamma, \tag{9.2.3}$$

where C_0 is a normalisation constant, α, β describe the dependence on b, and γ describes the dependence on t. In [106] a suitable critical field dependance on temperature is given:

$$B_{c2} = B_{c20}(1-t^n), \tag{9.2.4}$$

where $n = 1.7$ provides a satisfactory fit to most alloy compositions. From this equation it can be derived that for Nb-Ti:

$$J_c = C(T) B^{\alpha-1} \left(1 - \frac{B}{B_{c2}(T)}\right)^\beta, \tag{9.2.5}$$

where C is temperature dependent [107].

This complex parameter dependence can be very approximated to

$$J_c = c(b-B),\ B < b, \tag{9.2.6}$$

where b∼10 T at 4.2 K and 13 T at 1.9 K. The slope $c \sim 6 \times 10^8$ A/(Tm^2) is independent of the temperature. Figure 9.3 shows the critical surface for Nb-Ti for 1.9 and 4.2 K and the maximum total magnetic field with respect to the current density of the FSIIA and BC lattices. As can be seen, the majority of the lattices are within superconducting limits; however, BC-e, -f, and -g exceed it (BC-d is at the border). For a stable operation, these points should be well outside the critical surface, allowing for sufficient margins.

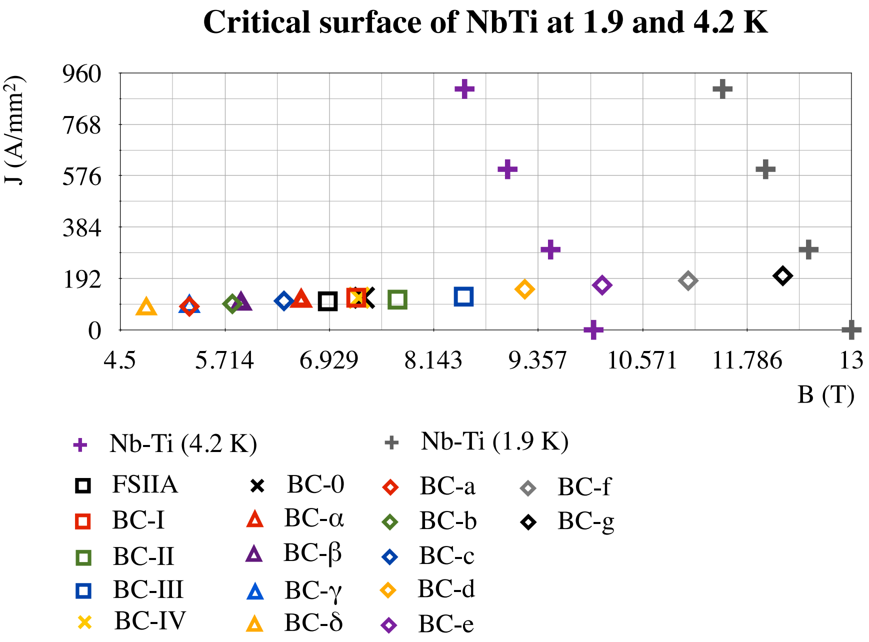

Figure 9.3.: Critical surface of Nb-Ti, and the maximum magnetic field at coils for FSIIA and the BC lattices with respect to the current density. The critical surface is shown in grey crosses for 1.9 K and in purple crosses for 4.2 K. The current density with respect to the maximum B_{tot} is plotted in squarers for FSIIA (black), BC-I, -II, -III, and -IV (red, green, blue and yellow respectively). Note that BC-IV is shown in yellow "X"-symbol rather than square as its coordinates are very similar to those of BC-I. BC-a to -g are shown in diamond shapes, BC-α to -δ are shown in triangles and BC-0 in black "X"-symbol. Only lattices BC-e, -f, and -g are not within the superconductive limits (BC-d is at the border).

9.3. Conclusions

The FSIIA and different versions of BC lattices were compared on their feasibility in superconducting design with respect to the hoop stress acting on their coils and their quench limits.

The hoop stress was calculated for different radii, and the maximum hoop stress of each lattice are listed in tables 9.1 and 9.2. The only lattices found within the ~200 MPa stress limit were BC-γ, -δ and BC-a.

The critical surfaces of Nb-Ti were plotted for two different temperatures, and the maximum magnetic fields of FSIIA and all BC lattices were plotted against their current densities[2]. The majority of the lattices were within the

---

[2] In the case of the BC lattices, the current density chosen for this plot was that of the specific coil that corresponded to B_{max}.

limits for superconducting operation; however BC-e, -f, and -g exceeded it (BC-d is at the border, see fig. 9.3).

Based on the results of the magnetic field reduction, the transmission, the hoop stress value and the quench limit, it can be concluded that the best lattices overall are BC-a and BC-b. These lattices were found to achieve a more than five times lower magnetic field and a comparable, or insignificantly lower, transmission compared to FSIIA (see figures 8.3 and 8.4). In addition, BC-a is well within the conservative 200 MPa hoop stress limit, whereas BC-b slightly exceeds it. Finally, both lattices are within the limits of superconducting operation. A future analysis aiming to further optimise these two BC lattices would therefore be very fruitful.

Chapter 10

Muon Collider and 6D cooling

A lepton collider, with sufficient energy and luminosity, would enable a further investigation of the mechanism responsible for the mass generation (if discovered at the Large Hadron Collider, LHC) and the origin of the electroweak symmetry breaking. Moreover, such a collider would facilitate the search for supersymmetric particles and the confirmation of their nature (if discovered), while also would search for signs of extra space-time dimensions and quantum gravity [85].

10.1. Muon Collider

It is expected that the results obtained from CERN's LHC by ∼2013, will set the desired energy for the next lepton collider and refine our current knowledge of the required luminosity. At present, there are three alternatives for a multi-TeV collider: a) a $\mu^+\mu^-$ collider (MC), b) a normal-conducting RF e^+e^- linear accelerator, and c) a SC (superconducting) collider. Due to the negligible synchrotron radiation muons emit, a MC promises superior attributes in a number of areas in comparison to either e^+e^- scheme: the absence of synchrotron radiation allows high-energy muon bunches to be stored in a compact collider ring, and therefore a MC would fit conveniently on the site of an existing laboratory. In addition, since the radiation of particles, caused by the collisions inside the muon bunches (beamstrahlung) is orders of magnitude lower than that of electron collisions, the muon collisions would be more monochromatic [85].

In order for the desired luminosity of $\mathscr{L} \sim 10^{30} - 10^{34}$ cm^{-2}s^{-1} to be achieved, a MC requires substantial muon cooling. Therefore, a six-dimensional phase-space volume reduction by a factor of $\sim 10^6$ is essential, which implies a requirement for transverse as well as longitudinal cooling. Since a 10^{21}-decays/year Neutrino Factory and a 10^{34}-luminosity Muon Collider can be driven by a 4 MW proton beam, these two facilities can have an almost identical proton driver and high-power target systems. A Muon Collider can be considered as an upgrade path of the Neutrino Factory, and therefore their front-ends are very similar [108].

Since a Muon Collider and a Neutrino Factory require both similar front ends, much of their associated R&D is in common [85]. A layout of the Neutrino Factory and Muon Collider is shown in fig. 10.1.

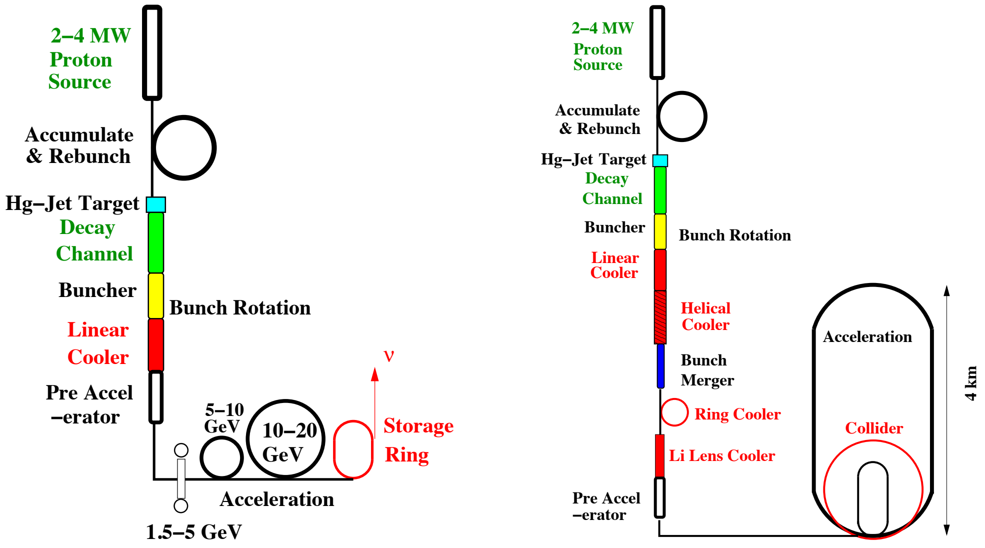

Figure 10.1.: Layout of a Neutrino Factory (left) and a Muon Collider (right). The similarity of their front-ends, consisting of a high-power proton driver and target, pion decay channel, bunching, phase rotation, and a transverse cooling channel, explains their common R&D. Figure taken from [85].

10.2. The "Snake" 6D Cooling Lattice.

This section presents the "Snake" lattice, a *novel* cooling lattice designed to achieve a six-dimensional emittance cooling. Using the FSIIA lattice as a starting point, Snake aims to be a solution for a Neutrino Factory upgradable to a Muon Collider.

10.2.1. Methodology

Aiming to simplify the cell geometry and the RF cavities installation, the Snake lattice introduces dispersion with the use of straight dipoles, rather than tilted solenoids [109]. However this method comes with the price of additional coil windings, needed to generate the dipole field component. The correlation between energy loss and position in the Snake lattice is introduced with wedge absorbers.

10.2.2. Magnetic Field

The solenoids and dipoles were placed at the same positions along the beam-axis, and were repeated every 0.75 m with an alternation of their polarity; a full-cell was therefore 1.5 m long. It should be noted that an appropriate care was taken so that the solenoidal and dipole fields had their maxima at the same positions along the beam-axis, z. Moreover, the dipole field characteristics were chosen such as the dipole field's change with z would be smooth, in order to avoid high field gradients that could cause an important decrease in transmission. The solenoidal and dipole fields are shown in fig. 10.2.

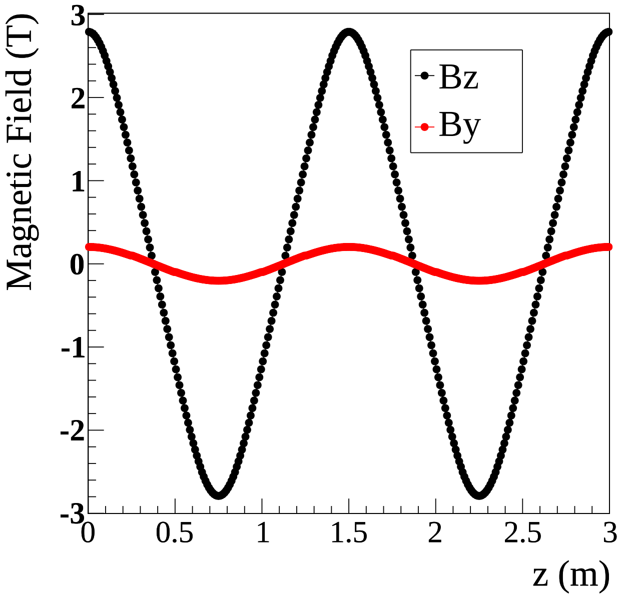

Figure 10.2.: On-axis magnetic field of solenoids (B_z) and dipoles (B_y) along the beam-axis.

10.2.3. Closed Orbit

The closed orbit was found numerically for different momenta, using the Simulation application of G4MICE and a user-written script: for a specific momentum, one particle was input at zero magnetic field at the middle of a lattice that only included twenty dipoles, twenty solenoids and two detectors, so that the particle will be within a symmetric magnetic field configuration. The first detector was placed at the location where the particle was input, and the second detector 1.5 m downstream (i.e. at the end of a full-cell length). After running the Simulation application of G4MICE, the script was calculating the momentum and position difference between the final and initial location of the particle:

$$\begin{aligned}
\Delta P_x &= P_{x,fin} - P_{x,in}, \\
\Delta P_y &= P_{y,fin} - P_{y,in}, \\
\Delta P_z &= P_{z,fin} - P_{z,in}, \\
\Delta x &= x_{fin} - x_{in}, \\
\Delta y &= y_{fin} - y_{in}, \\
\Delta z &= z_{fin} - z_{in}. \qquad (10.2.1)
\end{aligned}$$

If the absolute values of all the momentum and position differences were smaller or equal to 1 MeV/c and 1 mm (which were consider small values), then the approximate closed orbit was said to be found at the position and momentum values used as input. If the absolute values were larger than 1 MeV/c and 1 mm respectively, then ensuring the total momentum remained constant (by using $P_{tot} = \sqrt{P_x^2 + P_y^2 + P_z^2} = constant$), the particle was re-input having as new initial components:

$$\begin{aligned}
P_{x,new} &= \frac{(P_{x,fin} + P_{x,in})}{2}, \\
P_{y,new} &= \frac{(P_{y,fin} + P_{y,in})}{2}, \\
P_{z,new} &= \frac{(P_{z,fin} + P_{z,in})}{2}, \\
x_{new} &= \frac{(x_{fin} + x_{in})}{2}, \\
y_{new} &= \frac{(y_{fin} + y_{in})}{2}, \\
z_{new} &= \frac{(z_{fin} + z_{in})}{2}. \qquad (10.2.2)
\end{aligned}$$

Table 10.1.: Closed orbit parameters for different momenta. Positions x, y, z are in m, momenta P_x, P_y, P_z in GeV/c, and Energy, E, in GeV.

P	**x**	**y**	**z**	$\mathbf{P_x}$	$\mathbf{P_y}$	$\mathbf{P_z}$	**E**
232	$\mathcal{O}(10^{-3})$	$\mathcal{O}(10^{-3})$	0.0	0.0151	0.0049	0.231	0.254
+20%	$\mathcal{O}(10^{-3})$	$\mathcal{O}(10^{-3})$	0.0	0.0148	0.0039	0.278	0.297
-20%	$\mathcal{O}(10^{-3})$	$\mathcal{O}(10^{-3})$	0.0	0.0157	0.0066	0.1848	0.213
+10%	$\mathcal{O}(10^{-3})$	$\mathcal{O}(10^{-3})$	0.0	0.0150	0.0043	0.2547	0.276
-10%	$\mathcal{O}(10^{-3})$	$\mathcal{O}(10^{-3})$	0.0	0.0153	0.0056	0.2081	0.233
+5%	$\mathcal{O}(10^{-3})$	$\mathcal{O}(10^{-3})$	0.0	0.0150	0.0046	0.2431	0.265
-5%	$\mathcal{O}(10^{-3})$	$\mathcal{O}(10^{-3})$	0.0	0.0152	0.0052	0.2198	0.244

This procedure was repeated until the closed orbit was found. The initial position and momentum that resulted in a closed orbit of seven different momenta (232, $232 \pm 20\%, 232 \pm 10\%$, and $232 \pm 5\%$) are listed in table 10.1, and their $x-$ and $y-$orbits are illustrated in fig. 10.3.

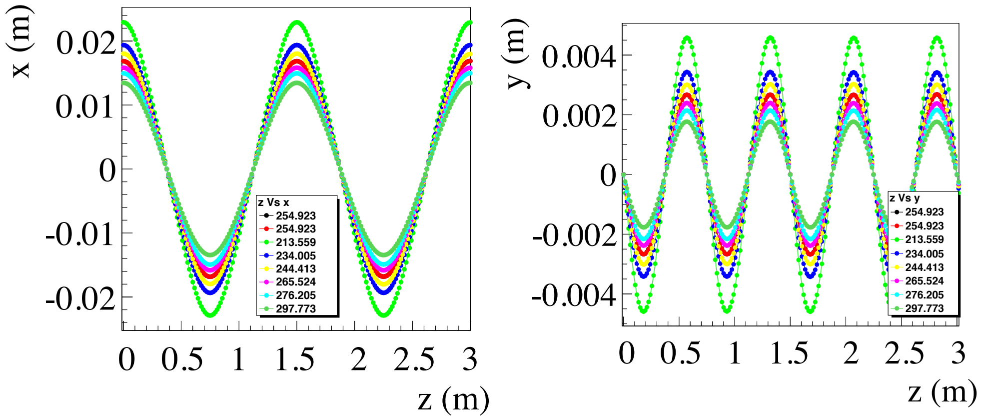

(a) $x-$orbit

(b) $y-$orbit

Figure 10.3.: Closed orbits for different particle energies. Note that the lower energy particles follow an orbit with larger extends in both positive and negative directions, for both x and y, than the higher energy particles. The colour code of each plot shows the total energy value (in MeV) of the specific particle.

10.2.4. Dispersion Calculation

In order to find the dispersion in the lattice, only solenoids and dipoles were included in the tracking calculation. The closed orbit of a particle differing by +1% from the reference momentum[1] of 232 MeV/c (i.e. the particle's

---

[1] Or momentum of the synchronous particle.

momentum was 234.32 MeV/c), was found. The closed orbit values were used as input and the particle was tracked through ten cells. The difference between this particle and the reference one in x and y position along the lattice was then calculated, and used for the dispersion calculation, D_x, and D_y:

$$\begin{aligned} D_x &= \frac{\Delta x}{\Delta P/P_o} \\ D_y &= \frac{\Delta y}{\Delta P/P_o}, \end{aligned} \tag{10.2.3}$$

where Δx is the difference in $x-$position between the particle and the reference particle: $\Delta x = x_p - x_o$, and ΔP is the difference in momentum: $\Delta P = P_p - P_o$ (in this case P_o=232 MeV/c, and $\Delta P/P_o$=0.01). D_x and D_y are shown in fig. 10.4. Due to the fact that $D_x > D_y$, the wedge absorbers' orientation was chosen such as to affect the x, rather than the y position of the particles. Comparing this plot with fig. 10.3 it can be seen that D_x and D_y have negative values for positive x, y, which implies that lower energy particles will follow larger x and y orbits than the higher energy particles. This is verified in figures 10.3a and 10.3b.

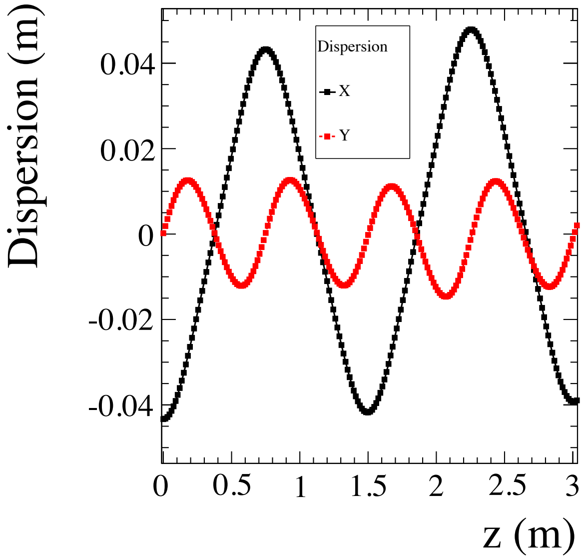

Figure 10.4.: Dispersion in x (black) and y (red). Due to the fact that the dispersion in the x-direction is larger than in the y-direction, the wedge absorbers' orientation will be such as to affect the x-orbit of the particles.

10.2.5. Transverse Dynamics

In order to understand the transverse beam dynamics in the Snake lattice, the transfer matrix **M** was calculated. Initially a small perturbation was added to the closed orbit (CO) value of x, obtaining x_{new}. A particle with initial parameters x_{new}, x'_{CO}, y_{CO}, y'_{CO} was then tracked through one full-cell and the output values of x, x', y, y' were recorded. After subtracting the closed orbit from these output values and dividing with the initial perturbation, the first column of the transfer matrix 10.2.4 was formed. The same procedure was followed for x', y, y' and the entire matrix was reproduced.

$$\begin{pmatrix} 0.3518 & 1.30839 & 0.00436 & 0.00218915 \\ 0.686822 & 0.371697 & 0.0127572 & 0.0155374 \\ 0.0047 & 0.00586846 & 0.354 & 1.26407 \\ 0.0108023 & 0.00770137 & 0.699924 & 0.362696 \end{pmatrix} \tag{10.2.4}$$

Transfer matrix **M** shows a symmetry between its two diagonal elements, and this symmetry is illustrated in matrix 10.2.5. The diagonal elements α are very similar, whereas the off-diagonal elements β are much smaller than α and close to 0. This implies that the dipole field has a small effect on the transfer matrix. Subsequently it is inferred that there is no need to re-match the betatron function to the Snake lattice and the same $\beta_{\perp}$ can be used as the one in FSIIA.

$$\begin{pmatrix} \alpha & \beta \\ \beta & \alpha \end{pmatrix} \tag{10.2.5}$$

10.2.6. Lattice Layout

A half Snake cell consists of a solenoid, a dipole and a wedge absorber, placed at the start of the cell, and an RF cavity located at the middle of the half-cell. The solenoid’s and dipole’s polarities, together with the wedge’s orientation, alternate with every half-cell repeat. A full 1.5 m Snake cell is illustrated in fig. 10.5. Note that this is a simplified illustration of the lattice.

The orientation of the absorbers was chosen based on the $x-$orbit of the beam shown in fig. 10.3a. The more energetic particles follow a smaller $x-$orbit than the less energetic ones, and the first $x-$orbit maximum has a positive value. Therefore, the absorbers needed to be shifted in the $x-$direction, as illustrated in fig. 10.7. The amount of shifting was chosen to be the one that keeps the energy of the reference particle constant. Note that due to the absorber orientation illustrated in this layout, the less energetic particles will indeed pass through less absorber material than the more energetic ones. The alternation in the absorber's orientation is also compatible with the the $x-$oscillations of fig. 10.3a. Fig. 10.7 illustrates the x-orbits together with the Snake components.

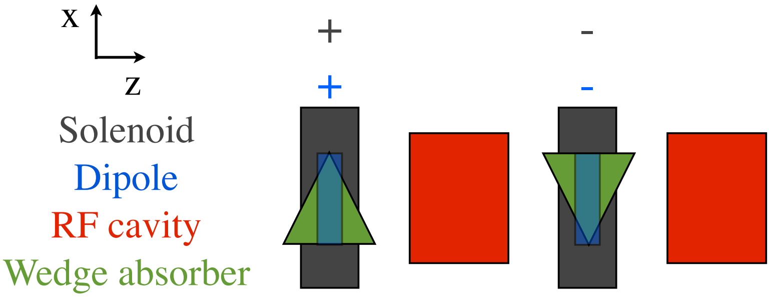

Figure 10.5.: A full-cell of the Snake configuration. A solenoid (grey), dipole (blue), and wedge absorber (green) are placed at the start of the cell, and are repeated after 0.75 m. An RF cavity (red) is placed at the middle of each half-cell, and the polarity of the solenoids and dipoles, together with the absorber's orientation, alternate with every half-cell repeat.

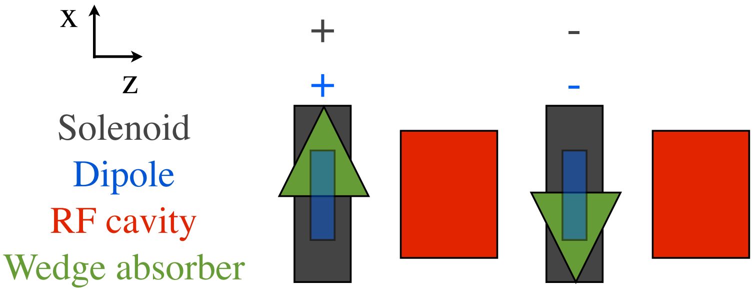

Figure 10.6.: A full-cell of the Snake configuration. The wedge absorbers are shifted in the $x-$direction to be compatible with the $x-$orbit of the beam.

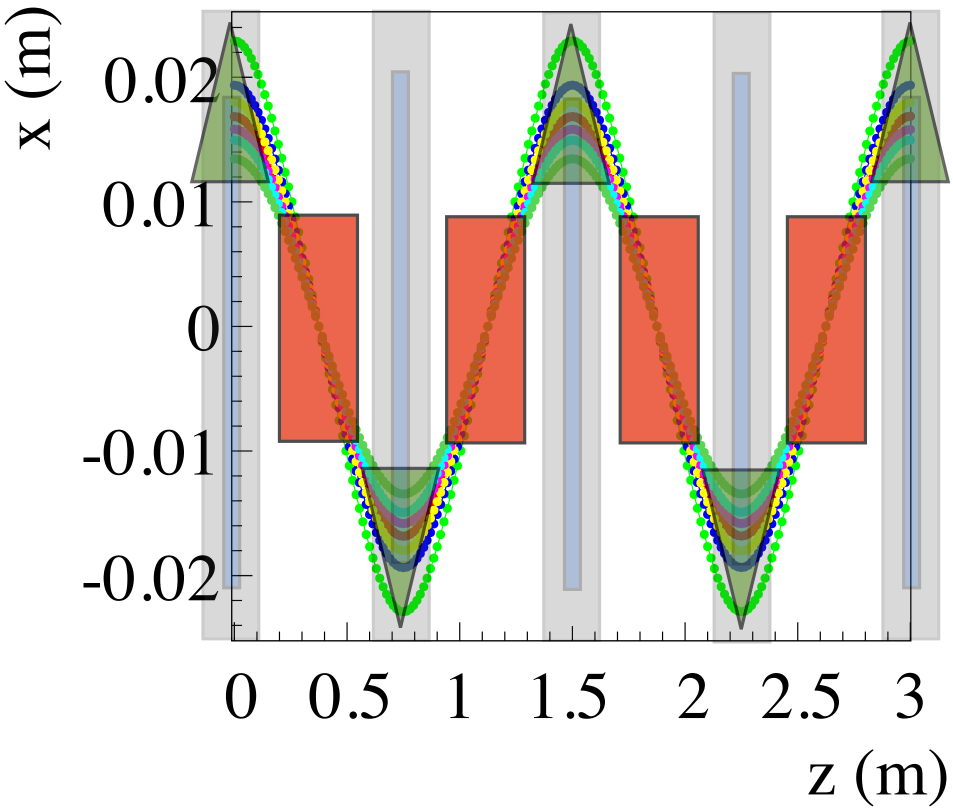

Figure 10.7.: The x-orbits are plotted together with the Snake components to emphasise the importance of shifting in x-direction. The less energetic particles follow a larger orbit and pass through smaller absorber material, due to the absorbers' orientation.

10.2.7. Tracking

Initial tracking in G4MICE did not produce a satisfactory result when all the components (wedge absorbers, coils and RF cavities) have been taken into account. The energy and time difference between the reference and a non-reference particle was plotted. The non-reference particle was input with the same position and momentum components as the reference one, and with a 0.12 ns initial time difference. The motion in fig. 10.8 suggested problems with the RF phasing adjustment.

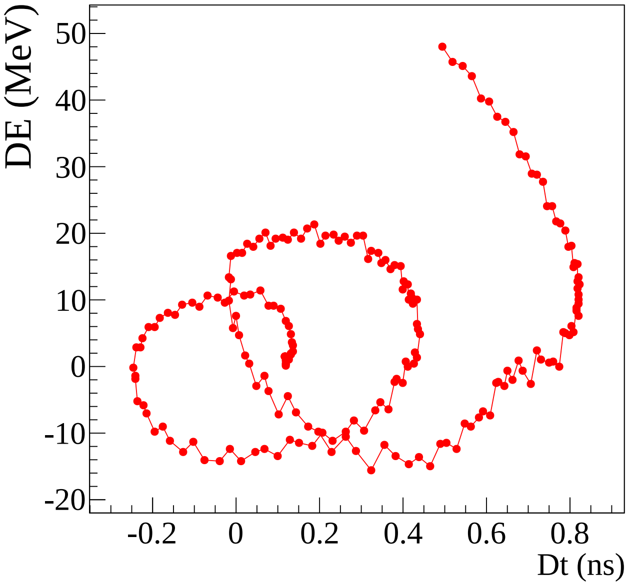

Figure 10.8.: Energy and time difference between the reference and a non-reference particle, with the same initial position and momentum values as the reference. The initial time difference was Δt=0.12 ns. The outward spiralling implied a problem with the RF phasing.

Alternative study was conducted in order to investigate the performance of the Snake lattice using the Beam Optics code [110]. This study used the magnetic field generated in G4MICE and an appropriate model of wedge absorbers. This absorber model involved the Bethe-Bloche energy loss and multiple scattering, but did not take into account the straggling effect. The 15 degrees wedge absorber orientation was as discussed above, however their location was as in FSIIA, i.e. on each side of the RF cavities.

First a reference particle was tracked and the absorber thickness was adjusted such as the initial and final energy of the particle would be the same in ±1 MeV accuracy. Following this, 1000 particles were created having identical initial parameters to the reference particle. These particles were then tracked through the lattice, and their final mean energy, $\bar{E}$, was calculated. The length of the wedge absorbers was altered to assure the same mean energy at the beginning and at the end of the lattice for the mean energy of the bunch. Finally, the energy loss of the reference particle and the phasing of the RF cavities were manipulated such as the final energy of the reference particle would be the same as the mean energy of the bunch ($E_{o,final} = E_{o,initial} = \bar{E}$).

In order to check the validity of this method, the energy difference between a particle and the reference one was plotted against their time difference (the non-reference particle had a 0.4 ns time difference from the reference particle;

all other parameters were the same as those of the reference particle). Figure 10.9 shows an inwards spiralling of the energy and time, demonstrating a decrease of the longitudinal parameters. It is clearly shown that longitudinal cooling can be achieved when the phasing of the cavities is correctly adjusted.

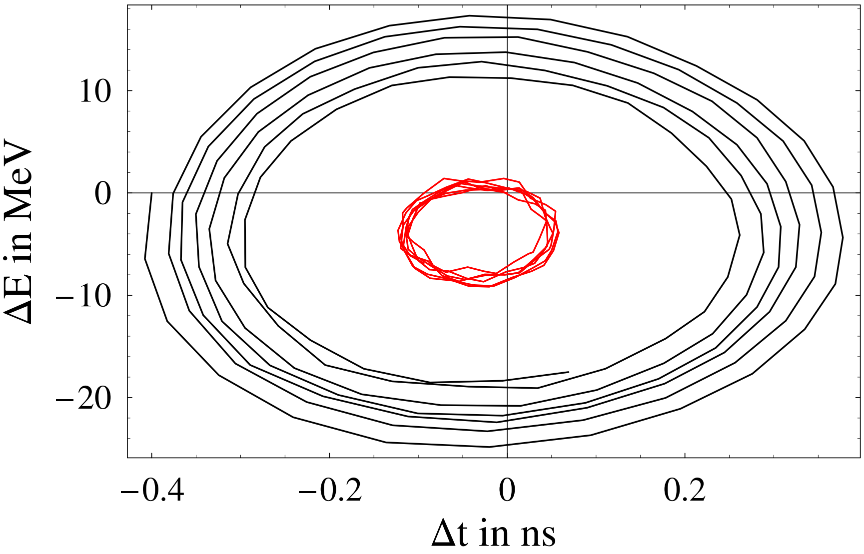

Figure 10.9.: Energy and time difference between the reference particle and a non-reference particle, with identical initial position and momentum values as the reference. The black line shows the result for an initial time difference of 0.4 ns between the reference and the non-reference particle, and the red line shows the results when no time difference was set. The red line indicates that the phasing is not exactly precise; however, the inward spiralling of the black line demonstrates that the new phasing option of the cavities is sufficient [111].

A similar approach to improve the RF phase adjustment was followed using the G4MICE software, where 0.12 ns rather than 0.4 ns was chosen as the initial time difference between the reference and the non-reference particles. Absorbers of 15° were placed as in fig. 10.7. The result of the energy and time difference between the reference and the non-reference particle is shown in fig. 10.10. It should be highlighted that the multiple Coulomb scattering option was disabled, together with the straggling effect, and that inward spiralling could not be achieved for initial time difference larger than 0.2 ns.

It is also believed that the phasing of the RF cavities in G4MICE could alternatively be further improved using the option “Phased” rather than “Unphased” for the cavity mode and an appropriate time delay[2]. Due to time

---

[2] In G4MICE this can be done with: “PropertyString CavityMode Phased” and “PropertyDouble TimeDelay”, with the appropriate time given in ns.

constraints the TimeDelay option was not explored.

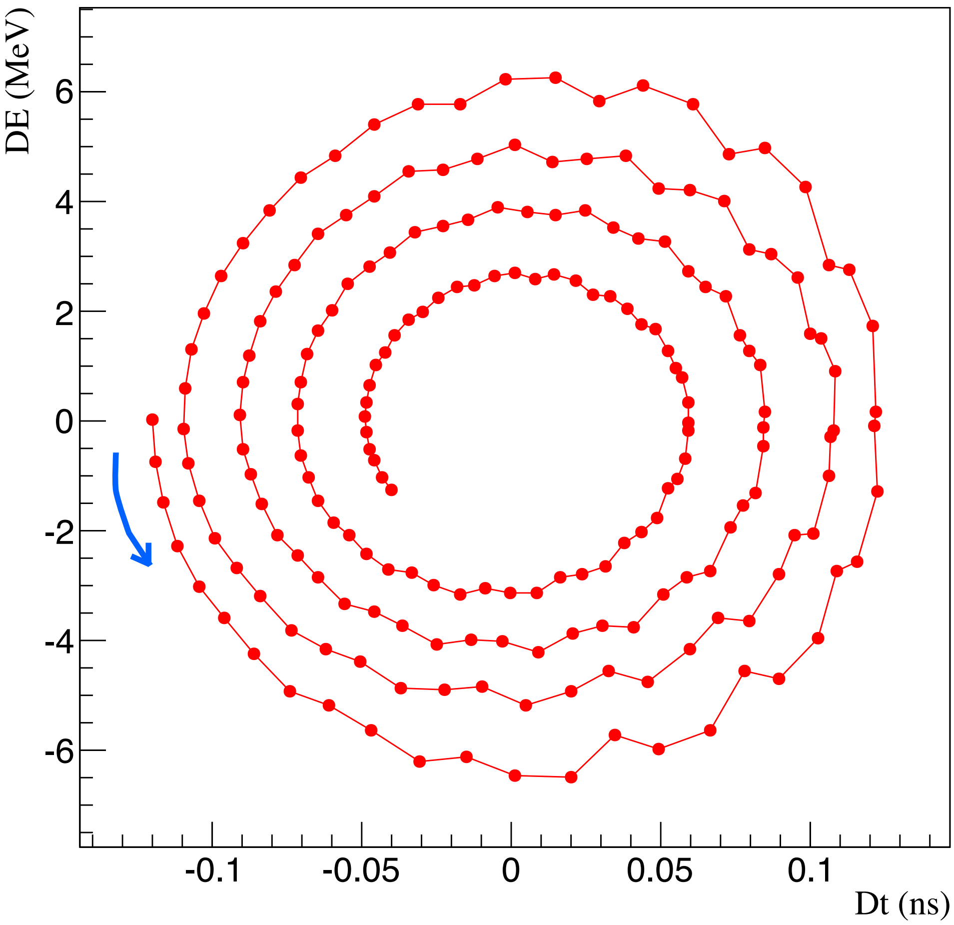

Figure 10.10.: Energy and time difference between the reference particle and a non-reference particle, with identical initial position and momentum values as the reference. There was an initial time difference of 0.12 ns between the reference and the non-reference particle.

10.2.8. The Snake-PMMP Lattice

Another lattice, Snake-PMMP, was designed with a different dipole polarity distribution (plus-minus-minus-plus, rather than plus-minus-plus-minus that was used in Snake), obtaining a similar B_y amplitude to that of Snake (see fig. 10.11a). After finding the closed orbits between a reference particle with momentum of 232 MeV/c and a non-reference particle with momentum $P = 232 + 232 \cdot 1\%$ MeV/c, and following the same procedure as in section 10.2.4, the dispersion of Snake-PMMP was found. Comparing the dispersion obtained in Snake-PMMP to that of Snake (see figures 10.11b and 10.4) it is clear that Snake-PMMP achieves a significantly higher dispersion, implying this lattice could offer stronger longitudinal cooling, or could allow to generate a sufficiently large dispersion using smaller dipole field components. Snake-PMMP has not been further analysed due to time constraints. However, this finding is promising and is therefore believed that further investigation of this lattice would be fruitful.

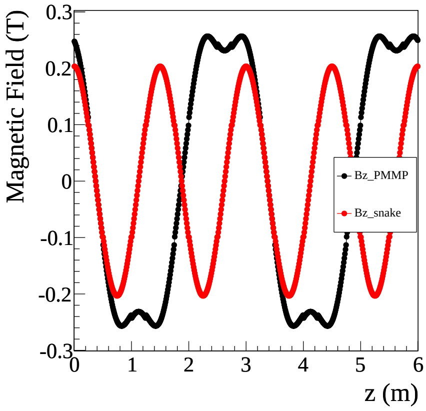

(a) B_y field comparison between Snake-PMMP (black) and Snake (red).

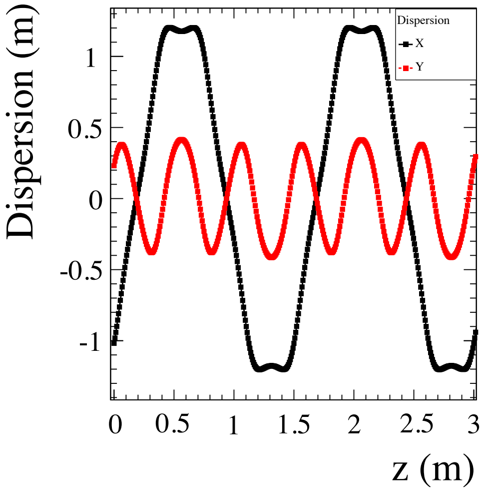

(b) Dispersion (D_x in black and D_y in red) in mm for Snake-PMMP along a 6 m lattice.

Figure 10.11.: (a) B_y comparison between Snake and Snake-PMMP; the two magnetic fields are comparable in amplitude, and the different geometry results in a different B_y behaviour. (b) Dispersion in Snake-PMMP; both D_x and D_y are significantly increased in this geometry in comparison to the dispersion obtained in the Snake lattice.

10.3. Conclusions

A new lattice was designed aiming to achieve a 6D emittance cooling of a muon beam, applicable for use at the Neutrino Factory and Muon Collider. This lattice, named Snake, introduced dispersion with the use of dipoles, and a correlation between energy loss and position with the use of wedge absorbers. The wedge absorbers were placed in such a way that the reference particle's energy would remain constant and that the less energetic particles would pass through less material than the more energetic ones.

After the realisation that the longitudinal phase space of the muon beam was not behaving as expected, the phase of the RF cavities was altered, using a specific technique and a different software than G4MICE (described in section 10.2.7). This new technique demonstrated that this lattice can achieve longitudinal cooling.

A similar approach was followed using the G4MICE result, resulting in the same indication of longitudinal cooling. Suggested procedure that could alternatively be used in G4MICE is given in section 10.2.7.

In addition it was shown that a change in the distribution of the dipole polarity can significantly increase the dispersion in both x and y without increasing the magnetic field. Due to time constraints this new geometry (Snake-PMMP) has not been further analysed. It is strongly encouraged that both Snake and Snake-PMMP should be further explored in the future as the results presented in this thesis are very promising.

Chapter 11

Conclusions

The future accelerator complex of the Neutrino Factory will enable the neutrino oscillation parameters measurement in an unprecedented precision. In particular this facility aims to address the evidence of the CP violation in the leptonic sector. The neutrinos at the Neutrino Factory will be produced from the decays of muons that are accumulated in storage rings. However, the muons are produced as tertiary particles, and as such occupy a large transverse phase-space. Therefore, in order to further accelerate the muon beam effectively before the muons decay, the beam emittance needs to decrease using ionisation cooling.

The reference ionisation cooling lattice of the Neutrino Factory, FSIIA (Feasibility Study IIA), performs well with respect to muon transmission and cooling dynamics. However, recent studies indicate that external magnetic field at the position of the RF cavities can reduce the cavities' performance and lead to RF breakdown. Since FSIIA has a high magnetic field at the RF cavities, the feasibility of this lattice has come under question.

This thesis presented several new lattices studied using the G4MICE software, aiming to achieve a low magnetic field at the position of the RF cavities, whilst achieving muon transmission and cooling dynamics comparable to that of FSIIA. Among these lattices, a *novel* lattice, called the "Bucked Coils" has shown a particularly good performance. Bucked Coils uses two coils of opposite polarity, placed at the same position, rather than just one that FSIIA uses. A detailed comparison between the FSIIA and the Bucked Coils lattices was given, with respect to the magnetic field, cooling dynamics and transmission.

Initially, four different versions of Bucked Coils (BC-I, -II, -III, and -IV) with larger cell-lengths than FSIIA were presented. BC-I achieved almost five times smaller magnetic field than that of FSIIA at the walls of the RF cavities, and a comparable transmission to FSIIA. The other three lattices achieved 2.5

times smaller magnetic field than FSIIA, and a higher transmission. A realistic beam was also used, with the same characteristics of the muon beam exiting the Front-End of the Neutrino Factory; the tracking results were comparable to those where a non-realistic beam was used.

More Bucked Coils versions were designed with a smaller cell-length, equal to that of FSIIA (1.5 m full cell-length), and different current densities (BC-0, α, -β, -γ, -δ). All these versions, achieved smaller magnetic field than that of FSIIA, and a higher or equal transmission. Other Bucked Coils lattices were also considered, with a cell-length equal to that of BC-I (2.10 m full-cell length), but different current densities (BC-a, -b, -c, -d, -e, -f, -g). The magnetic field of these lattices has been significantly lower than that of FSIIA (up to more than ∼5 times). The transmission performance of BC-a, -b, -c was comparable or insignificantly lower than that of FSIIA, whereas the other lattices had a notably lower transmission.

Most importantly, the feasibility of all the Bucked Coils lattices was compared to that of FSIIA with respect to the hoop stress that the coils experience, and their quench limits for superconducting design based on Nb-Ti. It was found that the only lattices within the ∼200 MPa limit of hoop stress are BC-γ, -δ, and -a. All other lattices, including FSIIA, exceed this limit. The critical surface of Nb-Ti was plotted for two operation points at 1.9 and 4.2 K, and the current density of all the lattices was plotted against their maximum magnetic field. It was shown that almost all lattices are within the limits of superconductivity, apart from BC-e, -f, and -g. Further study is needed including a more realistic approach on the mechanical engineering design.

The best lattices with respect to the magnetic field reduction, transmission and feasibility study are considered to be BC-a and -b: these lattices achieved more than five times smaller magnetic field at the position of the RF cavities and a comparable, or insignificantly lower transmission compared to FSIIA. In addition, BC-a is well below the 200 MPa limit and the critical surface, whereas BC-b slightly exceeds this conservative hoop stress limit. A further analysis and optimisation of these lattices would therefore be very fruitful.

In conclusion, the results described above clearly show that the Bucked Coils lattice reduces the RF breakdown issue while performing equally good, or even better than FSIIA in transmission and cooling dynamics. Moreover, the coils of the Bucked Coils lattice experience similar or lower hoop stress than that of FSIIA, and most of them are within the 200 MPa limit. Hence, the Bucked Coils lattice is considered to be a realistic lattice. Due to these positive results, the Bucked Coils is now the main alternative lattice to be used as the cooling lattice of the Neutrino Factory. However, it should be noted that although this lattice reduces significantly the magnetic field in the RF cavities, there is still no experimental evidence demonstrating that this reduction is sufficient for high gradient operation. It is hoped that such evidence can be delivered in the near future. Nevertheless, the Bucked Coils approach is a significant progress towards resolving the problem of the RF breakdown and is believed that in combination with other methods, like cavity surface preparation, can lead to the ultimate solution.

A lepton collider would enable the understanding of the mechanism responsible for the electroweak symmetry breaking and mass generation, while facilitating the search for supersymmetric particles, and signs of extra space-time dimensions. The sufficient energy and luminosity for this physics could be achieved with a Muon Collider, where a six-dimensional cooling is essential.

Aiming to simplify the cell geometry and the installation of the RF cavities, a *novel* six-dimensional cooling lattice was proposed and designed, applicable for use at a Neutrino Factory and a Muon Collider. The "Snake" lattice created dispersion with the use of dipoles rather than tilted solenoids, and a correlation between energy-loss and position was introducing with the use of wedge absorbers. The closed orbit was found for different momenta, which allowed to deduce the orientation of the wedge absorbers. It was found that the phasing of the RF cavities should be adjusted carefully in order for the longitudinal cooling to be achieved. Such an adjustment was difficult to be found in the G4MICE software when using the standard technique, applied in the previous 4D cooling studies. After a detailed investigation, the energy and time difference between a particle and the reference one showed an inward spiralling, clearly demonstrating that the Snake lattice achieves longitudinal cooling.

Another geometry called "Snake-PMMP" was also discussed that presented a dispersion maxima significantly larger than the Snake lattice without increasing the magnetic field. Alternatively, Snake-PMMP could generate a sufficiently large dispersion using smaller dipole field components.

It is strongly believed that both Snake and Snake-PMMP should be further explored as their results look promising. It is concluded that the work on 6D cooling lattices for the Neutrino Factory could allow a solution upgradable to a Muon Collider and studies on such solutions should continue.

Bibliography

[1] A. Bandyopadhyay et al. Physics at a future Neutrino Factory and superbeam facility. *Rept.Prog.Phys.*, 72:106201, 2009.

[2] D. Griffiths. *Introduction to Elementary Particles.* WILEY-VCH, 2 edition, 2008.

[3] S. M. Bilenky. Neutrino masses and oscillations. *arXiv:1105.2306v2 [hep-ph]*, 2011.

[4] F. Perrin. *Comptes Rendus*, 197:1625, 1933.

[5] G.C. Hanna and B. Pontecorvo. *Phys. Rev. 75, 983*, 1949.

[6] J. Angus S. C. Curran and A. L. Cockcroft. *Phil. Mag. 40, 53*, 1949.

[7] T.D. Lee and C.N. Yang. Possible Interference Phenomena between Parity Doublets. *Phys.Rev.*, 104:822–827, 1956.

[8] C.S. Wu, E. Ambler, R.W. Hayward, D.D. Hoppes, and R.P. Hudson. Experimental test of parity conservation in beta decay. *Phys.Rev.*, 105:1413–1414, 1957.

[9] L.D. Landau. *Nucl.Phys. 3, 127*, 1957.

[10] T.D. Lee and C.N.Yang. *Phys. Rev. 105, 1671*, 1957.

[11] A. Salam. *Nuovo Cimento 5, 299*, 1957.

[12] R.G. Arns. Detecting the neutrino. *Phys.Perspect.*, 3:314–334, 2004.

[13] F. Reines and C. L. Cowan. Detection of the free neutrino. *Phys. Rev.*, 92:830–831, 1953.

[14] F. Reines and C. Cowan. The Reines-Cowan experiments: Detecting the Poltergeist. *Los Alamos Sci.*, 25:4–27, 1997. http://library.lanl.gov/cgi-bin/getfile?00326606.pdf.

[15] C.L. Cowan, F. Reines, F.B. Harrison, H.W. Kruse, and A.D. McGuire. Detection of the free neutrino: A Confirmation. *Science*, 124:103–104, 1956.

[16] Frederick Reines and Clyde L. Cowan. The neutrino. *Nature*, 178:446–449, 1956.

[17] B. Pontecorvo. Inverse beta processes and nonconservation of lepton charge. *Sov. Phys. JETP*, 7:172–173, 1958. [Zh.Eksp.Teor.Fiz.34:247,1957].

[18] B. Pontecorvo. Mesonium and antimesonium. *Sov. Phys. JETP*, 6:429, 1957.

[19] Ziro Maki, Masami Nakagawa, and Shoichi Sakata. Remarks on the unified model of elementary particles. *Prog. Theor. Phys.*, 28:870–880, 1962.

[20] Y. Fukuda et al. Evidence for oscillation of atmospheric neutrinos. *Phys. Rev. Lett.*, 81:1562–1567, 1998.

[21] Q. R. Ahmad et al. Measurement of the charged current interactions produced by B-8 solar neutrinos at the Sudbury Neutrino Observatory. *Phys. Rev. Lett.*, 87:071301, 2001.

[22] T. Araki et al. Measurement of neutrino oscillation with KamLAND: Evidence of spectral distortion. *Phys. Rev. Lett.*, 94:081801, 2005.

[23] K. Zuber. *Neutrino Physics, Second Edition.* Series in High Energy Physics, Cosmology and Gravitation. Taylor and Francis, 2009.

[24] Alexandre B. Sousa. Long-baseline neutrino oscillation experiments. *Proceedings of the XXX. Physics in Collision, arXiv:1102.1125v2*, March 2011.

[25] B. Kayser. Neutrino mass, mixing and flavor change. *arXiv:hep-ph/0211134v1*, March 2008.

[26] Boris Kayser. Neutrino physics. *eConf*, C040802:L004, 2004. arxiv:hep-ph/0506165.

[27] F.P. An et al. Observation of electron-antineutrino disappearance at Daya Bay. 2012. 5 figures.

[28] K. Abe et al. Indication of Electron Neutrino Appearance from an Accelerator-produced Off-axis Muon Neutrino Beam. *Phys.Rev.Lett.*, 107:041801, 2011.

[29] P. Adamson et al. Improved search for muon-neutrino to electron-neutrino oscillations in MINOS. *Phys.Rev.Lett.*, 107:181802, 2011.

[30] Neutrino mixing oscillation parameters, http://pdg.lbl.gov/2011/tables/rpp2011-sum-leptons.pdf.

[31] L. Wolfenstein. Neutrino oscillations in matter. *Phys. Rev. D*, 17:2369–2374, May 1978.

[32] Hisakazu Minakata and Hiroshi Nunokawa. CP violation versus matter effect in long baseline neutrino oscillation experiments. *Phys.Rev.*, D57:4403–4417, 1998.

[33] M.H. Ahn et al. Measurement of Neutrino Oscillation by the K2K Experiment. *Phys.Rev.*, D74:072003, 2006.

[34] P. Adamson et al. Measurement of Neutrino Oscillations with the MINOS Detectors in the NuMI Beam. *Phys.Rev.Lett.*, 101:131802, 2008.

[35] M. Guler et al. OPERA: An appearance experiment to search for $\nu_\mu \to \nu_\tau$ oscillations in the CNGS beam. Experimental proposal. 2000.

[36] Y. Itow et al. The JHF-Kamioka neutrino project. pages 239–248, 2001. arXiv:hep-ex/0106019v1.

[37] D. S. Ayres et al. NOvA proposal to build a 30-kiloton off-axis detector to study neutrino oscillations in the Fermilab NuMI beamline. 2004.

[38] T. Akiri et al. The 2010 Interim Report of the Long-Baseline Neutrino Experiment Collaboration Physics Working Groups. 2011. Corresponding author R.J.Wilson (Bob.Wilson@colostate.edu)/ 113 pages, 90 figures.

[39] J. E. Campagne, M. Maltoni, M. Mezzetto, and T. Schwetz. Physics potential of the CERN-MEMPHYS neutrino oscillation project. *JHEP*, 04:003, 2007. http://www.iop.org/EJ/abstract/1126-6708/2007/04/003.

[40] S. Choubey et al. International Design Study for the Neutrino Factory, Interim Design Report. *arXiv:1112.2853 [hep-ex]*, 2011. IDS-NF Collaboration.

[41] Stefan Antusch, Jochen P. Baumann, and Enrique Fernandez-Martinez. Non-Standard Neutrino Interactions with Matter from Physics Beyond the Standard Model. *Nucl.Phys.*, B810:369–388, 2009.

[42] Yuval Grossman. Nonstandard neutrino interactions and neutrino oscillation experiments. *Phys.Lett.*, B359:141–147, 1995.

[43] IDS-NF webpage. *https://www.ids-nf.org/wiki/FrontPage*.

[44] Steve Geer, Olga Mena, and Silvia Pascoli. A Low energy neutrino factory for large θ_{13}. *Phys.Rev.*, D75:093001, 2007.

[45] M. Aiba R. Garoby, E. Benedetto and M. Meddahi. Linac-based proton driver for a neutrino factory. *CERN-NUFACT-NOTE-157*, Dec 2009.

[46] K.T. McDonald, H.G. Kirk, H. Park, T. Tsang, I. Efthymiopoulos, et al. The MERIT High-Power Target Experiment at the CERN PS. *Conf.Proc.*, C100523:3527–3529, 2010. IPAC-2010-WEPE078.

[47] G Prior, SS Gilardoni, HG Kirk, N Souchlas, and X Ding. Update on comparison of the particle production using mars simulation code. oai:cds.cern.ch:1382080. Technical Report CERN-ATS-2011-164, CERN, Geneva, Sep 2011.

[48] John J. Back. EUROnu/IDS-NF: Target. *International Design Study for the Neutrino Factory*, 2011.

[49] Peter Loveridge Tristan Davenne, Otto Caretta. A static packed bed target. http://alturl.com/fydrf.

[50] Harold Kirk. Target System Update. *IDS-NF Plenary, Arlington, VA*, 2011.

[51] Carl H. Albright et al. The neutrino factory and beta beam experiments and development. 2004. aka Feasibility Study II-a.

[52] D. Neuffer, M. Martini, G. Prior, C. Rogers, and C. Yoshikawa. Muon capture in the front end of the IDS neutrino factory. *Conf.Proc.*, C100523:WEPE068, 2010.

[53] A. Alekou. MICE Status. *Conf.Proc.*, C100523:3443–3445, 2010. IPAC-2010-3443-3445, IPAC-2010-WEPE042.

[54] R. Barlow, J.S. Berg, C. Beard, N. Bliss, J. Clarke, et al. EMMA: The world's first non-scaling FFAG. *Nucl.Instrum.Meth.*, A624:1–19, 2010.

[55] Thomas Edgecock, Carl Beard, James Clarke, Stephen Griffiths, Clive Hill, et al. The EMMA Non-scaling FFAG. *Conf.Proc.*, C100523:THPEC090, 2010.

[56] S. Machida et. al. Acceleration in the linear non-scaling fixed-field alternating-gradient accelerator EMMA. *Nature Physics*, (8 243-247), Jan 2012. doi: 10.1038/nphys2179.

[57] Hisakazu Minakata and Shoichi Uchinami. Parameter Degeneracy in Neutrino Oscillation – Solution Network and Structural Overview –. *JHEP*, 1004:111, 2010.

[58] J. Burguet-Castell, M. B. Gavela, J. J. Gomez-Cadenas, P. Hernandez, and O. Mena. On the measurement of leptonic cp violation. *Nuclear Physics*, B608:301–318, 2001.

[59] M.J. Syphers D.A. Edwards. *An Introduction to the Physics of High Energy Accelerators.* New York; Chichester: Wiley, 1993.

[60] S. Y. Lee. *Accelerator Physics.* World Scientific, 2, illustrated edition, 2004.

[61] 2003 Contemporary Physics Education Project (CPEP) Nuclear Science-A Guide to the Nuclear Science Wall Chart. Chapter 11, accelerators. http://www.lbl.gov/abc/wallchart/teachersguide/pdf/Chap11.pdf.

[62] Frank Gerigk. Cavity types. *arXiv:1111.4897v1 [physics.acc-ph]*, 2011.

[63] T.P. Wangler. *RF linear accelerators.* WILEY-VCH, 2 edition, 2008.

[64] H. Wiedemann. *Particle accelerator physics I : basic principles and linear beam dynamics.* Berlin; London: Springer, 2, revised edition, 2003.

[65] E. J. N. Wilson (Edward J. N.). *An introduction to particle accelerators.* Oxford : Oxford University Press, 2001.

[66] Gerald Dugan. Lecture 10: Single particle acceleration, Linear Accelerator Dynamics. *USPAS Accelerator School*, Phys 450B: Introduction to Accelerator Physics, 2002. http://www.lns.cornell.edu/ dugan/USPAS/.

[67] R. Wideroe. *Arch. fur Electrotechnik.* Number 21, 387. 1928.

[68] E. T. S. Walton. *Proc. Cambridge Phil. Soc.* Number 25, 569. 1929.

[69] M. Steenbeck. *U.S. Patent.* Number 2, 103, 303. 1935.

[70] D. W. Kerst and R. Serber. Electronic orbits in the induction accelerator. *Phys. Rev.*, 60:53–58, Jul 1941.

[71] J Rossbach and P Schm§ser. Basic course on accelerator optics. (DESY-M-93-02):72 p, Feb 1993.

[72] M.G. Minty and F. Zimmermann. *Measurement and control of charged particle beams*. Particle acceleration and detection. Springer, 2003.

[73] H. Wiedemann. *Particle accelerator physics II: nonlinear and higher-order beam dynamics*. Berlin; London: Springer, 1995.

[74] Gerald Dugan. Lecture 5: Periodic systems, Twiss parameters and stability, Hill's equation and its solution, Courant-Snyder invariant and emittance. *USPAS Accelerator School*, Phys 450B: Introduction to Accelerator Physics, 2002. http://www.lns.cornell.edu/ dugan/USPAS/.

[75] G. Penn and J. S. Wurtele. Beam envelope equations for cooling of muons in solenoid fields. *Phys. Rev. Lett.*, 85:764–767, Jul 2000.

[76] D. Neuffer. Introduction to muon cooling. *Nucl.Instrum.Meth.*, A532:26–31, 2004.

[77] Particle Data Group. Passage of particles through matter. *http://pdg.lbl.gov/2006/reviews/passagerpp.pdf.*

[78] G. Gregoire, G. Ryckewaert, L. Chevalier, J.M. Rey, M.G. Catanesi, et al. Proposal to the Rutherford Appleton Laboratory: an international muon ionization cooling experiment (MICE). 2003.

[79] ISIS website. How isis works. http://www.isis.stfc.ac.uk/about-isis/how-isis-works6313.html.

[80] M. Ellis, P.R. Hobson, P. Kyberd, J.J. Nebrensky, A. Bross, et al. The Design, construction and performance of the MICE scintillating fibre trackers. *Nucl.Instrum.Meth.*, A659:136–153, 2011.

[81] 2010. From Dr. Adam Dobbs, Private Communication.

[82] U. Bravar, M. Bogomilov, Y. Karadzhov, D. Kolev, I. Russinov, et al. MICE: the Muon Ionization Cooling Experiment. Step I: First Measurement of Emittance with Particle Physics Detectors. 2011.

[83] Alain Blondel ed. Mice status report. *MICE-NOTE-GEN 334.*, 2011.

[84] Muon Collider Advanced Accelerator R&D Proposal. 2012.

[85] R&D proposal for the National Muon Accelerator Program. *Revision 6d, FERMILAB-TM-2459-APC*, 2010.

[86] Arash Zarrebini. Vacuum rf r&d in uk. *U.K. Cavity Development Consortium, MuCool RF Workshop*, Jul 2009.

[87] Robert B. Palmer, Richard C. Fernow, Juan C. Gallardo, Diktys Stratakis, and Derun Li. RF Breakdown with and without External Magnetic Fields. *arXiv:0809.1633v1 [physics.acc-ph]*, 2008.

[88] R. H. Fowler and L. W. Nordheim. Electron emission in intense electric fields. *Proc R. Soc. London, Ser. A*, vol. 119(781):173, 1928.

[89] J. Norem, V. Wu, A. Moretti, M. Popovic, Z. Qian, et al. Dark current, breakdown, and magnetic field effects in a multicell, 805 MHz cavity. *Phys.Rev.ST Accel.Beams*, 6:072001, 2003. Publishers note in Phys.Rev.ST Accel.Beams 6:089901,2003 concerning the correction of an incorrect submission date.

[90] Juan C. Gallardo and Michael S. Zisman. Thoughts on Incorporating HPRF in a Linear Cooling Channel. *AIP Conf.Proc.*, 1222:308–312, 2010. 5 pages, 8 figures, submitted to Proceedings of NUFACT09.

[91] A.V. Tollestrup. Beam-Cavity Interaction for High Pressure Hydrogen Gas Filled Cavities. 2007. NFMCC-DOC-514.

[92] A.V. Tollestrup. HPRF with Beam: Beam Interaction with gas filled RF Cavities. 2008. Low Emittance Muon Collider Workshop, April 2008.

[93] C.T. Rogers. Design for a Muon Front End with Magnetically Shielded RF Cavities. *AIP Conf.Proc.*, 1222:298–302, 2010.

[94] A. Alekou, D. Neuffer, M. Martini, G. Prior, C. Rogers, et al. Alternative Muon Front-end for the International Design Study (IDS). *Conf.Proc.*, C100523:3455–3457, 2010. IPAC-2010-WEPE050.

[95] A. Alekou, J. Pasternak, and C. Rogers. Muon Cooling Performance in Various Neutrino Factory Cooling Cell Configurations using G4MICE. *Conf.Proc.*, C100523:3458–3460, 2010. IPAC-2010-WEPE051.

[96] Milorad Popovic. The muon test area at Fermilab. 2004. EPAC-2004-MOPLT118, http://accelconf.web.cern.ch/accelconf/e04/PAPERS/MOPLT118.PDF.

[97] K. Yonehara. Proposal for high pressure RF cavity test in the MTA. 2010. FERMILAB-TM-2474-APC.

[98] C.T. Rogers and Rikard Sandstrom. Simulation of MICE using G4MICE. *Conf.Proc.*, C060626:2400–2402, 2006.

[99] R. C. Fernow. Bucked cooling channels for the neutrino factory, 2008. BNL, IDS meeting, FNAL, https://pubweb.bnl.gov/ fernow/meetings/ids08/bucked.ppt.

[100] MATLAB. *Version 7.14.0.739 (R2012a).* The MathWorks Inc., Natick, Massachusetts, 2012.

[101] 2011. From Dr. Chris Rogers, Private Communication.

[102] F. Herlach and N. Miura. *High magnetic fields: science and technology.* Number v. 3 in High Magnetic Fields. World Scientific, 2003.

[103] E Todesco and P Ferracin. Limits to high field magnets for particle accelerators. oai:cds.cern.ch:1425903. Technical Report CERN-ATS-2012-052, CERN, Geneva, Feb 2012.

[104] C.P. Poole. *Superconductivity.* Academic Press, 2007. http://books.google.co.uk/books?id=HWnDpQPpM3kC.

[105] L Bottura. A practical fit for the critical surface of nbti. oai:cds.cern.ch:411159. *IEEE Trans. Appl. Supercond.*, 10(LHC-Project-Report-358):1054–7. 5 p, Dec 1999.

[106] M.S. Lubell. Empirical scaling formulas for critical current and critical field for commercial nbti. Technical Report CONF-821108-35, Jan 2001.

[107] Ezio Todesco and L Rossi. Electromagnetic design of superconducting dipoles based on sector coils. oai:cds.cern.ch:1076301. *Phys. Rev. Spec. Top. Accel. Beams*, 10(CERN-AT-2007-032):112401. 12 p, Dec 2007.

[108] Daniel M. Kaplan. From Neutrino Factory to Muon Collider. *AIP Conf. Proc.*, 1382:64–68, 2011.

[109] R. B. Palmer et al. Ionization cooling ring for muons. *Phys. Rev. ST Accel. Beams*, 8:061003, 2005.

[110] Autin, B., (ed.) and Carli, C. and D'Amico, T. and Grobner, O. and Martini, M. et al. Beam Optics: A program for analytical beam optics. 1998. CERN-YELLOW-98-06.

[111] From Dr. Jaroslaw Pasternak, Private Communication.

Appendix A

Appendix

A.1. Emittance Exchange

The cooling rate sum of x, y, and z, stays constant, and can be represented as a sum of the cooling partition numbers. A partition number is defined as the ratio of the cooling rate to the fractional momentum loss rate. For x and y, the partition numbers g_x and g_y are [76]:

$$g_x = g_y = \frac{\frac{d\epsilon_x/ds}{\epsilon_x}}{\frac{dp/ds}{p}} = 1, \tag{A.1.1}$$

whereas the partition number for longitudinal cooling is a function of muon energy, and is given by:

$$g_L = \frac{\frac{d\epsilon_L/ds}{\epsilon_L}}{\frac{dp/ds}{p}} = \frac{\frac{\partial(dE/ds)}{\partial E}}{\frac{dp/ds}{p}} = \frac{\frac{\partial(dp/dt)}{\partial p}}{\frac{(dp/dt)}{p}}. \tag{A.1.2}$$

Therefore, the longitudinal cooling can be written as:

$$\frac{d\sigma_E^2}{ds} = -2\frac{g_L\frac{dE}{ds}}{\beta^2 E}\sigma_E^2 + 4\pi(r_e m_e c^2)^2 n_e \gamma^2\left(1 - \frac{\beta^2}{2}\right), \tag{A.1.3}$$

which can be transformed into a longitudinal emittance cooling equation:

$$\frac{d\epsilon_L}{ds} = -\frac{g_L}{\beta^2 E}\frac{dE}{ds}\epsilon_L + \frac{\beta_\phi}{2}\frac{d\langle\Delta E_{rms}^2\rangle}{ds}, \tag{A.1.4}$$

where β_ϕ is a focusing function, given by:

$$\beta_\phi^2 = \frac{\langle\phi^2\rangle}{\langle\Delta E^2\rangle} = \frac{1}{\beta^3\gamma e V' \sin\phi_s}\frac{2\pi}{\lambda_0}\frac{\alpha_c}{mc^2}, \tag{A.1.5}$$

and V and α_c are the RF voltage and the momentum compaction factor respectively.

When wedge absorbers are used in order for the longitudinal cooling to be enhanced, g_x will become

$$g_x = 1 - \frac{\eta\rho'}{\rho_0}, \tag{A.1.6}$$

whereas g_L will increase by $\eta\rho'/\rho_0$, keeping the sum of the partition numbers, $\Sigma_g = (g_x + g_y + g_L)$ constant.

A.2. Equation of Motion in Solenoid

In [73] it is analytically described how a particle at the location σ that is under the influence of the Lorentz force in of a $(x,\ y,\ s)$-coordinate system[1], follows a path described by the vector $\mathbf{S}$. While in static magnetic fields the value of the particles momentum is unchanged, the momentum vector changes in time due to the change in the momentum direction. Therefore $\mathbf{p} = pd\mathbf{S}/d\sigma$, where p is the value of the particle's momentum, and $\mathrm{d}\mathbf{S}/d\sigma$ is the unit vector along the particle trajectory. Using $\frac{d\mathbf{p}}{d\tau} = \frac{d\mathbf{p}}{d\sigma}\beta c$, where $\tau = \frac{\sigma}{\beta c}$ and $\mathbf{v}_\sigma = \frac{d\mathbf{S}}{d\tau} = \frac{d\mathbf{S}}{d\sigma}\beta c$, the differential equation that describes the particle trajectory under the influence of a Lorentz force, $\mathbf{F}_L$, is described. This force is equal to $\mathbf{F}_L = \frac{d\mathbf{p}}{d\tau} = \frac{[c]e}{c}[\mathbf{v}_\sigma \times \mathbf{B}]$, and the differential equation is[2]:

$$\frac{d^2\mathbf{S}}{d\sigma^2} = \frac{[c]e}{cp}\left[\frac{d\mathbf{S}}{d\sigma} \times \mathbf{B}\right]. \tag{A.2.1}$$

Since $\frac{d\mathbf{S}}{d\sigma} = \frac{\mathbf{S}'}{\sigma}$ then $\frac{d^2\mathbf{S}}{d\sigma^2} = \frac{1}{\sigma'}\frac{d}{ds}\frac{\mathbf{S}'}{\sigma'}$, the general equation of motion then becomes:

$$\frac{d^2\mathbf{S}}{d\sigma^2} - \frac{1}{2\sigma'^2}\frac{d\mathbf{S}}{ds}\frac{d\sigma^{2\prime}}{ds} = \frac{[c]e}{cp}\sigma'\left[\frac{d\mathbf{S}}{ds} \times \mathbf{B}\right]. \tag{A.2.2}$$

From [73] it is also shown that this general equation of motion for a charged

---

[1] s, sometimes denoted as z, describes the direction along the beam-axis.

[2] Depending on what unit system is being used, c can be omitted, in which case it is written as $[c]$.

particle in a magnetic field **B** becomes:

$$\begin{aligned}
&\mathbf{x}_o(x'' + k_x + k_x^2 x + k_x k_y y - \tfrac{x'}{2\sigma^{2\prime}}\tfrac{d\sigma^{2\prime}}{ds}) \\
&+\mathbf{y}_o(y'' + k_y + k_y^2 y + k_x k_y x - \tfrac{y'}{2\sigma^{2\prime}}\tfrac{d\sigma^{2\prime}}{ds}) \\
&-\mathbf{s}_o(2k_x x' + 2k_y y' + k_{x'} x + k_y' y + \tfrac{1+k_x x+k_y y}{\sigma^{2\prime}}\tfrac{d\sigma^{2\prime}}{ds}) \\
&= \tfrac{[c]e}{cp}\sigma' \left[\tfrac{d\mathbf{S}}{ds} \times \mathbf{B}\right].
\end{aligned} \tag{A.2.3}$$

This is a general equation of motion for charged particles in a magnetic field **B**, where no approximations have been applied. The individual components can be separated for practicality and the differential equations of transverse motion become:

$$\begin{aligned}
&x'' - k_x(1 + k_x x + k_y y) - \frac{1}{2}\frac{x'}{\sigma'^2}\frac{d\sigma'^2}{ds} = \\
&\frac{[c]e}{cp}\sigma'[y' B_s - (1 + k_x x + k_y y)B_y]
\end{aligned} \tag{A.2.4}$$

$$\begin{aligned}
&y'' - k_y(1 + k_x x + k_y y) - \frac{1}{2}\frac{y'}{\sigma'^2}\frac{d\sigma'^2}{ds} = \\
&\frac{[c]e}{cp}\sigma'[(1 + k_x x + k_y y)B_x - x' B_s].
\end{aligned} \tag{A.2.5}$$

Within a hard edge approximation, where the magnetic field depends on s in a way that the fields are zero in magnet free sections and a constant value is assumed within the magnets[3], the field is described by:

$$k_y = \frac{[c]e}{cp}B_x = \frac{[c]e}{cp}(B_{x_o} + gy + sxy - \underline{g}x - \frac{1}{2}\underline{s}(x^2 - y^2) + \mathcal{O}(3)) \tag{A.2.6}$$

$$k_x = -\frac{[c]e}{cp}B_y = -\frac{[c]e}{cp}(B_{y_o} + gx + \frac{1}{2}s(x^2 - y^2) + \underline{g}y + \underline{s}xy + \mathcal{O}(3)), \tag{A.2.7}$$

where p is the momentum of the reference particle, g and s are the quadrupole and sextuple coefficients, and $\underline{g}, \underline{s}$ are the skew[4] coefficients.

Rotated quadrupoles (skew quadrupoles) and solenoid magnets are the most generally used magnets that introduce coupling in beam transport systems. When restricting the beam dynamics to rotated quadrupole and solenoid fields, and neglecting the transverse beam deflection, then the resulting linear cou-

---

[3] This assumption results in a step function distribution of the magnetic fields.

[4] The coils are rotated with respect to the closed orbit.

pling gives the following equations of motion[5]:

$$\begin{aligned} x'' + kx &= -\underline{k}y + Sy' + \frac{1}{2}S'y, \\ y'' - ky &= -\underline{k}x - Sx' - \frac{1}{2}S'x, \end{aligned} \tag{A.2.8}$$

where S is the solenoidal field: $S(s) = \frac{e}{cp}B_s(s)$. When considering only the solenoidal fields $\mathbf{B} = (-\frac{1}{2}B_s'x, -\frac{1}{2}B_s'y, B_s)$, these equations can be simplified to:

$$\begin{aligned} x'' - S(s)y' - \frac{1}{2}S'(s)y &= 0, \\ y'' + S(s)x' - \frac{1}{2}S'(s)x &= 0. \end{aligned} \tag{A.2.9}$$

A.3. Hill's Equation in 2D

In [64] it is described that the solutions of Hill's equation and their properties have been formulated by Floquet's theorem:

- Two independent solutions exist of the form:

  $$u_1(s) = w(s) \cdot e^{i\mu s/L}, u_2(s) = w^*(s) \cdot e^{-i\mu s/L}, \tag{A.3.1}$$

  where $w^*(s)$ is the complex conjugate solution to $w(s)$. It can be assumed $w^*(s) = w(s)$ as for all beam dynamics practical cases there are only real solutions.

- $w(s)$ is unique and periodic with period L:

  $$w(s + L) = w(s). \tag{A.3.2}$$

- μ is a characteristic coefficient defined by:

  $$\cos \mu = \frac{1}{2}Tr[\mathbf{M}(s + L)]. \tag{A.3.3}$$

- The trace and transformation of matrix $\mathbf{M}$ is independent of s: $Tr[\mathbf{M}(s+$

---

[5] As before, the underlying terms represent the magnet strengths of rotated multipole magnets.

$L)] \neq f(s)$.

- The determinant of the transfer matrix **M** is: det**M**=1.
- The solutions remain finite for $\frac{1}{2}Tr[\mathbf{M}(s+L)] < 1$.

The transformation of a trajectory u through one lattice period of length L must be equivalent to the multiplication by the transfer matrix **M**:

$$\mathbf{M} = \begin{bmatrix} \cos\phi + \alpha \cdot \sin'\phi & \beta \cdot \sin\phi \\ -\gamma \cdot \sin\phi & \cos\phi - \alpha \cdot \sin\phi \end{bmatrix}. \tag{A.3.4}$$

So:

$$u(s+L) = \cos(\cos\psi + \alpha \cdot \sin\psi) \cdot u(s) + \beta \cdot \sin\psi \cdot u'(s), \tag{A.3.5}$$

where u can be any of the solutions of (A.3.1), and ψ is the betatron phase advance for L. In addition, from equations A.3.1 and A.3.2:

$$u(s+L) = u(s) \cdot e^{\pm i\mu} = u(s) \cdot (\cos\mu \pm i \cdot \sin\mu). \tag{A.3.6}$$

When comparing the coefficients of the sine and cosine terms then it can be seen that:

$$\cos\psi = \cos\mu,\ or\ \psi = \mu, \tag{A.3.7}$$

and

$$\alpha \cdot u(s) + \beta \cdot u'(s) = \pm i \cdot u(s). \tag{A.3.8}$$

Equation A.3.8 can be simplified if a logarithmic differentiation is performed:

$$\frac{u''}{u'} - \frac{u'}{u} = -\frac{\beta'}{\beta} - \frac{\alpha'}{\pm i - \alpha}.$$

Moreover, from Hill's equation (3.3.1) and A.3.8 it can be derived:

$$\frac{u''}{u'} - \frac{u'}{u} = \frac{-K\beta}{\pm i - \alpha} - \frac{\pm i - \alpha}{\beta}.$$

By equating the right hand side terms of these two expressions it can be found that

$$(1 - \alpha^2 - K \cdot \beta^2 + \alpha' \cdot \beta - \alpha \cdot \beta') \pm i \cdot (2\alpha + \beta') = 0.$$

All functions in the brackets are real as long as there is stability and therefore both brackets must be equal to zero. This is how:

$$\beta' = -2\alpha, \tag{A.3.9}$$

and

$$\alpha' = K \cdot \beta - \gamma. \tag{A.3.10}$$

By combining eq. A.3.9 and eq. A.3.8 then it can be seen that

$$\frac{u'}{u} = \frac{\pm i - \alpha}{\beta} = \pm\frac{i}{\beta} + \frac{1}{2}\frac{\beta'}{\beta}, \tag{A.3.11}$$

which can be integrated:

$$log\frac{u}{u_o} = \pm\int_o^s \frac{ds}{\beta} + \frac{1}{2} \cdot log\frac{\beta}{\beta_o}, \tag{A.3.12}$$

with $u_o = u(s_o)$ and $\beta_o = \beta(s_o)$ for $s = s_o$. The solution of u is then [64]:

$$u(s) = \alpha\sqrt{\beta(s)}e^{\pm i\psi}, \tag{A.3.13}$$

with $\alpha = u_o/\sqrt{\beta_o}$ and $\psi(s - s_o) = \int_{s_o}^{s} \frac{d\tau}{\beta(\tau)}$.

A.4. Optics and Tracking of BC-a, -b, and -c

The transverse betatron functions, $\beta_\perp$, of BC-a, -b, and -c, presented in chapter 8, are plotted with respect to the beam-axis, z, against the lattices presented in chapter 7 (see fig. A.1). The new lattices, BC-a, -b, and -c, have the largest $\beta_\perp$ values. Therefore these lattices are expected to provide a worse cooling than FSIIA, BC-I, -II, -III, and -IV. However, the new lattices have the smallest variations in $\beta_\perp$ and hence, the muon transmission in these lattices is expected to be significantly better.

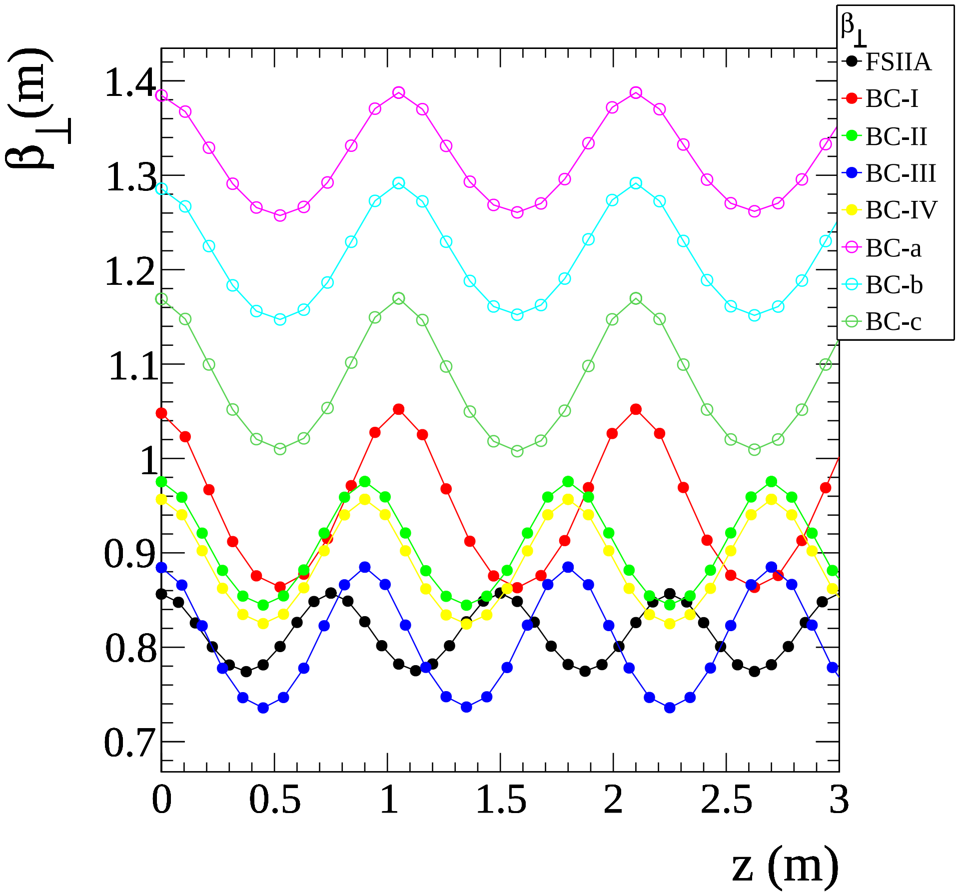

Figure A.1.: Transverse betatron function, $\beta_\perp$, with respect to the beam-axis, z. The new lattices, BC-a (purple), BC-b (cyan) and BC-c (dark green) have the largest values of $\beta_\perp$ ($\beta_{\perp,a} > \beta_{\perp,b} > \beta_{\perp,c}$), which implies a worse cooling effect. On the other hand, these lattices have the smallest $\beta_\perp$ variations and are therefore expected to present a better transmission.

The transverse betatron function $\beta_\perp$ with respect to the momentum, P of the new lattices is shown in fig. A.2. The smaller gradient of BC-c in comparison to BC-a implies a better performance for BC-c.

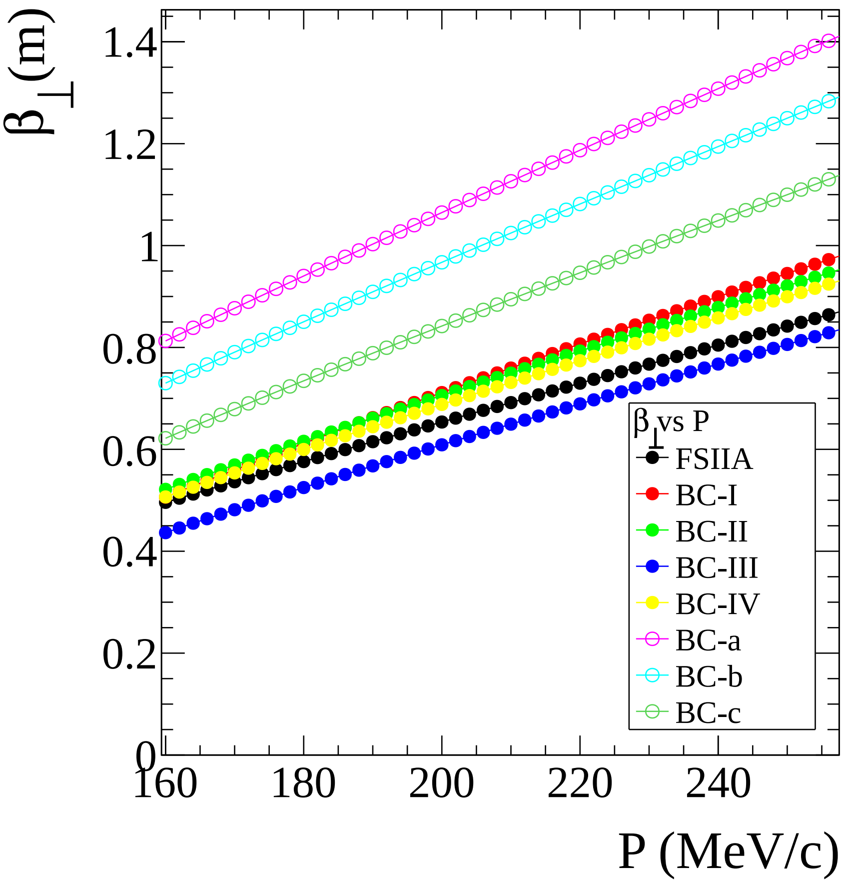

Figure A.2.: Transverse betatron function $\beta_\perp$ with respect to the momentum, P, for the new lattices BC-a (purple), BC-b (cyan) and BC-c (dark green). These lattices have larger gradients in comparison to FSIIA, and BC-I to BC-IV, and therefore a worse performance is expected.

The muon transmission in BC-a, -b, and -c was plotted along the beam-axis (fig. A.3). No cuts were applied for this plot. The new lattices obtain the best transmission over all, closely followed by BC-IV performance.

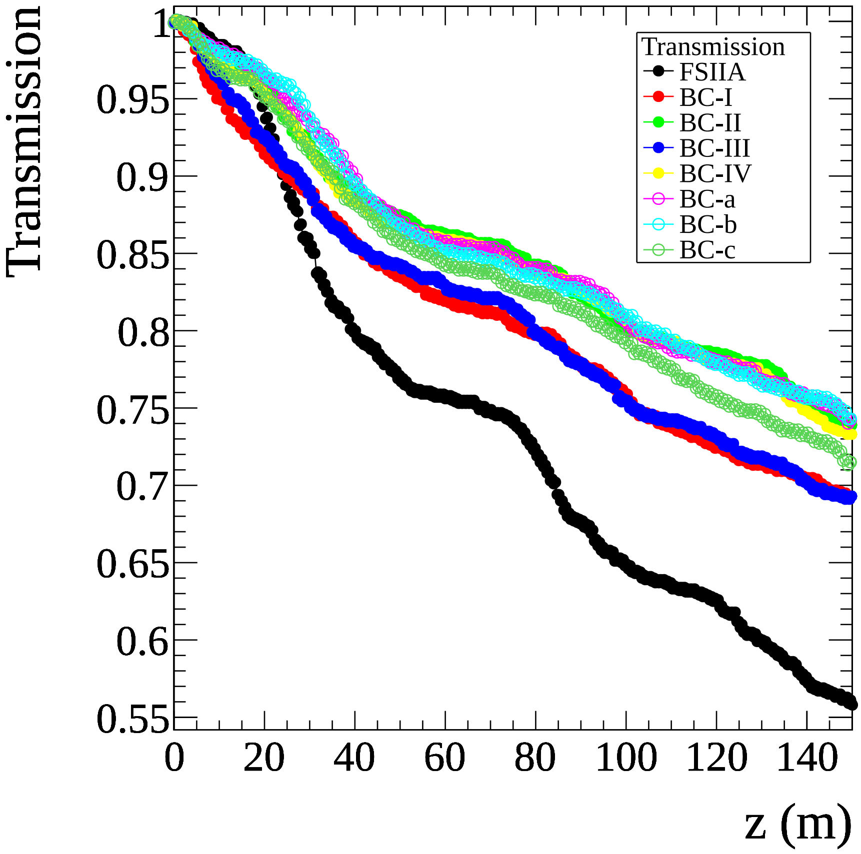

Figure A.3.: Transmission along the beam-axis. The new lattices BC-a, -b, -c have a better transmission than FSIIA and perform similarly to BC-IV.

The transverse emittance, $\epsilon_{\perp}$ along the beam-axis is presented in fig. A.4. Only the particles that managed to reach the end of the lattice were taken into account for this plot. As can be seen, the equilibrium emittance of the new lattices is larger than that of FSIIA, as was expected from fig. A.2. Still, BC-a, -b, and -c are within cooling limits.

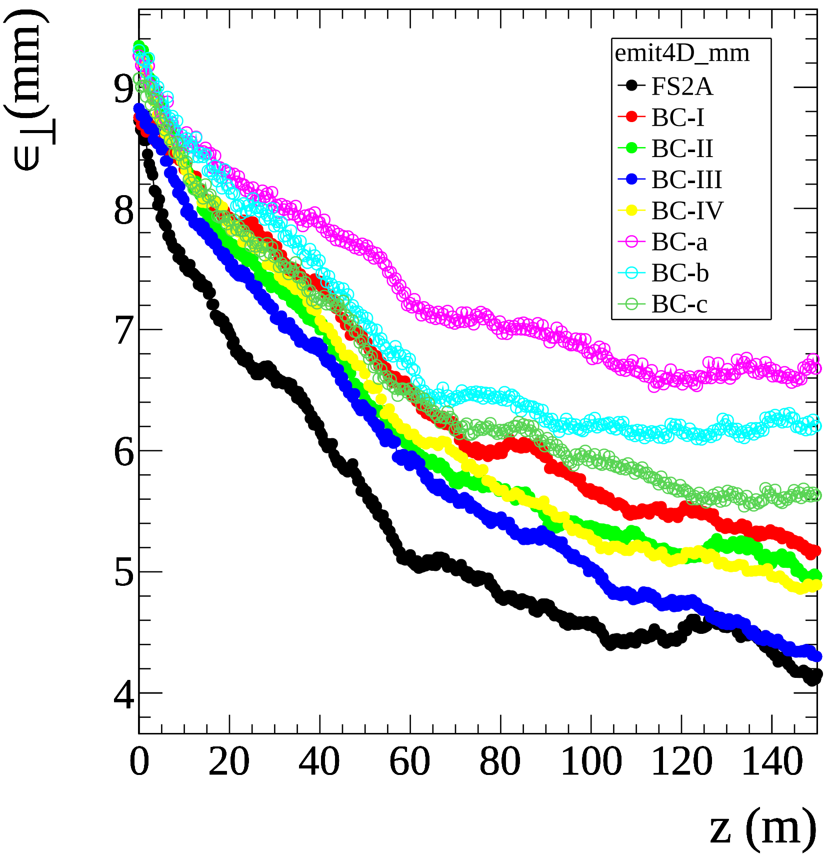

Figure A.4.: Transverse emtitance $\epsilon_\perp$ along the beam-axis, z. The equilibrium emittance of BC-a, -b, and -c is larger than that of FSIIA and BC-I to -IV, as expected from the large $\beta_\perp$ the new lattices have.